Advanced High-Frequency Measurement Techniques for Electrical and Biological Characterization in CMOS

Jun-Chau Chien
Ali Niknejad

Electrical Engineering and Computer Sciences
University of California at Berkeley

Technical Report No. UCB/EECS-2017-9
http://www2.eecs.berkeley.edu/Pubs/TechRpts/2017/EECS-2017-9.html

May 1, 2017

Advanced High-Frequency Measurement Techniques for Electrical and Biological Characterization in CMOS

by

Jun-Chau Chien

A dissertation submitted in partial satisfaction of the

requirements for the degree of

Doctor of Philosophy

in

Engineering – Electrical Engineering and Computer Sciences

in the

Graduate Division

of the

University of California, Berkeley

Committee in charge:

Professor Ali M. Niknejad, Chair
Professor Jan M. Rabaey
Professor Liwei Lin

Spring 2015

Advanced High-Frequency Measurement Techniques for Electrical and Biological Characterization in CMOS

Abstract

Advanced High-Frequency Measurement Techniques for Electrical and Biological Characterization in CMOS

by

Jun-Chau Chien

Doctor of Philosophy in Electrical Engineering and Computer Science

University of California, Berkeley

Professor Ali M. Niknejad, Chair

Precision measurements play crucial roles in science, biology, and engineering. In particular, current trends in high-frequency circuit and system designs put extraordinary demands on accurate device characterization and modeling. On the other hand, the need for better point-of-care requires substantial innovation in developing miniaturized sensors and medical devices that ease the biological analysis without sacrificing the accuracy. This research presents two advanced measurement techniques for electrical and biological characterization applications.

In the first part, a novel single-element on-wafer VNA calibration algorithm is presented dedicated for device characterization at mm-Waves. Conventional calibration approaches such as thru-reflect-line (TRL) require at least three precisely-machined and well-characterized standards. The necessity of probe re-positioning leads to significant measurement errors due to mechanical uncertainty as the measurement frequency approaches sub-THz. By exploiting on-chip impedance modulation, such an electronic calibration (E-Cal) algorithm can work with single element without any prior knowledge of the impedance behavior. This CMOS-based approach opens a new direction in the field of VNA calibration.

In the second part, the implementation of a dielectric spectroscopy biosensor aiming for single-cell analysis is presented. Most present day clinical flow cytometers use fluorescence-activated cell sorting (FACS), which requires bulky optical detection system as well as complex sample-labeling process, limiting the assay time and the wide-spread adoption in the point-of-care (POC) setting. To address these issues, this research presents the design and the implementation of a sensor-on-CMOS spectrometer that measures the microwave signature of single cell as a potentially label-free analytic tool. The sensor covers four frequency bands across 6.5 – 30 GHz, offering sub-aF noise sensitivity at 100-kHz bandwidth. Such performance is enabled with injection-locked oscillator sensors in interferometry architecture. With microfluidic integration, experiments on flow cytometry and molecular sensing are demonstrated.

To my parents and Yu-Ling

TABLE OF CONTENTS

Acknowledgements

I would like to express my sincere gratitude to my advisor Professor Ali M. Niknejad. Your advices have guided me in different aspects throughout various research projects. I would also like to thank you for giving me the freedom in exploring different research fields beyond the integrated circuits, which greatly expands the scope of the research. In addition, I am very grateful to have the opportunity serving as the GSI in your class. It’s an invaluable experience to learn the teaching philosophy and work side-by-side with the best circuit experts in the world. You have become my role model: I have learned a lot in managing a research team and striking for balance between working and family. Thank you, Ali!

I would also like to acknowledge Professor Jan M. Rabaey, Professor Ahmad Bahai, and Professor Liwei Lin for being on my qualification committee, providing various insights and visionary thoughts in this research project. I would like to acknowledge Professor Elad Alon, Professor Amin Arbabian from Stanford University, Professor Mekhail Anwar from UCSF, Professor Luke P. Lee, Professor Michel Maharbiz, and Professor Amy Herr for your feedbacks in various design reviews and discussions. You have inspired me greatly throughout my biosensor research.

I would like to especially thank to Ken Chang, Jafar Savoj, and Parag Upadhyaya from Xilinx. The five-month internship is one of my best professional experiences. I especially thank to Ken for your leadership and career advices.

I am fortunate to be in part of Berkeley Wireless Research Center (BWRC) where I can meet so many talented scholars and good friends. In particular, I would like to thank to Stanley Chen, Tsung-Te Liu, Yue Lu, Charles Wu, Steven Callender, Bagher Afshari, Ashkan Borna, Ehsan Adabi, Shinwon Kang, Jungdong Park, Siva Thyagarajan, Wen Li, Yida Duan, Lingkai Kong, Chintan Thakkar, Ping-Chen Huang, and Nai-Chung Kuo.

I would like to thank sincerely to my dear friends, Yang Lin, Wei-Chang Li, Yenhao Chen, Lingqi Wu, Chung-Wei Lin, Ruonan Liu, Yung-Kan Chen, Yao-Ting Mao, Charlie Yeh, Chih-Chung Fu, and friends from Berkeley Association of Taiwanese Students (BATS) Basketball team for making my life at Berkeley very much enjoyable.

I would like to show my deepest gratitude to my parents. Your love, supports, and encouragement are my foundation throughout the years. Finally, I would like to express my deepest gratitude to my fiancée, Yu-Ling. Seven years of long distance relationship (two years of Taipei – Berkeley, five years of Seattle – Berkeley) is not easy. I am so grateful to have your company. We finally made it. Love you, Yu-Ling!

Chapter 1

Introduction

Microwaves are ubiquitous in our daily life. Microwave ovens, cellular phones, airport security scanning machine, and hyperthermia treatments of cancer with microwave ablations are some good examples. With the advance of semiconductor technology, we will soon enter the era of millimeter-waves (mm-Wave), particularly driven by the need for the next generation low-power mobile communications. Though planar CMOS technology has shown its capability for sub-THz circuits and systems [1 – 2], new devices such as FinFETs, nanowire transistors, and new devices with heterogeneous integration of silicon, III-V, and organics compounds are gaining more attention. The latter will enable numerous applications in wearable devices and sensors applications due to its capability for implementation on a flexible substrate [3]. To embrace new technologies at yet higher frequencies for better system performance in various emerging applications, precision measurements are indispensable at both the device and circuit levels.

In the other domain, the characterization and the analysis of biological specimen are the fundamentals for medical diagnosis in point-of-care health monitoring, biological research, and clinical studies. These specimens include tissues, cells, and bio-molecules such as glucose, DNA, and proteins. Study on the constituents of these biological specimens as well as their dynamic responses when subjected to chemical modification is extremely beneficial in the development of disease treatment and pharmaceuticals. Though consumer electronics have become ubiquitous and inexpensive, medical devices, by contrast, are still primarily found only in the hospitals. To make the dream *Physician in everyone's phone* come true, substantial innovation is required to develop new sensors and devices that are fundamentally less invasive and able to operate with batteries for portable applications.

To address the needs for precision measurements in both the electrical and biological characterization applications, two techniques are developed in this research. In the next two sections, we will provide an introduction to each of the problems.

1.1 High-Frequency Measurements for Device Characterization

Device characterization plays a major role in microwave engineering. Many of the circuit performance can be predicted directly based on the measured S-parameters such as amplifier gain [4]. In addition, device modeling with scalability is mandatory to fully exploit the power of mixed-signal circuit designs. Nowadays device modeling is mostly performed at the foundry based on the measurements at limited frequency ranges (< 20 GHz). Extrapolation is consequently mandatory to predict the circuit performance either by simply trusting the results from the post-layout extraction or performing excessive electromagnetics simulations. The importance of precise device characterization cannot be further emphasized.

Calibration and de-embedding are mandatory for accurate S-parameter measurements. The purpose of the calibration and de-embedding is to remove the parasitics effect of the error boxes from the raw measurements. These error boxes can consist of the components within the network analyzer such as the directional couplers as well as those outside the network analyzer including cables, probes, connectors, and probing pads. By shifting the reference planes as close as possible to the devices and circuits ports, actual behaviors can be reliably measured.

Currently, TRL and multiline TRL (mTRL) are recognized as the standard procedure for on-wafer calibration [5 – 6]. These algorithms offer the highest accuracy with minimum requirement on the impedance information of the calibration structures when compared to SLOT (short-load-open-thru) and LRRM (line-reflect-reflect-match) and therefore are the golden standard taken by National Institute of Standard and Technology (NIST). However, TRL requires at least three calibration structures. Thus, the measurements are more susceptible to probing error. Such a problem is more pronounced at mm-Wave and sub-THz frequencies due to the shrinkage of the wavelengths. On the other hand, simplification of error box model can reduce the number of calibration structures at the cost of model accuracy. For instance, open/short and thru-only approaches require the minimum number of structures by modeling the test fixture with lumped equivalent circuit where the distributed effects are ignored [7]. In this work, we exploit a ubiquitous device in CMOS in the application for on-wafer calibration and de-embedding: the MOS transistors. By performing impedance modulation electronically, the process requires only a *single* element while solving for the full two-port S-parameter of the test fixture, maintaining TRL-equivalent accuracy.

1.2 Dielectric Spectroscopy for Cellular and Molecular Sensing

Dielectric spectroscopy measures the response of a biological specimen when exposed to alternating electromagnetic fields over a broad frequency range [8]. By measuring the effective permittivity and the conductivity, the discrimination between cells is achievable based on their size, morphology, and compositions [9]. The instantaneous change of a single cell can also be examined in real-time to infer its physiological state under excitations. Such label-free and non-destructive approaches have drawn great attention due to its simplicity in sample preparation. Nevertheless, most of the work to date lack quantitative analysis and biological explanations for the phenomenon observed. In addition, the scale of the samples is still relatively large, mostly limited by the sensor geometry and performance. Researches have demonstrated the ability to detect the presence of a cell but do not offer adequate sensitivity for discrimination purpose.

Many of the previous research in this field have focused primarily on the sensor design and leave the work of detection to an external broadband network analyzer. The cost and the lack of portability prohibit such technology for point-of-care. Miniaturization using integrated circuits (IC) technology is therefore mandatory. In addition to its size, sensor-on-CMOS can potentially offer higher sensitivity that is not achievable with conventional tools, opening a new door for scientific studies.

This research presents two microwave sensors in CMOS. The first one employs an impedance analyzer architecture using transmission-line sensors, enabling a measurement range of 1 – 50 GHz, the widest to date. Such a sensor performs dielectric sensing within an area of $200 \times 20\ \mu m^2$ using fringing fields. Chemical mixtures and biological medium measurements are demonstrated and measurement technique for drift mitigation is proposed. The second chip presents a novel spectrometer architecture for single-cell analysis in flow cytometry. With the distribution of narrowband oscillator-sensors along a microfluidic channel, both broad frequency coverage and enhanced sensitivity are achieved simultaneously. The sensor performance is furthered improved by injection locking the sensor oscillators which transforms frequency shift, the signal of interest, to a phase quantity that can be measured rapidly at high transducer gain. Flow cytometry is demonstrated with microfluidic integration. Furthermore, the system has been adapted for molecular sensing.

1.3 Structure of the Dissertation

In Chapter 2, the CMOS-based electronic calibration (E-Cal) algorithm for vector network analyzer (VNA) measurements is presented. We will start with the problem of de-embedding with three unknowns. The evolution of the algorithm for full VNA calibration involving seven unknowns will be discussed. Design non-idealities are highlighted followed by measurement results from 10 – 65 GHz. In Chapter 3, the fundamentals of dielectric spectroscopy, sensor topologies, and the system architecture for instrumentation miniaturization are presented. The design of a 1 – 50 GHz CMOS broadband impedance analyzer is discussed followed by aqueous solution measurements.

In Chapter 4, we will present the design of a highly sensitive microwave capacitive sensor with sub-aF noise floor for high-throughput label-free flow cytometry. The theory of injection-locked oscillator for sensing applications is analyzed with detailed discussions on the sensor robustness. Microfluidic integrations as well as flow cytometry measurements are presented. Chapter 5 adapts the sensor architecture proposed in Chapter 4 for molecular sensing. Technique for flicker noise reduction is discussed. Finally, Chapter 6 concludes this research work and suggests future research directions.

Chapter 2

Electronic Calibration in CMOS

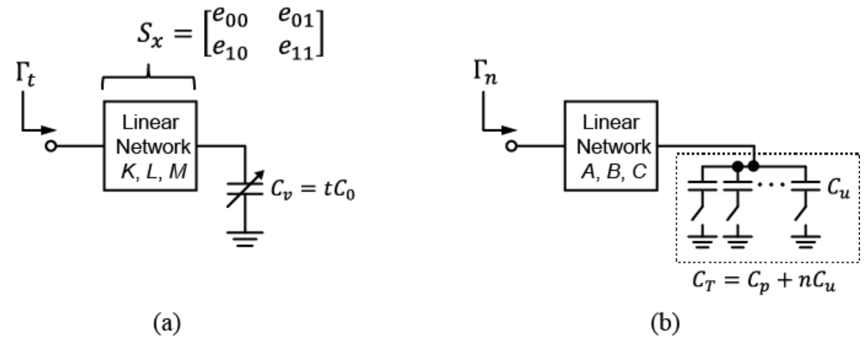

Figure 2.1: One-port calibration using (a) varactor with known capacitance value at each biasing point and (b) CMOS switched-capacitors with unknown parasitic capacitance Cp.

2.1 One-port Electronic Calibration

The first electronic VNA calibration was proposed in 1970 by means of varactors [10]. As shown in Fig. 2.1(a), the reflection coefficient of a varactor loaded two-port network is

$$\Gamma_L = e_{00} + \frac{e_{01}e_{10}\Gamma_{C_V}}{1 - e_{11}\Gamma_{C_V}} = \frac{e_{00} - \Delta_x\Gamma_{C_V}}{1 - e_{11}\Gamma_{C_V}}, \tag{2.1}$$

$$\Delta_x = e_{00}e_{11} - e_{01}e_{10}. \tag{2.2}$$

Such an expression can be expressed as bilinear transformation of *t*, which represents the normalized capacitance of the varactor:

$$\Gamma_L = \frac{Kt + L}{Mt + 1}, \tag{2.3}$$

In (2.3), K, L, and M are the transformation constants describing the network and can be solved if t is known. One can apply the same technique using on-chip switched-capacitors in CMOS (Fig. 2.1(b)). By including an array of these tiny switched-capacitors and enabling each of them sequentially, the measured reflection coefficient can be expressed as

$$\Gamma_n = \frac{An + B}{Cn + 1}, \tag{2.3}$$

with n an integer number representing the number of activated switched-capacitors in the array and the A, B, and C are another set of transformation constants. With at least two measurements, both A/C and B can be solved analytically with significant implications. Intuitively, as n goes to infinity, the impedance of the capacitor resembles an ideal short. As a consequence, A/C represents the reflection coefficient of having an ideal short located at the end of the network. In other words, measurement with known termination can be distilled from the raw data. Similarly, transformation constant B implies measurement with an open circuit termination. This is the concept of *load extrapolation* and forms the core theme of the electronic calibration (ECal) in this work.

In the above problem, A and C cannot be solved individually due to the degeneracy of the measurements as n is an integer. C_p is yet another unknown that cannot be found due to insufficient information. Numerical approach such as least-square method can potentially be used to *fit* the unknowns A, B, and C as in [10]; however, this type of solution finding is not acceptable in precision calibration.

In the next section, we apply the concept of *load extrapolation* to two-port electronic calibration. With the versatility of matrix manipulation, we will show that such calibration problem can be solved without any approximations.

2.2 Two-Port Electronic Calibration

Fig. 2.2 illustrates the general idea of the proposed two-port electronic calibration technique. In order to preserve the clarity of the equations and to arrive at fair comparison to on-wafer TRL, the problem has been narrowed to de-embedding the parasitic effects of the probing pads and the interconnections. The same concept can be adapted to full VNA calibration, which will be described in section 2.6. In this example, both the left (S_x) and the right (S_y) error boxes are assumed to be identical with ports being swapped, resulting in total three unknowns to be solved (e_{00}, e_{11}, and e_{01} = e_{10} assuming the network is reciprocal). In contrast to TRL which mandates three calibration standards, the aim of this research is to solve for all three unknowns from a collection of S-parameter measurements by applying impedance modulation on a single structure. In addition, this must be accomplished without any prior knowledge of the actual impedance value. One

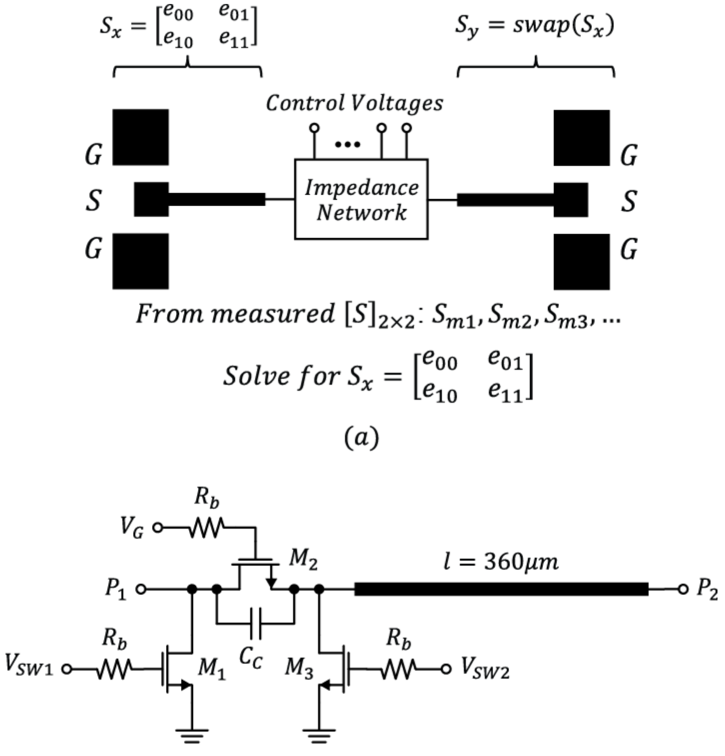

(a)

(b)

Figure 2.2: (a) General concept of the single-element electronic calibration. (b) Implemented impedance network.

example of the impedance network is shown in Fig. 2.2(b) which comprises three NMOS transistors ($M_{1\text{-}3}$) serving as impedance modulators and a transmission line (t-line) with known length but unknown propagation constant (γ) and characteristic impedance (Z_0). The impedance of each device is controllable through individual gate bias in an analog fashion.

2.2.1 Extrapolation

The first step in the proposed algorithm is to convert the measured $[S]_{2\times2}$ into one-port reflection measurements (Γ) with known termination. To achieve this, two $[S]_{2\times2}$ measurements, only differing in the impedance state of one of the shunt NMOS transistors, are collected. As shown in Fig. 2.3(a), these measured $[S]_{2\times2}$ are described using T-matrices:

$$T_{m1} = T_x T_{Y_1} T_{Z_2} T_{Y_3} T_l T_y, \tag{2.4}$$

$$T_{m2} = T_x T_{Y_1'} T_{Z_2} T_{Y_3} T_l T_y, \tag{2.5}$$

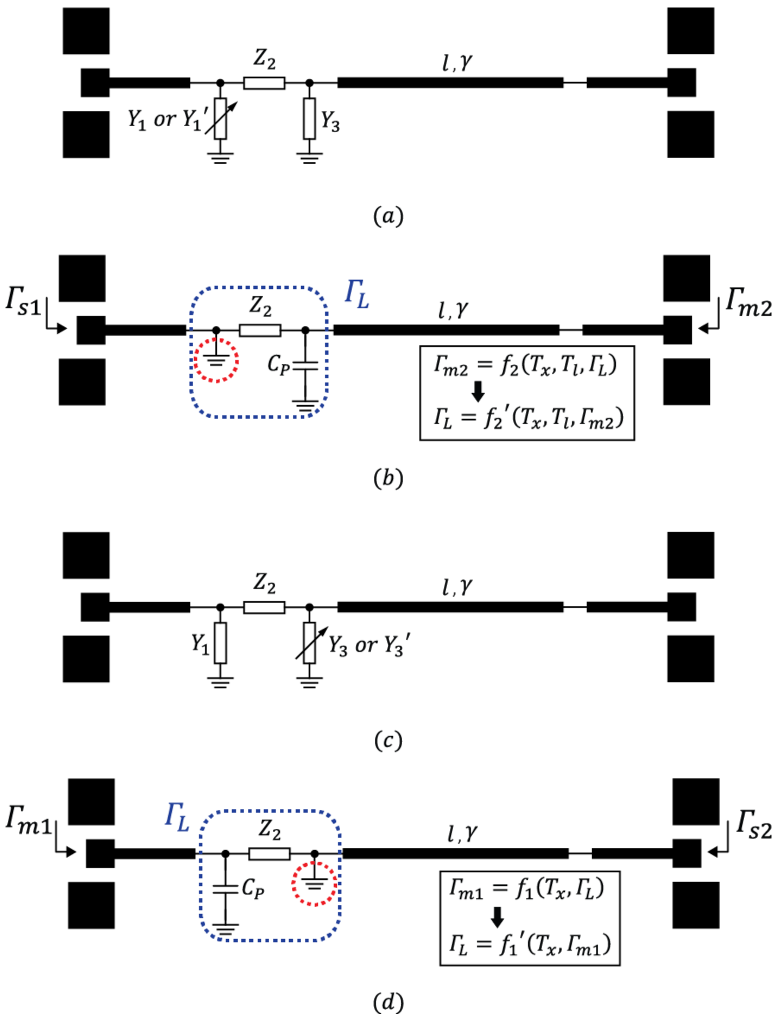

Figure 2.3: (a)(c) Impedance states at each measurement. (b)(d) Derived reflection measurements with ideal short terminations.

where T_x and T_y represents the test fixtures (or the error boxes) on both sides, T_{Y_1} and $T_{Y_1'}$ are the *T*-matrices of M_1 modulated at different impedance states, and T_{Z_2}, T_{Y_3}, and T_l are the *T*-matrices of M_2, M_3, and the inserted t-line, respectively. Multiplying T_{m_2} with the inverse of T_{m_1}, we arrive at

$$T_m = T_{m2}(T_{m1})^{-1} = T_x T_{Y_1'} \left(T_{Y_1}\right)^{-1} (T_x)^{-1}. \qquad (2.6)$$

Note that the *T*-matrix of shunt admittance exhibits the following property:

$$T_{Y_1}\left(T_{Y_2}\right)^{-1} = T_{Y_1 - Y_2} = T_{\Delta Y} = \begin{bmatrix} 1 - \frac{\Delta Y Z_0}{2} & -\frac{\Delta Y Z_0}{2} \\ \frac{\Delta Y Z_0}{2} & 1 + \frac{\Delta Y Z_0}{2} \end{bmatrix}. \qquad (2.7)$$

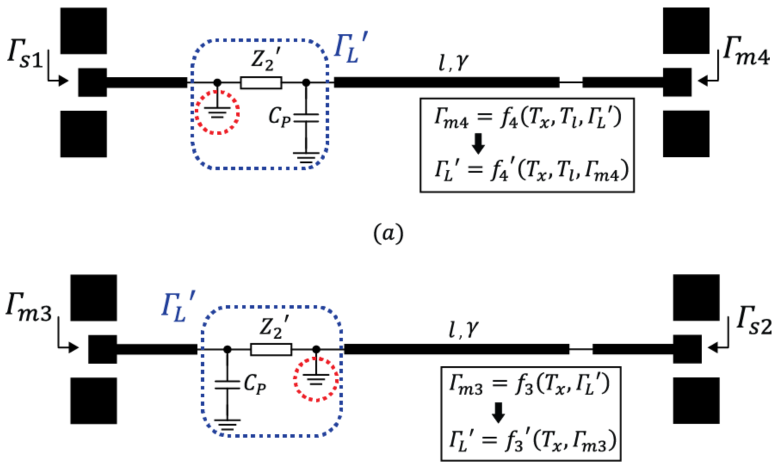

(a)

(b)

Figure 2.4: Derived reflection measurements with ideal short terminations located at (a) left and (b) right side of π-network.

Consequently, (2.6) can be grouped as

$$(T_m - I_{2\times 2})T_x = T_m' T_x = T_x \frac{\Delta Y Z_0}{2} \begin{bmatrix} -1 & -1 \\ 1 & 1 \end{bmatrix}. \tag{2.8}$$

By expanding (2.8), the following equality is derived:

$$\frac{x_{11} - x_{12}}{x_{21} - x_{22}} = -\frac{m_{12}}{m_{11}}. \tag{2.9}$$

Here m_{11} and m_{12} are the elements in the T_m' and x_{11}, x_{12}, x_{21}, and x_{22} are the elements in T_x. Note that the left side of (2.9) is equivalent to the reflection coefficient (Γ_{s1}) with an *ideal short* terminating Y_1, i.e. the position of modulation (Fig. 2.3(b)). In other words, a measurement with *known* termination is extrapolated without any knowledge of the actual Y_1. This is of no surprise if one observes carefully on the T-matrix of the shunt admittance in (2.7) and (2.8) where an *ideal short* exists in the admittance matrix. Such extrapolation forms the foundation of the proposed algorithm. It is worth mentioning that the equations here are very similar to TRL when extracting the propagation constant of the t-line.

By reversing T_{m1} and T_{m2} and repeating (2.6) – (2.9), Γ_{m2}, the reflection coefficient of the test fixture loaded with t-line and Z_2 in parallel with Y_3 (shown as C_p in Fig. 2.3(b)), is derived. Similarly, the procedure is applied after collecting measurements from modulating Y_3 (Fig. 2.3(c) and (d)). The derived reflection measurements are Γ_{s2} and Γ_{m1}.

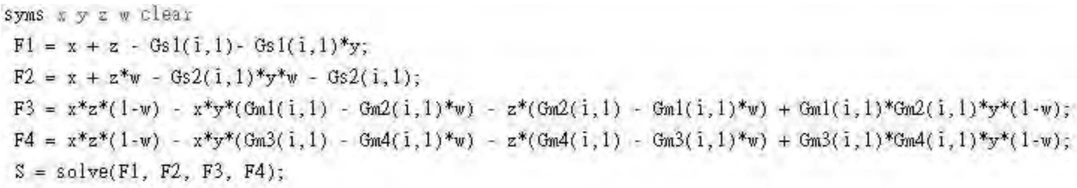

```
syms x y z w clear
 F1 = x + z - Gs1(i,1)- Gs1(i,1)*y;
 F2 = x + z*w - Gs2(i,1)*y*w - Gs2(i,1);
 F3 = x*z*(1-w) - x*y*(Gm1(i,1) - Gm2(i,1)*w) - z*(Gm2(i,1) - Gm1(i,1)*w) + Gm1(i,1)*Gm2(i,1)*y*(1-w);
 F4 = x*z*(1-w) - x*y*(Gm3(i,1) - Gm4(i,1)*w) - z*(Gm4(i,1) - Gm3(i,1)*w) + Gm3(i,1)*Gm4(i,1)*y*(1-w);
 S = solve(F1, F2, F3, F4);
```

Figure 2.5: A snapshot of implemented Matlab codes.

2.2.2 Impedance Sharing

Up to this point, only Γ_{s1} and Γ_{s2} are considered useful as Γ_{m1} and Γ_{m2} are still loaded with an unknown termination Γ_L. This is insufficient as four unknowns (including γ of t-line) requires a minimum of four measurements to be solvable. In fact, the π-network shown in the schematic is designed such that Γ_{m1} and Γ_{m2} shares the series branch Z_2; in other words, both measurements have identical load termination. This allows the merging of Γ_{m1} and Γ_{m2} by inverting each measurement, isolate the common term Γ_L, and equating the two expressions with Γ_L serving as a bridge (Fig. 2.3(b) and (d)). The expression is now useful as no additional variable has been introduced. It is important to mention that the proposed technique is inspired by LRRM [11].

One might argue that the mismatch contributed by the off-state parasitic capacitance (C_p) at both sides of Z_2, primarily from the transistor source/drain junction, will deteriorate our assumption on impedance sharing. To remedy this, Z_2 can be chosen to be much smaller (30 ~ 70 Ω) than the mismatch-induced impedance difference. Such junction capacitance exhibits 7 bits of matching from foundry device model.

Lastly, we modulate the impedance of Z_2 to a different state (Z_2') and repeat the entire procedure. As shown in Fig. 2.4, Γ_{m3} and Γ_{m4} also shares an identical termination (Γ_L'). After merging the two, a useful measurement free of unknown termination is derived.

2.2.3 Equation solving

With a total of six reflection measurements, we arrived at the following four non-linear equations:

$$xz(1-w) - xy(\Gamma_{m1} - \Gamma_{m2}w) - z(\Gamma_{m2} - \Gamma_{m1}w) + \Gamma_{m1}\Gamma_{m2}y(1-w) = 0, \quad (2.10)$$

$$xz(1-w) - xy(\Gamma_{m3} - \Gamma_{m4}w) - z(\Gamma_{m4} - \Gamma_{m3}w) + \Gamma_{m3}\Gamma_{m4}y(1-w) = 0, \quad (2.11)$$

$$x + z - \Gamma_{s1} - \Gamma_{s1}y = 0, \quad (2.12)$$

$$x + zw - \Gamma_{s2} - \Gamma_{s2}yw = 0, \quad (2.13)$$

where $x = e_{00}$, $y = e_{11}$, $z = e_{00}e_{11} - e_{01}e_{10}$, and $w = \mathrm{e}^{-2\gamma l}$. Merging the equations results in a 5th-order polynomial equation. The solution can be found numerically using *solve* in Matlab. Fig. 2.5 shows a snapshot of the Matlab code.

2.2.4 Impedance renormalization

Up to this point, the extracted S_x is normalized to the Z_0 of the on-chip t-line. To solve for such unknown Z_0, we take advantage of the shunt switches (M_1 and M_3) in the π-network, which will serve as on-chip *calibration* standards.

From 2.2.1, we have shown how reflection measurement terminated with an ideal short can be derived mathematically. On the other hand, network duality tells us that reflection measurements terminated with an *ideal open* can also be extracted in a similar way. To see this, we notice that the T-matrix of any arbitrary series impedance Z reference to Y_0 is described by (Fig. 2.6(a))

$$T_Z = I_{2x2} + \frac{ZY_0}{2}\begin{bmatrix} -1 & 1 \\ -1 & 1 \end{bmatrix}, \tag{2.14}$$

Applying the procedure of (2.4) – (2.6) with two measured $[S]_{2\times 2}$ differing only in Z_2 (T_{m3} and T_{m4} in Fig. 2.6(b)) leads to the following expression similar to (2.8):

$$(T_{m4}(T_{m3})^{-1} - I_{2\times 2})T_x T_{Y1} = T_x T_{Y1} \cdot \frac{\Delta Z Y_0}{2}\begin{bmatrix} -1 & 1 \\ -1 & 1 \end{bmatrix}. \tag{2.15}$$

The following equality is derived after some algebra:

$$\frac{x_{11}' + x_{12}'}{x_{21}' + x_{22}'} = -\frac{m_{12}'}{m_{11}'}. \tag{2.16}$$

Here m_{11}' and m_{12}' are the elements in $T_{m4}(T_{m3})^{-1} - I_{2\times 2}$ and x_{11}', x_{12}', x_{21}', and $x_{22}'$are the elements in $T_x T_{Y1}$. Note that the left side of (2.16) is now equivalent to the reflection coefficient (Γ_{o1}) with an open termination. As S_x is known, Γ_{Y1} is found:

$$\Gamma_{Y_1} = \frac{e_{00} - \Gamma_{o1}}{\Delta_x - e_{11}\Gamma_{o1}}. \tag{2.17}$$

The procedure is repeated twice with transistor M_1 turned on and off, leading to two expressions of the normalized admittance at different biasing:

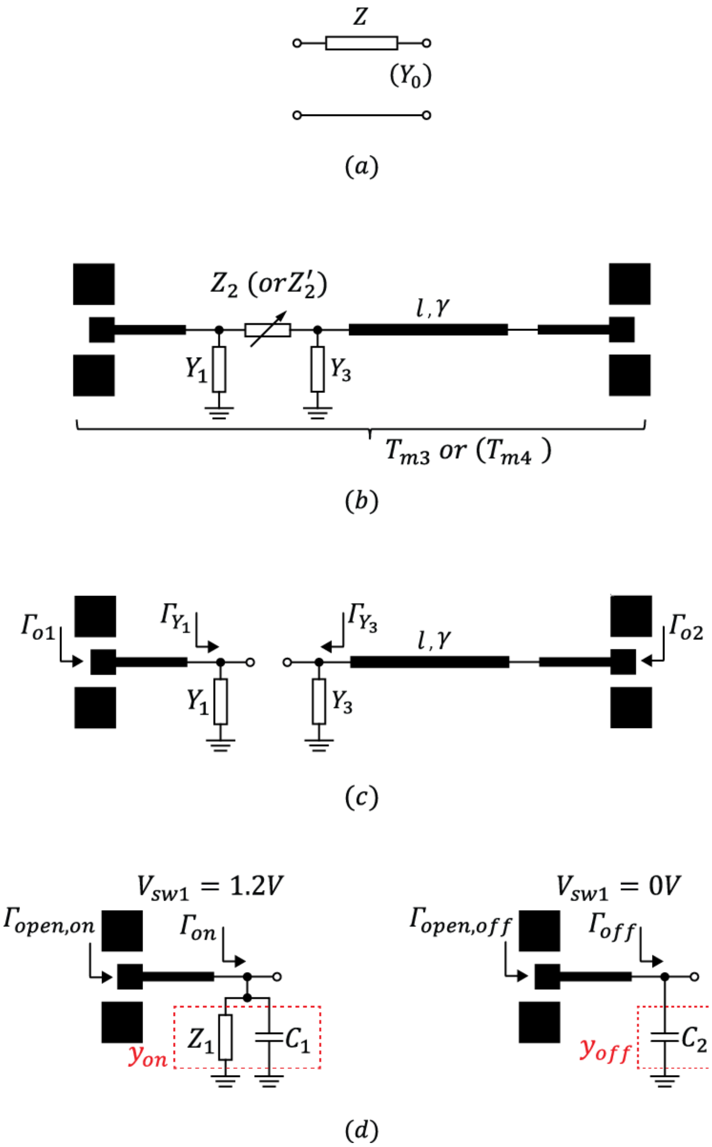

Figure 2.6: (a) Series impedance network. (b) $[S]_{2\times2}$ when modulation Z_2. (c) Reflection measurements with open terminations. (d) Equivalent circuit models of M_1 in its on (left) and off (right) states.

$$y_{on} = \frac{Z_0}{Z_1} + j\omega Z_0 C_1, \tag{2.18}$$

$$y_{off} = j\omega Z_0 C_2. \tag{2.19}$$

Here Z_1 represents the on-state impedance of M_1 and C_1 and C_2 model the corresponding capacitance loading.

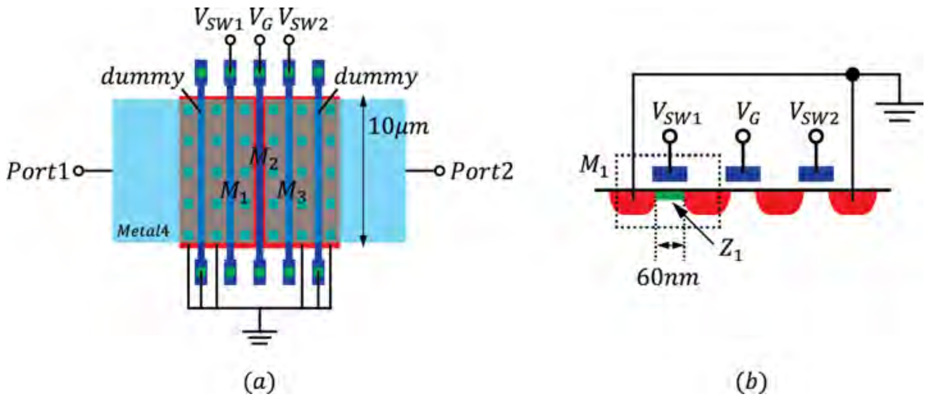

Figure 2.7: (a) Layout and (b) cross-section of the π-network.

Before moving on, let's study the physical location, layout, and the cross-section of the π-network as shown in Fig. 2.7. It is observed that the modulation of impedance occurs within the transistor channel having a longitudinal geometry on the order of tens of nm in deep sub-micron CMOS. Such fine length allows us to approximate Z_1 with a frequency independent resistance as the phase shift is negligible even at sub-THz frequencies. By modeling Z_1 with a constant resistance R_1 whose value can be measured at DC, Z_0 is found assuming $C_1 \approx C_2$:

$$Z_0 = R_1 \cdot (y_{on} - y_{off}). \tag{2.20}$$

2.2.5 Via Exclusion

The reference plane in the conventional TRL calibration is located at the center of the *thru* structure, as indicated in Fig. 2.8(a). From DUT perspective, the reference plane is at the signal layer of the t-line, which is usually on the top most metal layer, e.g. M9 in TSMC 65-nm CMOS. As a consequence, the de-embedded DUT S-parameter includes the accessing vias connecting the signal line from the device ports. On the other hand, the reference plane in the proposed π structure is located at the junction of the two nearby impedances, as shown in Fig. 2.8(b). This enables the engineering of the reference planes in the layout. By having all the impedance modulators in close proximity, as shown in the layout of Fig. 2.7 and Fig. 2.8(c), such reference plane can be shifted to a lower metal layer such as M4. Hence the effect of accessing vias can be excluded from the DUT without multi-structure and multi-steps of de-embedding. Such unique feature enables the measurement of the DUT intrinsic performance for the first time. From the simulation, these accessing vias result in a dB reduction in the transistor gain at frequency above 150 GHz. Unfortunately, the effect of via exclusion cannot be verified in the experiment yet due to frequency capability of the measurement setup.

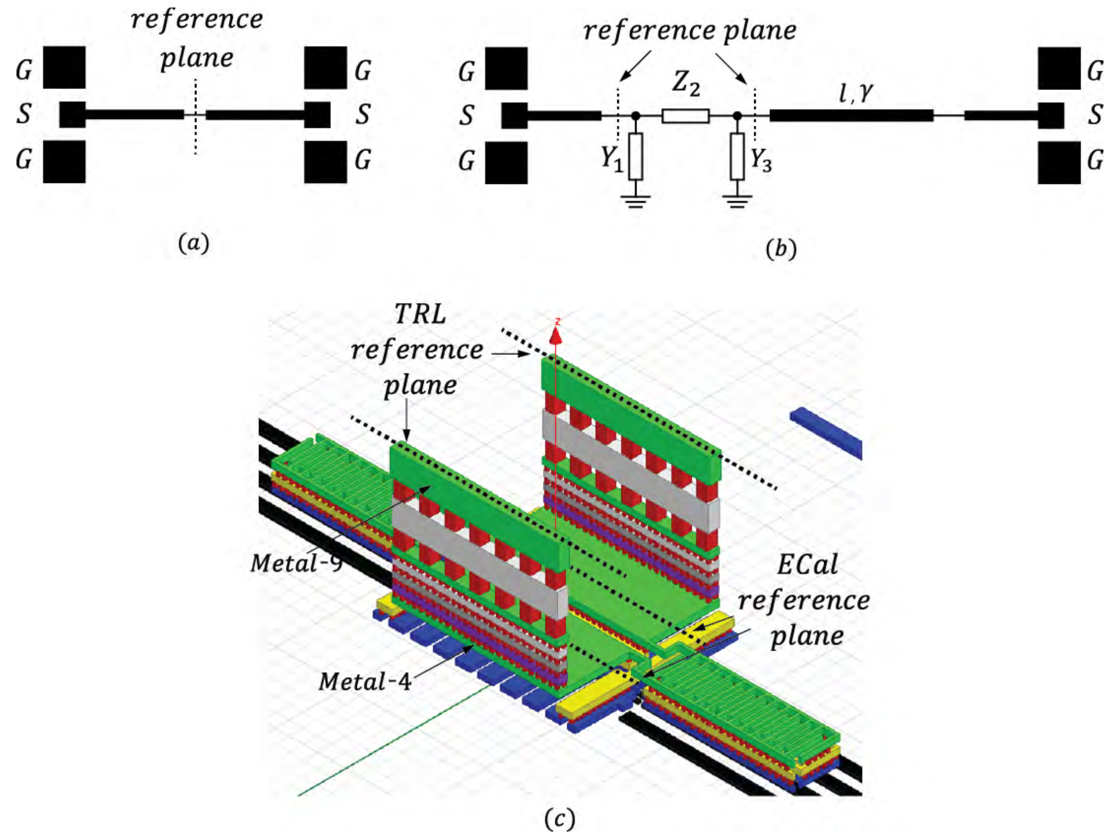

Figure 2.8: (a) Reference plane in TRL thru structure. (b) Reference plane in CMOS ECal. (c) 3D layout view indicating the location of reference planes.

2.3 Design Considerations

The robustness of the algorithm is verified through Monte Carlo simulation by quantifying the error sensitivity in both the extrapolation and the impedance-sharing steps. Uncorrelated noise with known variance are introduced in each element of the measurement $[S]_{2\times2}$ and the output variances are calculated. The algorithm is regarded as numerically stable if the solution converges. Optimization of design parameters can be carried out in the same way by minimizing the error sensitivity. Such numerical experiments allow rapid evaluation of the algorithm robustness against design parameters including the modulated impedance values and the length of t-line. Note that the analytical forms of noise sensitivity can be derived using perturbation analysis with the use of noise matrix, similar to the approach taken in multiline TRL (mTRL) [5]. This can potentially provide more design insights when weighting functions are introduced in the optimization process.

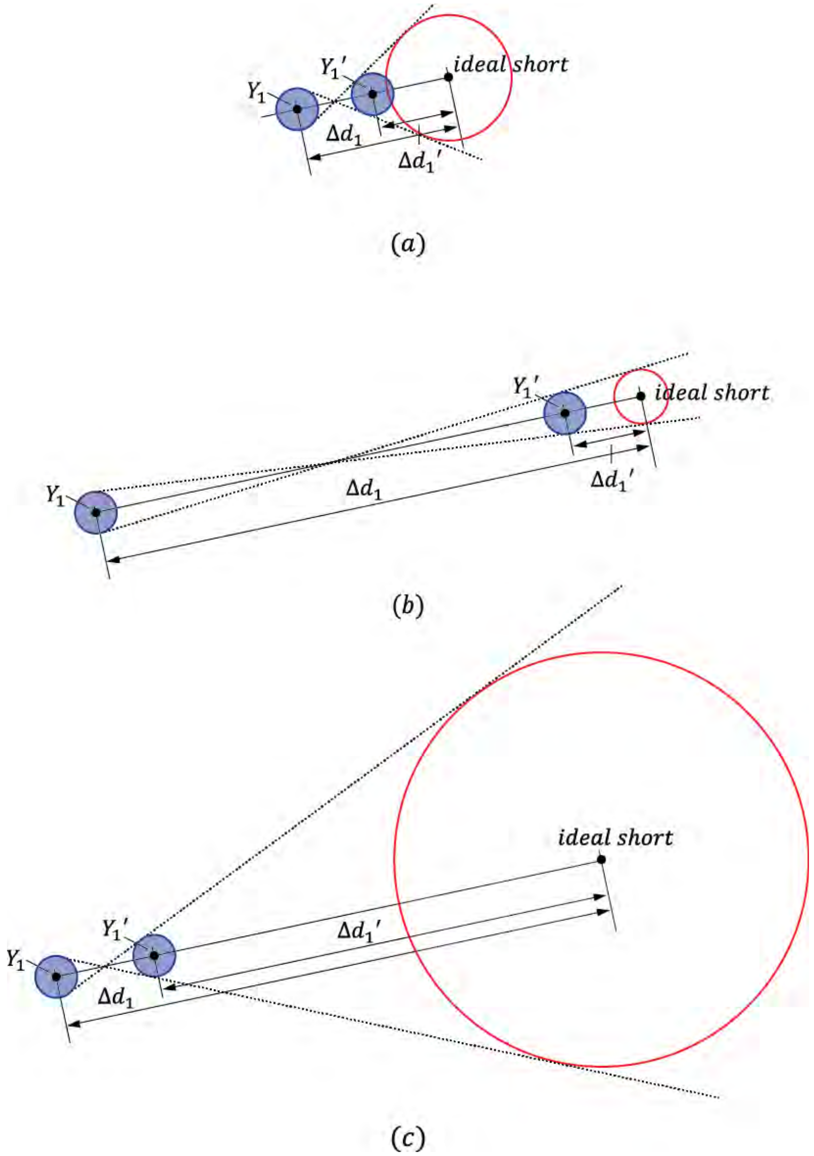

Figure 2.9: Error amplification in the extrapolation step with different combination of Δd_1 and $\Delta d_1'$.

There are two major design considerations due to non-idealities: error amplification in the extrapolation step and bandwidth limitation in the equation solving step. We will discuss them separately in the following subsections.

2.3.1 Error Amplification

The error sensitivity in the extrapolation step depends heavily on the impedance distances to the ideal short. This can be understood graphically with Fig. 2.9 where

$$\Delta d_1 = \left|\frac{1}{Y_1} - Z_{short}\right|, \tag{2.21}$$

$$\Delta d_1{}' = \left|\frac{1}{Y_1{}'} - Z_{short}\right|. \tag{2.22}$$

The blue circles represent the amount of uncertainty due to measurement error including random noise. From the figure, we can draw two conclusions. First, it is desirable to minimize $\Delta d_1'/\Delta d_1$ ratio such that the amount of error amplification can be limited (Fig. 2.9(b)). This motivates the selection of NMOS switches instead of varactors as impedance modulators. Next, the error sensitivity is always larger than unity. This results in higher output uncertainty when compared with TRL in the simulation. Fortunately, such noise can be reduced using redundant measurements in the optimization flow as long as the measurement uncertainty remains random. We will study the impact of such error sensitivity in more details from the experiments in section 2.4.

2.3.2 Bandwidth Limitation

As traveling waves on a t-line exhibits frequency-dependent phase shift, the measurement bandwidth is limited. At low frequency, the solution exhibits higher sensitivity to the measurement uncertainty since the phase shift is small. This is equivalent to having a smaller signal-to-noise ratio (SNR) in analogy to a communication system. On the other hand, as frequency approaches integer multiples of $\lambda/4$, numerical stability suffers. Fig. 2.10 shows an example of Monte Carlo simulation at different t-line length.

On the other hand, it is crucial to keep the measurement impedance as close to 50 Ω (or the impedance of the VNA system) as possible to minimize systematic error. Hence care must be taken to minimize that the parasitic capacitance of the shunt admittances to avoid shorting the signal currents at very high frequency. Similarly, it is desirable to maintain low series impedance in the π-network to maintain sufficiently high S_{21}. To achieve this, additional capacitance can be placed in shunt with the series impedance modulator. Given such considerations, two sets of designs are implemented with the first measuring frequencies below W-band (< 110 GHz) and the other covering G-band (140 – 220 GHz).

2.3.3 Implementation

Fig. 2.11 shows the die photo of the 110-GHz test structure fabricated in 65-nm CMOS. Microstrip t-lines with 6-μm signal width at M9 on top of a ground plane constructed with a mesh of M1 and M2 is implemented (Z_0 ~ 52 Ω from HFSS at 60 GHz). The length of the t-line in this particular example is 360 μm, equivalent to 45°

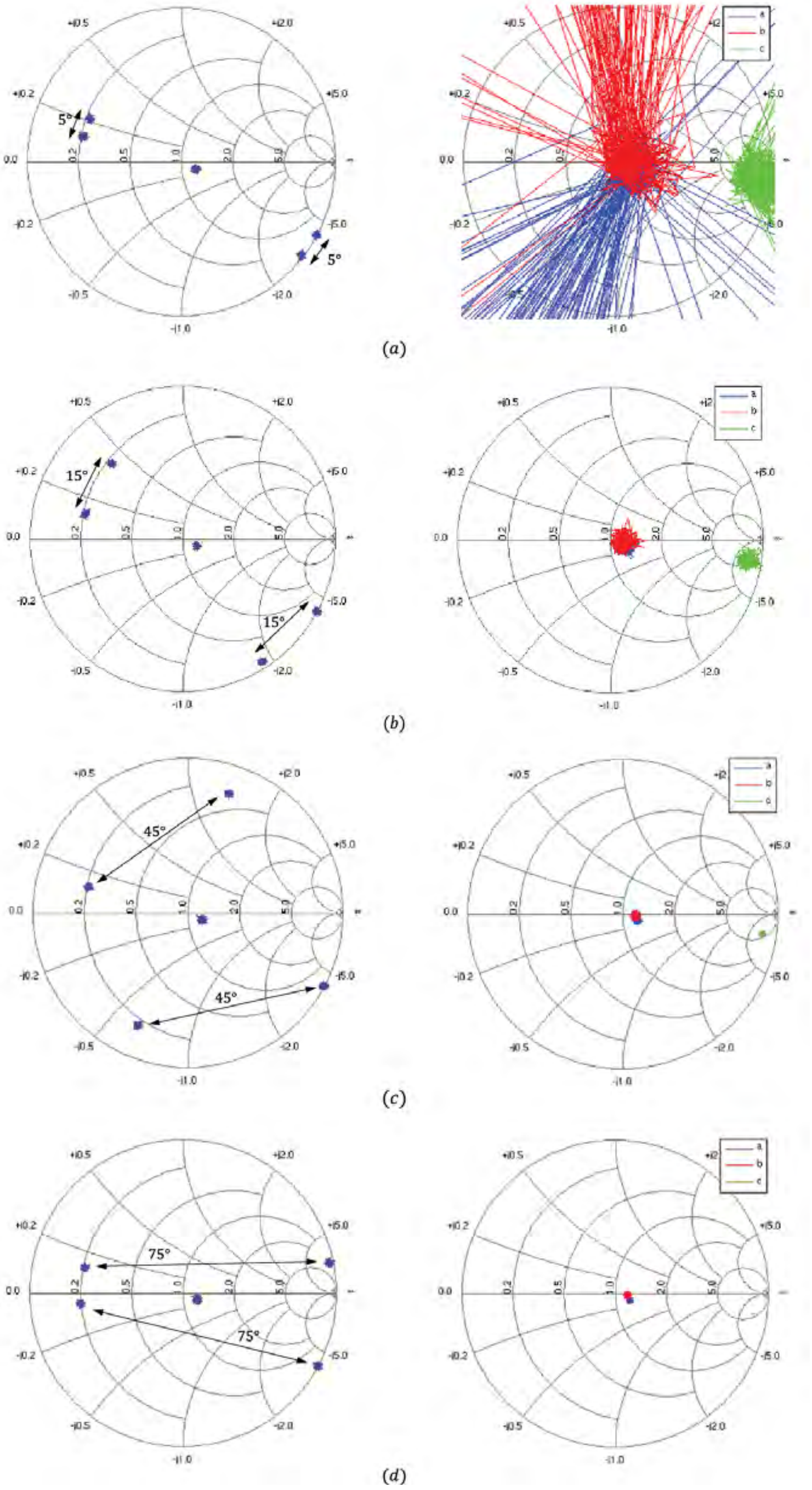

Figure 2.10: The effect of t-line length on noise sensitivity. All left plots represent the reflection measurements on the Smith Chart with t-line length quantified by the amount of phase shift. All right plots represent the extracted solutions.

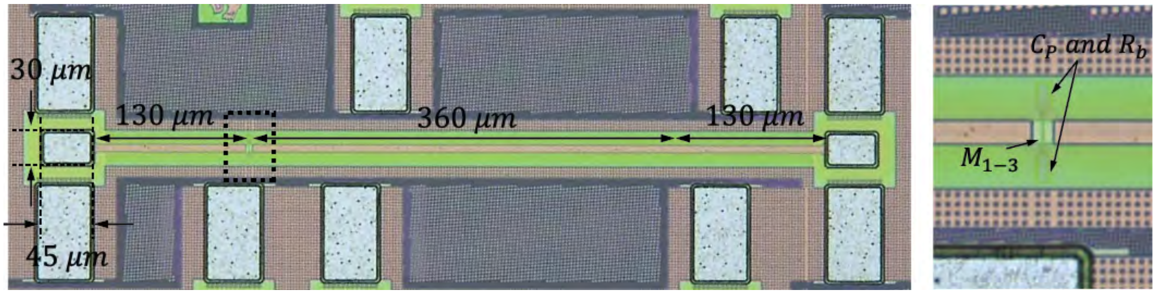

Figure 2.11: Calibration structure micrograph.

phase shift at 50 GHz. NMOS gates, all single-finger with W/L of 10-µm/60-nm, are floated with 20 kΩ unsalicided poly-resistors having a width of 0.4 µm while the body is also floated with undoped silicon similar to T/R switch design to reduce parasitic loading [12]. A 44-fF MOM capacitor (C_c) is added to lower the series impedance (Z_2) when M_2 is completely off. This keeps S_{21} higher than -12 dB at 10 GHz.

To minimize parasitic capacitance, transistors for the G-band test structures are scaled to 6-µm/60-nm while t-line length is reduced to 160 µm, equivalent to 80° at 200 GHz.

2.4 Experimental Results

First, SLOT calibration is performed at the probe tips using ISS from Cascade Microtech with R&S ZVA-67 VNA. The output power at VNA ports is kept below -10 dBm. The extracted γ of MSL is shown in Fig. 2.12, demonstrating reasonable accuracy compared to TRL from 10 – 65 GHz. In fact, the extracted α with the proposed approach matches closer to the HFSS simulation. Different reflection coefficients derived in the algorithm are plotted in Fig. 2.13. Each of them shows the expected behavior. Fig. 2.14 compares Γ_{s1} to the S_{11} and S_{22} of a short structure on the Smith Chart. Fig. 2.15 compares the extracted test fixture S-parameter from the two approaches.

Fig. 2.16(a) shows the DC equivalent circuit of the de-embedding structure in the measurement setup taking into account the wiring resistance $R_{p1} – R_{p4}$. The network can be further simplified to five unknowns by ensuring the current returns from the same port. These unknown resistances are found through different combination of impedance states in $M_{1\text{-}3}$. In order to maintain consistent R_{p1} and R_{p2}, a customed switching network is soldered on a PCB (Fig. 2.16(b)).

Fig. 2.17 shows the calculated Z_0 and the equivalent t-line circuit elements, exhibiting the expected frequency dependency. Comparing to TRL *calibration comparison method* [13 – 14], our single-element approach captures the increase of the line conductance ($G_{\text{p.u.l.}}$) surprisingly well but suffers from higher error in the line resistance ($R_{\text{p.u.l.}}$). The accuracy could be limited by the deviation of C_1 and C_2 at different transistor biasing.

As mentioned in section 2.3.1, it is desirable to have sufficient wide distance between the two modulated impedances to minimize error amplification. Therefore, varactors are

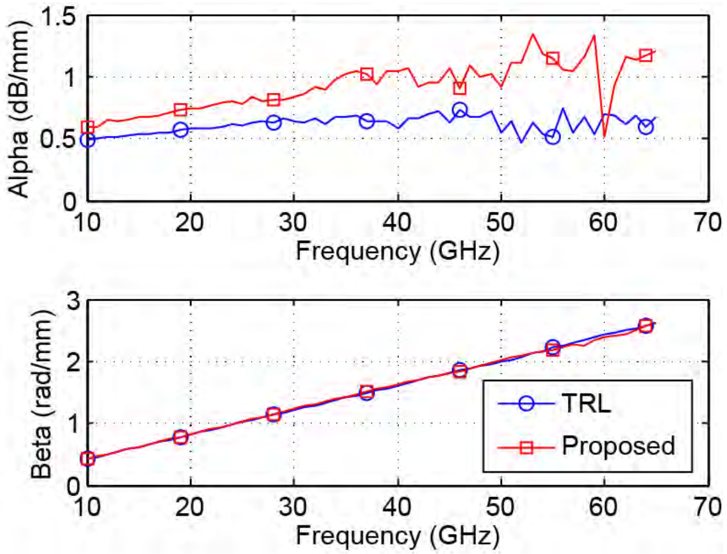

Figure 2.12: Extracted t-line propagation constant.

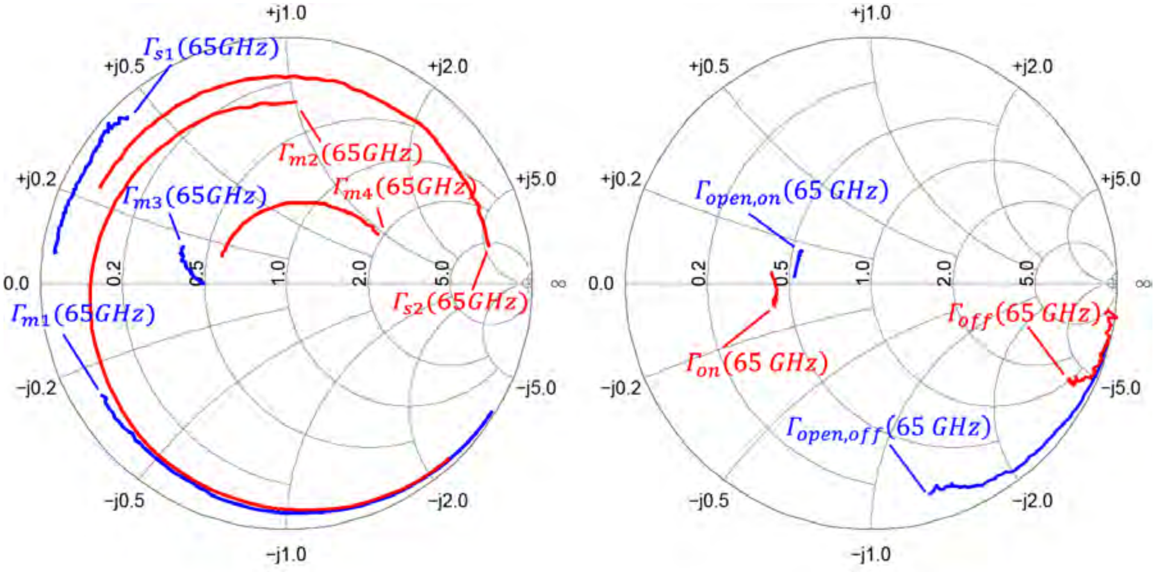

(a) (b)

Figure 2.13: Reflection measurements with (a) short terminations and (b) open terminations.

not suitable to serve as impedance modulators. This effect can be observed in our first prototype chip where varactors with capacitance change on the order of 4 fF are implemented. Fig. 2.18 shows the schematics of the structure, the die photo, and the extracted offset-short measurements at 30 GHz. It is found that the results are far off from the unity circle on the Smith Chart. This experiment indicates that careful design of the impedance modulator is necessary to achieve high precision.

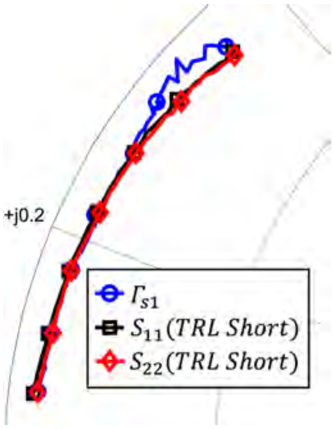

Figure 2.14: Comparison between ECal extracted reflection measurements terminated with ideal short and measured reflection coefficients from TRL short structure.

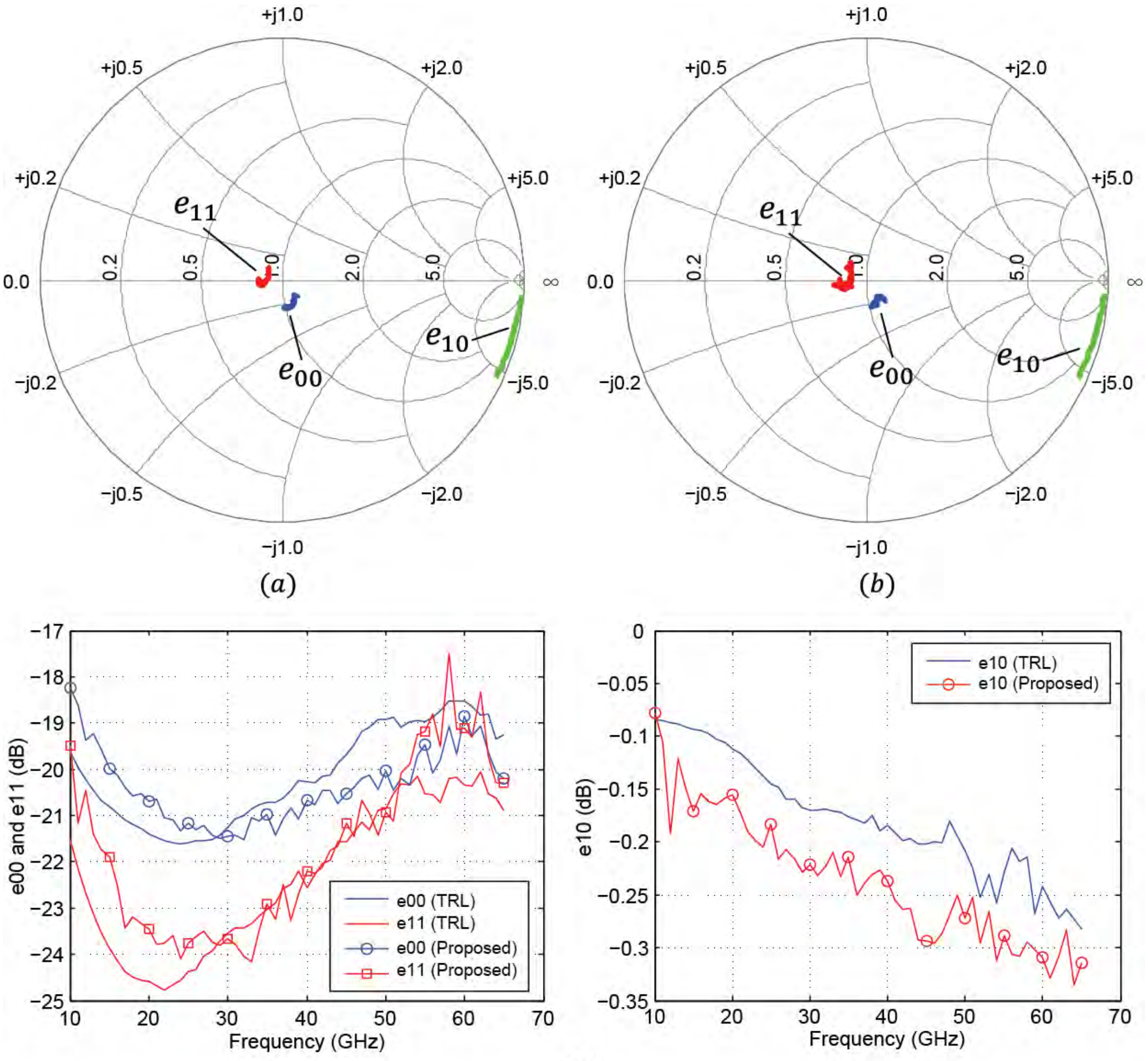

(a) (b)

(c)

Figure 2.15: Extracted S_x: (a) TRL and (b) proposed algorithm. (c) S_x in log-mag format.

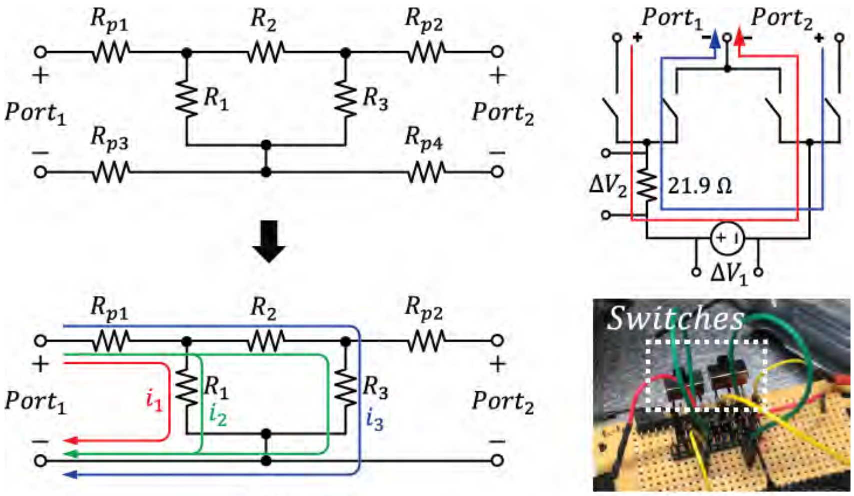

(a) (b)

Figure 2.16: (a) DC equivalent circuit and (b) customed switch network.

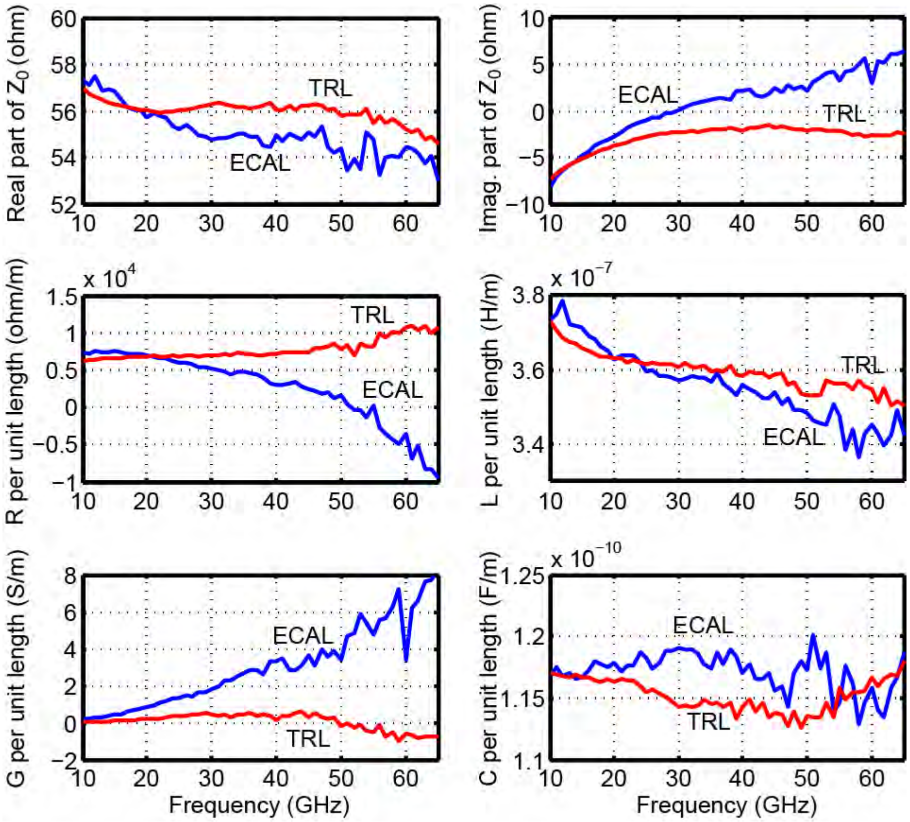

Figure 2.17: Extracted Z_0 and the t-line circuit parameters with TRL and the proposed electronic calibration.

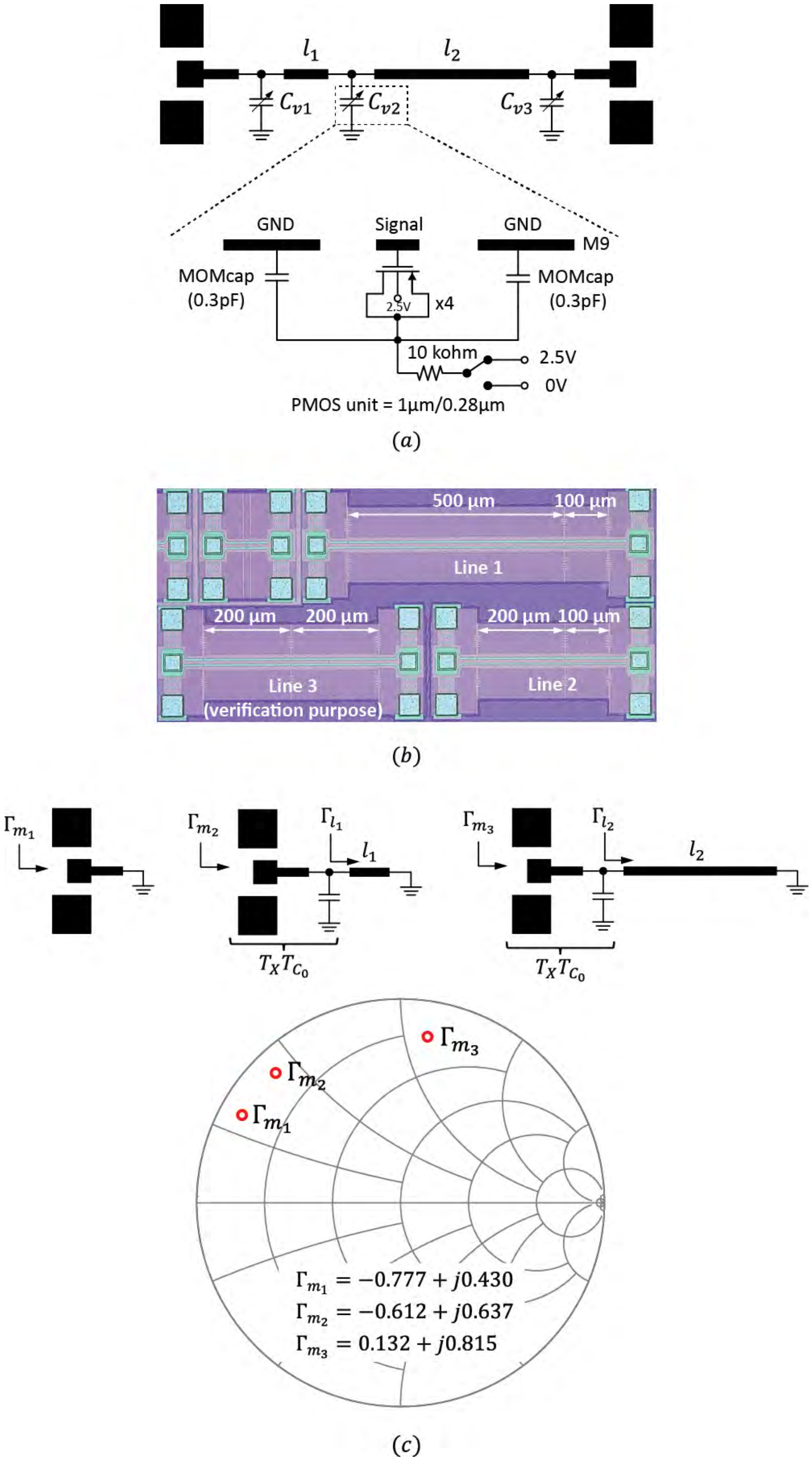

Figure 2.18: (a) The schematic and (b) the layout of ECal structure with varactors as impedance modulators (c) The extracted reflection measurements when terminating with ideal short.

2.5 Two-element VNA Calibration

In the previous section, single-element calibration dedicated for de-embedding of probing components has been described. This section discuss how the concept can be adapted to full VNA calibration where there are total eight unknowns to be solved (Fig. 2.19). As either one of the transmission terms ($e_{10}e_{32}$ or $e_{01}e_{23}$) is sufficient, the number of unknowns is reduced to seven. In this section, a two-element approach without bandwidth limitation is presented.

Fig. 2.20 shows the required structures for VNA calibration evolved from the proposed electronic calibration algorithm. The first element consists of the same π-network but without the t-line. The second element is a simple *thru* structure, which offers an additional four measurements to accommodate for doubling the number of the unknowns. In order to retain the same via-exclusion property, the reference plane of the *thru* is located at the center of a metal bridge positioned on M4 as shown in Fig. 2.20(b). In the next section, we will describe additional techniques necessary to solve for all the unknowns.

2.5.1 Open Measurement in Two-element ECal

The inclusion of thru leads to a new reflection measurement where the error box is loaded with an *ideal open*, as shown in Fig. 2.21(a). Here we will show how to arrive at this conclusion.

First, the *thru* measurement is described again with T-matrices:

$$T_{thru} = \begin{bmatrix} t_{11} & t_{12} \\ t_{21} & t_{22} \end{bmatrix} = T_x T_y. \tag{2.23}$$

$$T_y = {T_x}^{-1} T_{thru}. \tag{2.24}$$

Note that

$$T_x = \frac{1}{e_{10}} \begin{bmatrix} -\Delta_x & e_{00} \\ -e_{11} & 1 \end{bmatrix}, \tag{2.25}$$

$${T_x}^{-1} = \frac{1}{e_{01}} \begin{bmatrix} 1 & -e_{00} \\ e_{11} & -\Delta_x \end{bmatrix}, \tag{2.26}$$

$$T_y = \frac{1}{e_{32}} \begin{bmatrix} -\Delta_y & e_{22} \\ -e_{33} & 1 \end{bmatrix}. \tag{2.27}$$

By inserting (2.25) – (2.27) into (2.24), the following three equalities are found

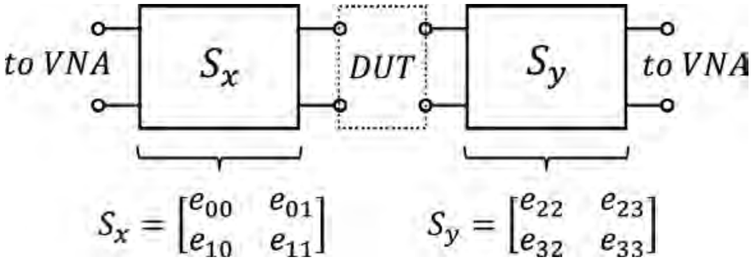

Figure 2.19: Full VNA calibration error model.

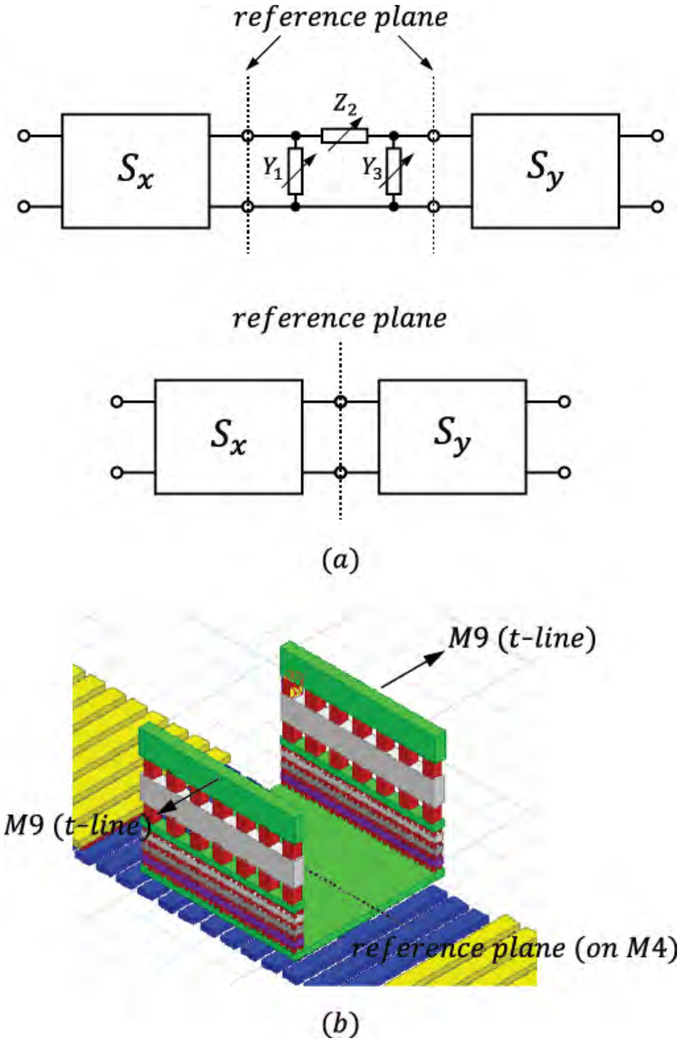

Figure 2.20: (a) Dual-element ECal structures. (b)3D layout illustration of ECal thru.

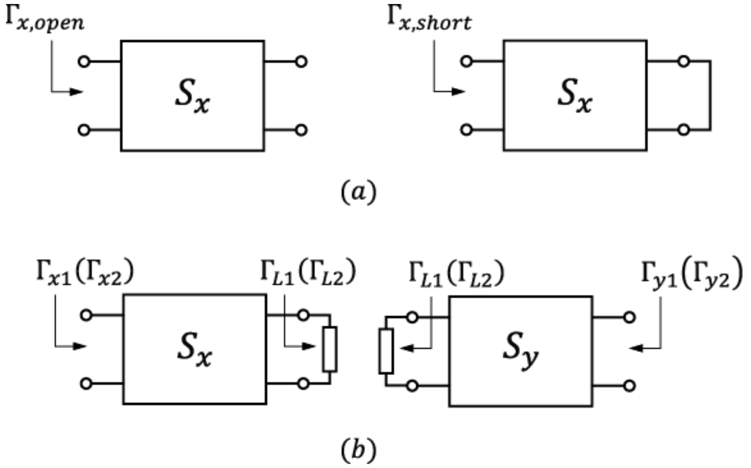

Figure 2.21: (a) Reflection measurements with open (left) and short (right) terminations. (b) Reflection measurements with identical load terminations.

$$\Delta_y = \frac{e_{00}t_{21} - t_{11}}{e_{11}t_{12} - \Delta_x t_{22}}, \tag{2.28}$$

$$e_{22} = \frac{t_{12} - e_{00}t_{22}}{e_{11}t_{12} - \Delta_x t_{22}}, \tag{2.29}$$

$$e_{33} = \frac{\Delta_x t_{21} - e_{11}t_{11}}{e_{11}t_{12} - \Delta_x t_{22}}. \tag{2.30}$$

Note that e_{32}/e_{01} has been substituted with

$$\frac{e_{32}}{e_{01}} = \frac{1}{e_{11}t_{12} - \Delta_x t_{22}}. \tag{2.31}$$

Next, the impedance sharing technique discussed in section 2.2.2 is utilized using the notation in Fig. 2.21(b). The reflection measurements from both left and right ports are

$$\Gamma_{x1} = \frac{e_{00} - \Delta_x \Gamma_{L1}}{1 - e_{11}\Gamma_{L1}}, \tag{2.32}$$

$$\Gamma_{y1} = \frac{e_{33} - \Delta_y \Gamma_{L1}}{1 - e_{22}\Gamma_{L1}}. \tag{2.33}$$

By equating (2.32) and (2.33) by use of share Γ_{L1} and plugging in (2.28) – (2.30):

$$c_1(e_{00}^2 - \Delta_x^2) + c_2(1 - e_{11}^2) + c_3(e_{11}\Delta_x - e_{00}) = 0, \tag{2.34}$$

where c_{1-3} are all measured quantities:

$$c_1 = t_{21} + \Gamma_{y1} t_{22}, \tag{2.35}$$

$$c_2 = \Gamma_{x1} t_{11} + \Gamma_{x1} \Gamma_{y1} t_{12}, \tag{2.36}$$

$$c_3 = t_{11} + t_{21} \Gamma_{x1} + t_{22} \Gamma_{x1} \Gamma_{y1} + \Gamma_{y1} t_{12}. \tag{2.37}$$

Repeating the same procedure at different shared impedance Γ_{L2}, we arrive at

$$c_1{}'(e_{00}^2 - \Delta_x^2) + c_2{}'(1 - e_{11}^2) + c_3{}'(e_{11}\Delta_x - e_{00}) = 0, \tag{2.38}$$

where $c_{1-3}{}'$ have exact the same form as (2.35) – (2.37) except that Γ_{x1} and Γ_{y1} are replaced with reflection measurements when loaded with Γ_{L2}. Solving (2.34) and (2.38) leads to the following expression

$$\frac{e_{00}^2 - \Delta_x^2}{1 - e_{11}^2} = -\frac{c_2 c_3' - c_2{}' c_3}{c_1 c_3' - c_1{}' c_3}. \tag{2.39}$$

Note that the left side of (2.39) can be decomposed into

$$\left(\frac{e_{00} + \Delta_x}{1 + e_{11}}\right)\left(\frac{e_{00} - \Delta_x}{1 - e_{11}}\right) = \Gamma_{x,short} \Gamma_{x,open}. \tag{2.40}$$

Therefore

$$\Gamma_{x,open} = -\frac{1}{\Gamma_{x,short}} \frac{c_2 c_3' - c_2{}' c_3}{c_1 c_3' - c_1{}' c_3}. \tag{2.41}$$

As $\Gamma_{x,short}$ is derived with extrapolation technique discussed in section 2.2.1, $\Gamma_{x,open}$ can be found with (2.41).

2.5.2 Solution Flow in Two-element ECal

In the previous section, the combination of extrapolation and the impedance sharing techniques provides only two reflection measurements, $\Gamma_{x,short}$ and $\Gamma_{x,open}$. This is insufficient to solve for the three unknowns (e_{00}, e_{11}, and Δ_x) in the left error box (S_x). There are two approaches to circumvent this limitation. The first one is to insert a t-line

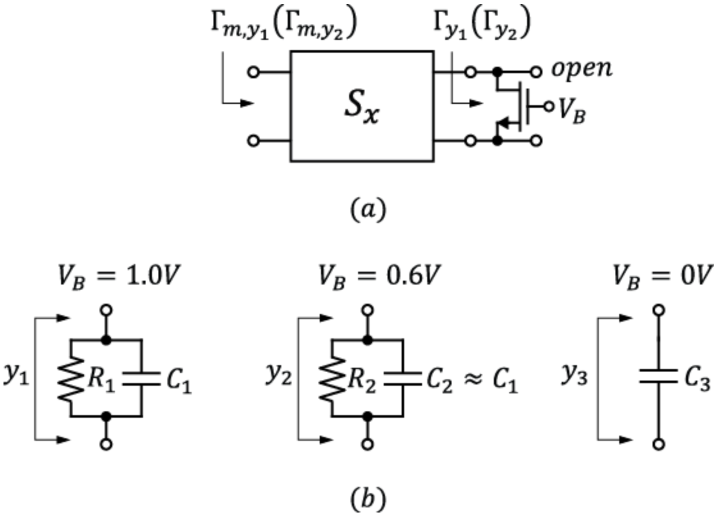

Figure 2.22: (a) Reflection measurements with single transistor termination. (b) Equivalent RC model of terminating transistor at different biasing.

similar to the previously described single-element approach. Though one additional unknown (γ of the t-line) is introduced, this avoids the degeneracy of the measurements. The other approach is to utilize the technique introduced in section 2.2.4 by referencing the high-frequency impedance with that measured at DC. We will take the second route and introduce another optimization technique similar to the load extraction approach in enhanced-LRRM (eLRRM) algorithm [11].

According to Fig. 2.22(a), we have two reflection measurements as M_1 is biased at two different voltages.

$$\Gamma_{m,y_1} = \frac{e_{00} - \Delta_x \Gamma_{y1}}{1 - e_{11}\Gamma_{y1}}, \tag{2.42}$$

$$\Gamma_{m,y_2} = \frac{e_{00} - \Delta_x \Gamma_{y2}}{1 - e_{11}\Gamma_{y2}}, \tag{2.43}$$

Inverting both (2.42) and (2.43) leads to

$$\Gamma_{y1} = \frac{\Gamma_{m,y_1} - e_{00}}{e_{11}\Gamma_{m,y_1} - \Delta_x}, \tag{2.44}$$

$$\Gamma_{y2} = \frac{\Gamma_{m,y_2} - e_{00}}{e_{11}\Gamma_{m,y_2} - \Delta_x}. \tag{2.45}$$

Next, the difference between the normalized load admittance is

$$\Delta y = y_1 - y_2 = \frac{1-\Gamma_{y1}}{1+\Gamma_{y1}} - \frac{1-\Gamma_{y2}}{1+\Gamma_{y2}} = g_1 - g_2 = \Delta g. \tag{2.46}$$

In the above expression, the parasitic capacitances at two impedance states are assumed identical and therefore drop out. This is a valid assumption as NMOS is kept in linear region at all time. (2.46) can be organized as

$$\Delta g + (\Delta g + 2)\Gamma_{y1} + (\Delta g - 2)\Gamma_{y2} + \Delta g \Gamma_{y1}\Gamma_{y2} = 0. \tag{2.47}$$

By inserting (2.44) and (2.45) into (2.47) and note that

$$\Delta g = \frac{R_1 - R_2}{Z_0}, \tag{2.48}$$

with both R_1 and R_2 being the resistance measured at DC, the unknowns (e_{00}, e_{11}, Δ_x) can be solved in conjunction with $\Gamma_{x,short}$ and $\Gamma_{x,open}$. Once S_x is found, S_y can be solved with *thru* measurements according to (2.24).

2.5.3 Load Extraction in Two-element ECal

The accuracy of the previous approach depends greatly on the accuracy of Δg. In order to relax the accuracy requirement in the DC resistance measurements, load extraction technique adopted from eLRRM is applied [11]. Instead of measuring the conductance difference at two different biasing, parasitic capacitance of M1 when biased in linear region is *fitted* such that the conductance as M1 is completely off approaches its minimum. With notation in Fig. 2.22(b), the optimization goal is shown below

$$\min_{b_1} |real(y_3)|. \tag{2.49}$$

This can be done with *optimization* or *curve-fitting* toolbox in Matlab.

2.6 Single-element VNA Calibration

It sounds impossible to solve for the full VNA calibration problem with a single element. Nevertheless, the switch-loaded distributed t-line makes this ultimate calibration possible. The general idea is shown in Fig. 2.23. By distributing switches across the entire t-line, numerous offset-short measurements can be derived using extrapolation technique. If the propagation constant of the switches-loaded t-line (γ') is known, all the

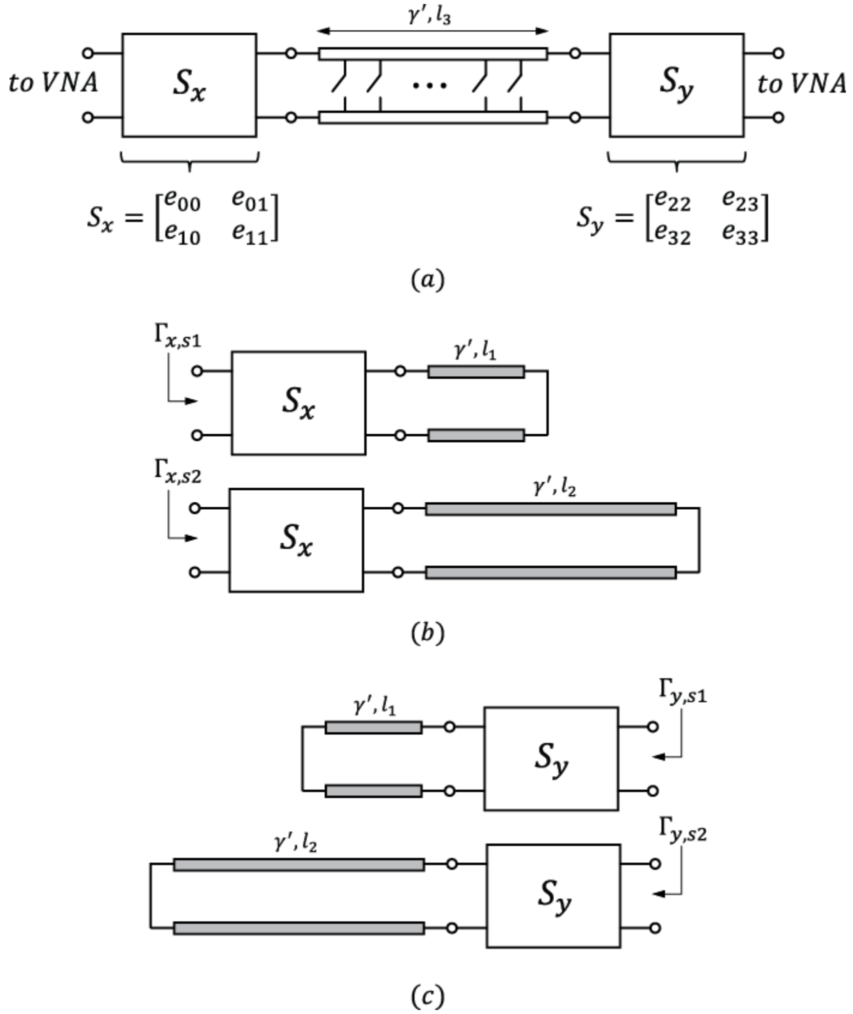

Figure 2.23: (a) Schematic of single-element ECal structure. (b) Offset-short reflection measurements from the left port and (c) from the right port.

error terms can be solved including the transmission ones as the structure by itself is a reciprocal two-port network. The key for this algorithm is to find γ'.

2.6.1 Propagation Constant Extraction in Single-element ECal

Fig. 2.23(b) shows the schematic of two offset-shorts at different t-line lengths. The reflection coefficients can be derived as

$$\Gamma_{x,s1} = T_x T_{l_1} \begin{bmatrix} -1 \\ 1 \end{bmatrix}, \tag{2.50}$$

$$\Gamma_{x,s2} = T_x T_{l_2} \begin{bmatrix} -1 \\ 1 \end{bmatrix}, \tag{2.51}$$

where

$$T_{l_\mathrm{i}} = \begin{bmatrix} e^{-\gamma' l_\mathrm{i}} & 0 \\ 0 & e^{\gamma' l_\mathrm{i}} \end{bmatrix}, \tag{2.52}$$

represents the T-matrix of the t-line with length l_i and propagation constant γ ´. After combining Γ_{s1} and Γ_{s2} into a 2 × 2 matrix form, we arrive at the following expression:

$$[\Gamma_{x,s1} \quad \Gamma_{x,s2}] = \Gamma_{xs} = T_x \begin{bmatrix} -e^{-\gamma' l_1} & -e^{-\gamma' l_2} \\ e^{\gamma' l_1} & e^{\gamma' l_2} \end{bmatrix} = T_x L_1, \tag{2.53}$$

$$T_x = \Gamma_{xs} {L_1}^{-1}, \tag{2.54}$$

The same can be applied on the other port as shown in Fig. 2.23(c):

$$swap(T_y) = \Gamma_{ys} {L_1}^{-1}. \tag{2.55}$$

In (2.55), *swap* operation means the ports of the network are flipped and is expressed mathematically as

$$swap(T_y) = \begin{bmatrix} 0 & 1 \\ 1 & 0 \end{bmatrix} {T_y}^{-1} \begin{bmatrix} 0 & 1 \\ 1 & 0 \end{bmatrix} = I_r {T_y}^{-1} I_r. \tag{2.56}$$

With (2.56), (2.55) can be reorganized as

$$T_y = I_r L_1 {\Gamma_{ys}}^{-1} I_r. \tag{2.57}$$

Inserting (2.54) and (2.57) into the line measurements

$$M_{line} = T_x \begin{bmatrix} e^{-\gamma' l_3} & 0 \\ 0 & e^{\gamma' l_3} \end{bmatrix} T_y, \tag{2.58}$$

leads to the following expression:

$${\Gamma_{xs}}^{-1} M_{line} {I_r}^{-1} \Gamma_{ys} = M = {L_1}^{-1} \begin{bmatrix} e^{-\gamma' l_3} & 0 \\ 0 & e^{\gamma' l_3} \end{bmatrix} L_1. \tag{2.59}$$

Expanding the left side of (2.59), we arrive at the following four equations:

$$m_{11} = \frac{e^{-\gamma'(l_3 - l_1 - l_2)} - e^{\gamma'(l_3 - l_1 - l_2)}}{det(L_1)}, \tag{2.60}$$

$$m_{12} = \frac{e^{-\gamma'(l_3 - 2l_2)} - e^{\gamma'(l_3 - 2l_2)}}{det(L_1)}, \tag{2.61}$$

$$m_{21} = \frac{-e^{-\gamma'(l_3-2l_1)} + e^{\gamma'(l_3-2l_1)}}{det(L_1)}, \tag{2.62}$$

$$m_{22} = -m_{11}, \tag{2.63}$$

$$det(L_1) = -e^{-\gamma'(l_1-l_2)} + e^{\gamma'(l_1-l_2)}. \tag{2.64}$$

Here m_{11}, m_{12}, m_{21}, and m_{22} are the elements in the combined measurement M and $det(L_1)$ is the determinant of the matrix L_1. As all the lengths are defined by the layout, we can solve for the switched-loaded propagation constant from either one of (2.60) – (2.62). Once γ ´ is found, the error terms are solved using the offset-short measurements. The impedance can be renormalized following the procedure in section 2.2.4.

2.6.2 Single-element ECal Implementation

Fig. 2.24 shows the schematic of three switched-load t-line structures. Note that Fig. 2.24(b) and Fig. 2.24(c) differ only in the granularity of the switches when distributed along the unloaded t-line. Switch mismatch has negligible impact on the accuracy due to the averaging effect of the distributed nature. The cut-off frequency for the loaded line is approximately 1 THz assuming each segment has an effective inductance and capacitance of 10 pH and 10 fF. The characteristic impedance of the line is 30 Ω. Fig. 2.24(d) shows a 3D layout view of the connection between t-line and a switch, which is placed underneath the ground mesh.

2.7 Chapter Summary

This chapter introduced a novel VNA calibration technique in CMOS. By modulating the impedance of switches electronically, error terms can be solved with fewer calibration structures. The core theme is to derive reflection measurements loaded with *ideal short* using the concept of *load extrapolation*. In addition, the proposed π-network configuration allows the application of *impedance sharing* to avoid the introduction of additional unknown variables. *Impedance renormalization* can be carried out in the same structure by approximating the complex impedance of a transistor at high frequencies with resistance measured at DC. The reference plane can be placed on lower metal layers by layout design. This allows the exclusion of access via from the DUT. The complete die photo of the ECal chip is shown in Fig. 2.25.

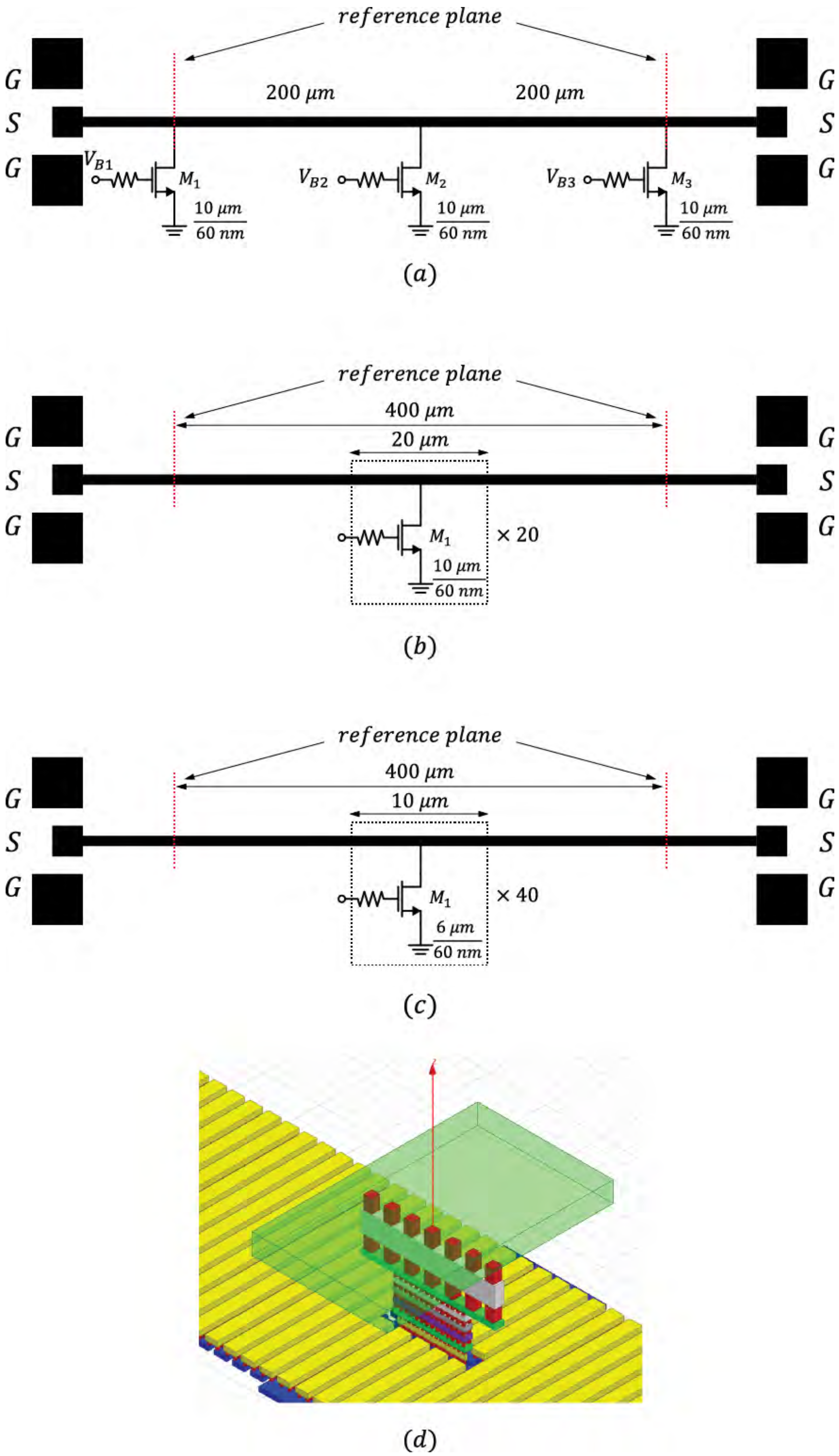

Figure 2.24: (a) – (c) Circuit schematics of different single-element ECal structures. (d) 3D illustration of the connection from the signal line to a switch.

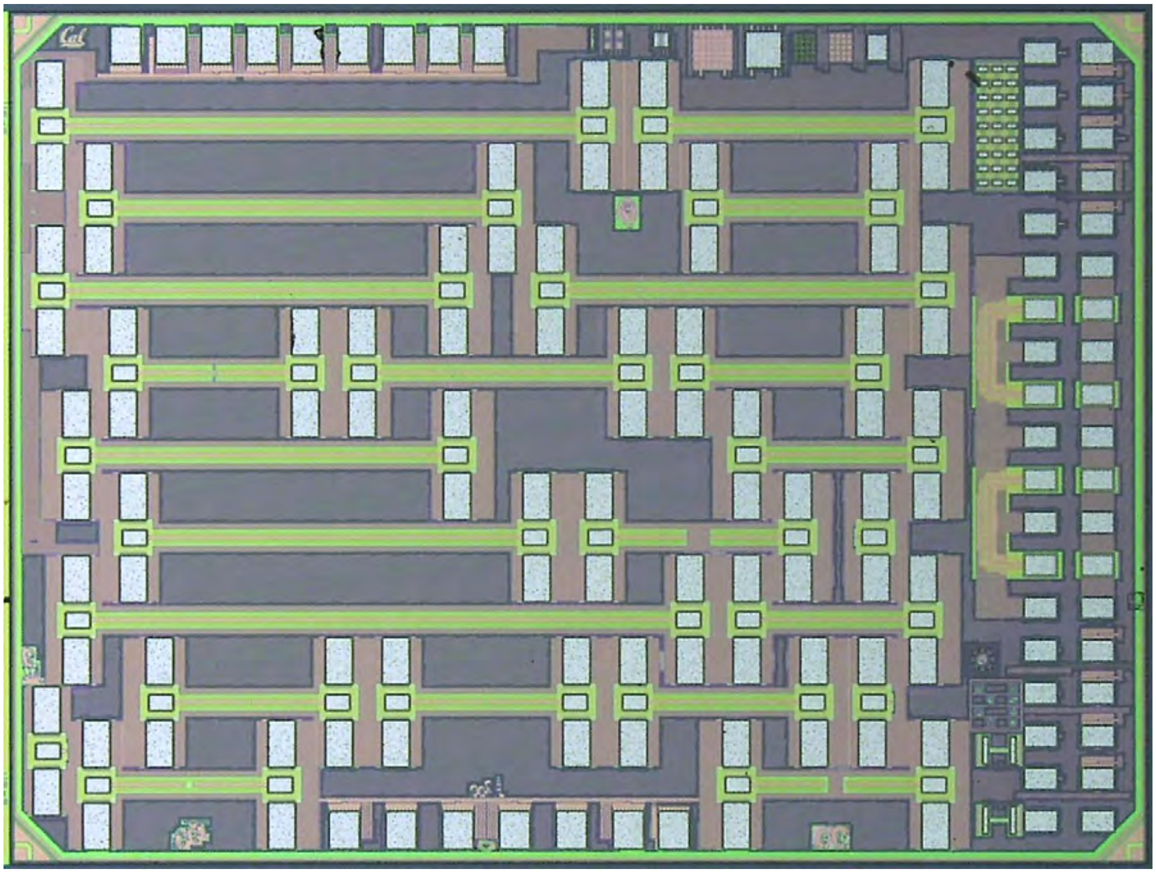

Figure 2.25: ECal chip micrograph.

Chapter 3

Broadband Dielectric Spectroscopy for Chemical Mixture Detection

The study of the interaction between matter and electromagnetic fields can be dated back to 19th century when James Clerk Maxwell uncovered the coupling between the electric and the magnetic fields. Thereafter the characterization of electromagnetic responses has become one of the most important analytical tools for material science and electronic engineering. The polarization of matter due to impinged fields is quantified by the permittivity (ε) and the permeability (μ), which describes how electromagnetic waves propagate in the medium. As the polarization depends uniquely on the molecular structures and the composition of the matter, it is possible to exploit the electromagnetic property in emerging biomedical applications.

Currently the most successful electromagnetic sensing application is the millimeter-wave imaging used in airport security screening [15]. Similar technology has also been pursued by numerous researchers in the medical fields for non-invasive tumor detection in human body [16 – 17]. Now it is time to turn our attention to even smaller specimen: cells that constitute the human body and biological molecules such as proteins and DNA. In this chapter, we will first review the fundamental principle of dielectric spectroscopy and different measurement modalities. Following that, we will discuss the design and the implementation of a 1 – 50 GHz sensor prototype in CMOS for chemical mixture detection.

3.1 Introduction to Broadband Dielectric Spectroscopy (BDS)

The interaction of matter with the electromagnetic fields induces different polarization effects depending on the composition, structure, and the orientation. Such a response is frequency-dependent and therefore enables the use of spectroscopy for material characterization. The polarization ($\vec{P}$) leads to the change of field intensity ($\vec{E}$) in

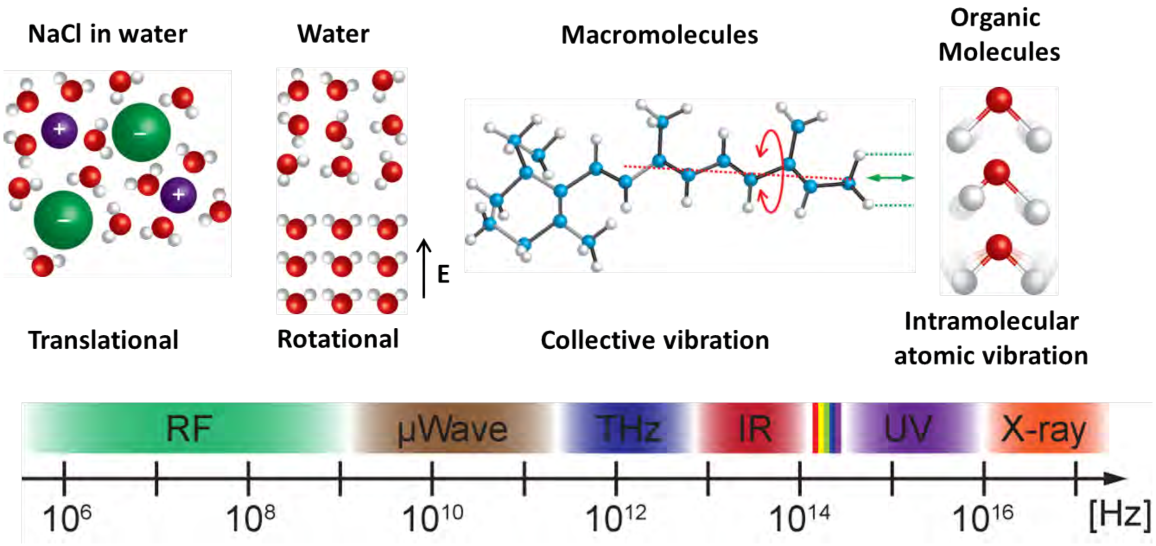

Figure 3.1: The interaction of molecules with electromagnetic fields.

the medium and is related to the displacement fields ($\vec{D}$) as

$$\vec{D} = \varepsilon_0 \vec{E} + \vec{P}. \tag{3.1}$$

Formally, the polarization is defined as the volumetric density of dipole moment in space:

$$\vec{P} = \frac{\sum \vec{p}}{V}. \tag{3.2}$$

On the other hand, it is easier to regard the polarization as the susceptibility (χ_e) of matter:

$$\vec{P} = \varepsilon_0 \chi_e \vec{E}. \tag{3.3}$$

Equation (3.1) can therefore be expressed as

$$\vec{D} = \varepsilon_0 (1 + \chi_e) \vec{E} = \varepsilon_r \varepsilon_0 \vec{E} = \varepsilon \vec{E}, \tag{3.4}$$

with ε being the complex permittivity:

$$\varepsilon = \varepsilon' - j\varepsilon". \tag{3.5}$$

In (3.5), the real part accounts for the amount of electric energy stored in the matter, and is often termed dielectric constant, whereas the imaginary part captures the loss dissipated as heat, and is often characterized as loss tangent:

$$\tan\delta = \frac{\varepsilon''}{\varepsilon'}. \tag{3.6}$$

For example, the dielectric constant and the loss tangent of an undoped silicon at RF is approximately 11.7 and 0.043, respectively. In the optics, index of refraction (n) is more often used and the link with the permittivity and the permeability is

$$n = \sqrt{\varepsilon_r \mu_r}. \tag{3.7}$$

It is more appropriate to model the polarization with time-dependency by convolving the material dependent susceptibility with the field intensity:

$$\vec{P}(t) = \varepsilon_0 \int_{-\infty}^{\infty} \chi_e(t-\tau)\vec{E}(\tau)d\tau, \tag{3.8}$$

The above expression is similar to our engineering description of a linear time-invariant (LTI) system, which can be associated with a specific frequency response describing the system dynamics. In biological samples, such dynamics depends on the motion of the molecules. Fig. 3.1 illustrates a few examples with molecules widely found in blood. We will briefly explain each motion in the following paragraphs.

At low frequencies around kHz, the ions exhibit translational motions when applying time-varying electric fields. Such ionic diffusion leads to the accumulation of charges at the electrode-electrolyte interface and is the major cause of the electrical-double-layer (EDL) [18]. The phenomenon is similarly found in the electrolytic capacitors, resulting in extremely high effective permittivity (> 1000) for the medium with high ionic strength [19]. As frequency increases, the translational motion is prohibited, causing the permittivity to drop. This is termed α-dispersion.

There are two different molecular motions at frequencies above MHz. First, large molecules such as protein will exhibit rotational behavior if charge is non-uniformly distributed along the molecular chain. On the other hand, the interfacial polarization of the cellular membrane due to Maxwell-Wagner effect also contributes the dispersion of the permittivity. Such a combinational effect is termed β-dispersion [19]. It is worth mentioning that the Maxwell-Wagner polarization is widely studied with Effective Medium Theory (EMT) to analyze the effective permittivity of a cell using single or double shell models [20].

At microwave frequencies, the highly polar water molecules will re-orient themselves with the fields through the rotational motions, leading to γ-dispersion centered around the relaxation frequency at 18 GHz [19]. On the other hand, as biological specimen is heterogeneous in nature, the interaction between the nearby molecules due to Van del Waal forces leads to δ-dispersion, which manifests themselves at frequencies slightly below the γ-dispersion. The origin of δ-dispersion can be attributed to the presence of bound water formed around the macromolecules as a thin membrane layer. These water molecules will present less mobility when responding to the alternating fields. The aforementioned polarizations are based on relaxation. From circuit perspectives, these relaxation effects are equivalent as cascading of several RC filters.

As frequency increases above THz and infrared band, resonance responses due to the collective vibration of macromolecules and the vibration of hydrogen bonds can be observed. A distributed mass-spring system can often be applied to describe such behavior [21]. The atomic polarization due to the distortion of the electron clouds within an atom can be observed at optical frequencies.

The dispersion of the permittivity is usually described using the Debye model:

$$\varepsilon(\omega) = \varepsilon_\infty + \frac{\varepsilon_s - \varepsilon_\infty}{1 + j\omega\tau} - j\frac{\sigma}{\omega}, \tag{3.9}$$

where ε_s and ε_∞ are the static and optical permittivity, respectively, $j = \sqrt{-1}$, τ is the relaxation time constant, and σ is the conductivity. Complex composition of the biological specimen can be accounted for with the superposition of Debye equations:

$$\varepsilon(\omega) = \varepsilon_\infty + \sum_i \frac{\Delta\varepsilon_i}{1 + j\omega\tau_i}. \tag{3.10}$$

In (3.10), $\Delta\varepsilon_i$ and τ_i describe the difference between the static and the optical permittivity and the associated time constant at each band, respectively. Note that the effect of conductivity has been ignored in (3.10) as ionic distribution is less pronounced at microwave frequencies [22]. Other equations with empirical parameters can be used to simplify the model. The Havriliak-Negami relaxation model is the most generalized one:

$$\varepsilon(\omega) = \varepsilon_\infty + \frac{\varepsilon_s - \varepsilon_\infty}{(1 + (j\omega\tau)^\alpha)^\beta}. \tag{3.11}$$

In the above expression, α and β are the empirical parameters describing the broadening and the asymmetry of the complex permittivity when plotted in polar form. Equation (3.11) is called Cole-Davison model if $\alpha = 1$ and Cole-Cole model if $\beta = 1$.

The impulse response of the electric susceptibility can also be modeled with a stretched exponential function. Such a function can be conceived as a distribution of relaxation time constant with the distribution function $\rho(u)$:

$$\chi_e(t) = \chi_e(0)e^{-t^\beta} = \int_0^\infty \rho(u)e^{-\frac{t}{u}}du. \tag{3.12}$$

The Fourier Transform of (3.12) is called Kohlrausch–Williams–Watts function and can only be found with numerical integration.

The polarization of matter is considered as a causal LTI system. Therefore Kramer-Kronig relationship is applicable to the complex permittivity, linking the real and the imaginary parts of the permittivity through Hilbert transform [23]. In the time-domain,

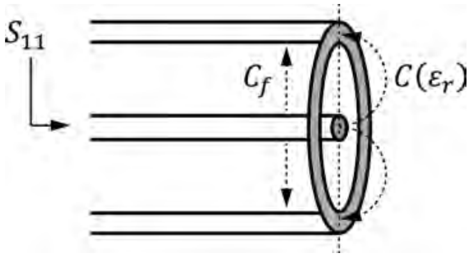

Figure 3.2: Open-ended coaxial sensor.

Hilbert transform is the convolution of the function of interest with *1/***π***t*. In frequency-domain, Hilbert transform operates by multiplying the spectrum with *–j*×*sign*(*ω*), where

$$sign(\omega) = \begin{cases} -1, & for\ \omega < 0 \\ 0, & for\ \omega = 0 \\ 1, & for\ \omega > 0 \end{cases} \tag{3.13}$$

Due to system causality, it is sufficient to measure either the real or the imaginary part of the complex permittivity. The measurements of both parameters can facilitate the cross checking of the results.

3.2 Sensor Types

Sensors of different types are used to characterize the permittivity of the biological samples based on its size and physiological states. This section provides a summary of the existing sensor topologies.

3.2.1 Open-ended Coaxial Cables

The open end of a coaxial cable is one popular sensing site for tissue measurements at microwave frequencies. As fringing fields interact with the material-under-test (MUT), changes in the effective load result in differences in the measured S_{11} (Fig. 3.2).

$$S_{11} = \frac{1 - j\omega Z_0\left[C(\varepsilon_r) + C_f\right]}{1 + j\omega Z_0\left[C(\varepsilon_r) + C_f\right]}. \tag{3.14}$$

With careful calibration and shifting of the reference plane, the open-ended coaxial cables can be used as a *probe* to quantify the complex permittivity of tissues in a convenient way. For example, [24, 25, 26] presents a coaxial probe machined with stainless steel for interfacing with wet tissue excised from the tumor surgeries. With the advancement of micromachining, coaxial probes with aperture diameter less than 1 mm is feasible. For example, [27] demonstrated an active probe operating from 2 – 16 GHz, consisting of both a MEMS-based coaxial probe with 0.6-mm aperture size and CMOS circuits. The frequency range is limited by the electronics; the probe itself can support operating frequencies up to 30 GHz [28].

3.2.2 Planar Waveguides

Recently, transmission-line sensors have drawn significant attention in the community due to its broadband nature. With both transmission and reflection measurements, complex permittivity can be inferred by quantifying the change of wave propagation as the channel is loaded with MUT. In particular, planar structures such as microstrip lines and coplanar waveguide (CPW) are of great interest due to ease of microfluidic integration. This facilitates the sample delivery at reduced volume [29]. In particular, cell measurements at microwave frequencies are all accomplished with planar waveguides. For example, [30] and [31] measure cells in suspension placed within a miniature reservoir fabricated on top of the CPW. Single-cell analysis is similarly performed by immobilizing the cells using C-cup trapping structure [22].

3.2.3 Resonators

Sensors employing resonance offer superior sensitivity enhancement due to bandwidth narrowing. By measuring the shift in the resonant frequency and the degradation of the resonator’s quality factor, complex permittivity can be readily extracted. Similar to the waveguides, planar resonators such as spiral inductors, microstrop rings, and LC resonators are preferred. For example, [32] performs glucose sensing using planar spiral inductors fabricated on a PCB. The same can be applied for cell measurements once the cells are immobilized on top of the sensing capacitor. Planar antennae can serve for the same purpose. One good example is the measurement of protein conformation change using slot antenna [33].

It is worth mentioning the Margin Probe developed by Dune Medical Inc., a biomedical start-up from Israel [34]. The pencil-like probe integrates a spiral coil with 1-cm aperture resonating at 500 MHz when interacting with the tissue. The probe is used to identify the margin of excised tumors directly in the operating room. This provides real-time feedback to the doctors and the surgeons. Such a device has received FDA approval in 2013 and the clinical trials conducted in UC Irvine Medical Center reports that it is capable of reducing the rate of secondary surgery by 50 % [35].

3.2.4 Free-Space Measurements

Free-space measurements are yet another type of dielectric sensing which can be performed remotely. Similar to the measurements using waveguide sensors, this approach measures the changes of the amplitude and the phase as the target sample is inserted within the propagation paths. One critical issue for such measurement modality is the necessity of high power source to compensate for the path loss. This is not the case for near-field sensing where the samples are placed in direct contact with the sensors.

3.3 Instrumentation

3.3.1 Frequency-domain Spectroscopy

All the aforementioned discrete sensors are measured with vector network analyzer (VNA). This instrumentation embeds various directional couplers to separate the incident and the reflected waves at each port for complex ratiometric measurements over a broad range through frequency sweeping. However, the sensor performance is considerably suffered due to the existence of the front-end passives. For instance, the receiver noise figure in Agilent N5242 PNA can be as high as 31 dB (noise floor of -133 dBm at 10-Hz bandwidth). This motivates the development of new sensor electronics.

3.3.2 Time-domain Spectroscopy

Broadband permittivity can also be measured in the time-domain using reflectometry and pulsed system, which offers significant throughput enhancement as frequency sweeping is avoided. Such time-domain spectroscopy has been widely adopted for THz spectroscopy by generating femto second pulses with quasi-optic techniques [36]. Pseudo-random sequence signal is yet another type of input excitation source for rapid broadband measurements [37]. As the input signal spans over a broad frequency spectrum, the correlation between the input and the sampled outputs allows the characterization of frequency response of the sensor. The main challenge for time-domain measurement is the design of high-speed sampler with low noise and low distortion.

3.3.3 Impedance Analyzer

The impedance analyzer is suitable for instrumentation miniaturization due to its architectural simplicity. As shown in Fig. 3.3(a), the current flows through the sensor is first amplified, converted to a voltage with a transimpedance amplifier (TIA), and I/Q demodulated directly without the need for directional couplers. The *absolute* sensor impedance can be calculated if the driving amplitude (V_0) is known a priori:

$$Z_{sense} = \frac{V_0}{I_{sense}}. \tag{3.15}$$

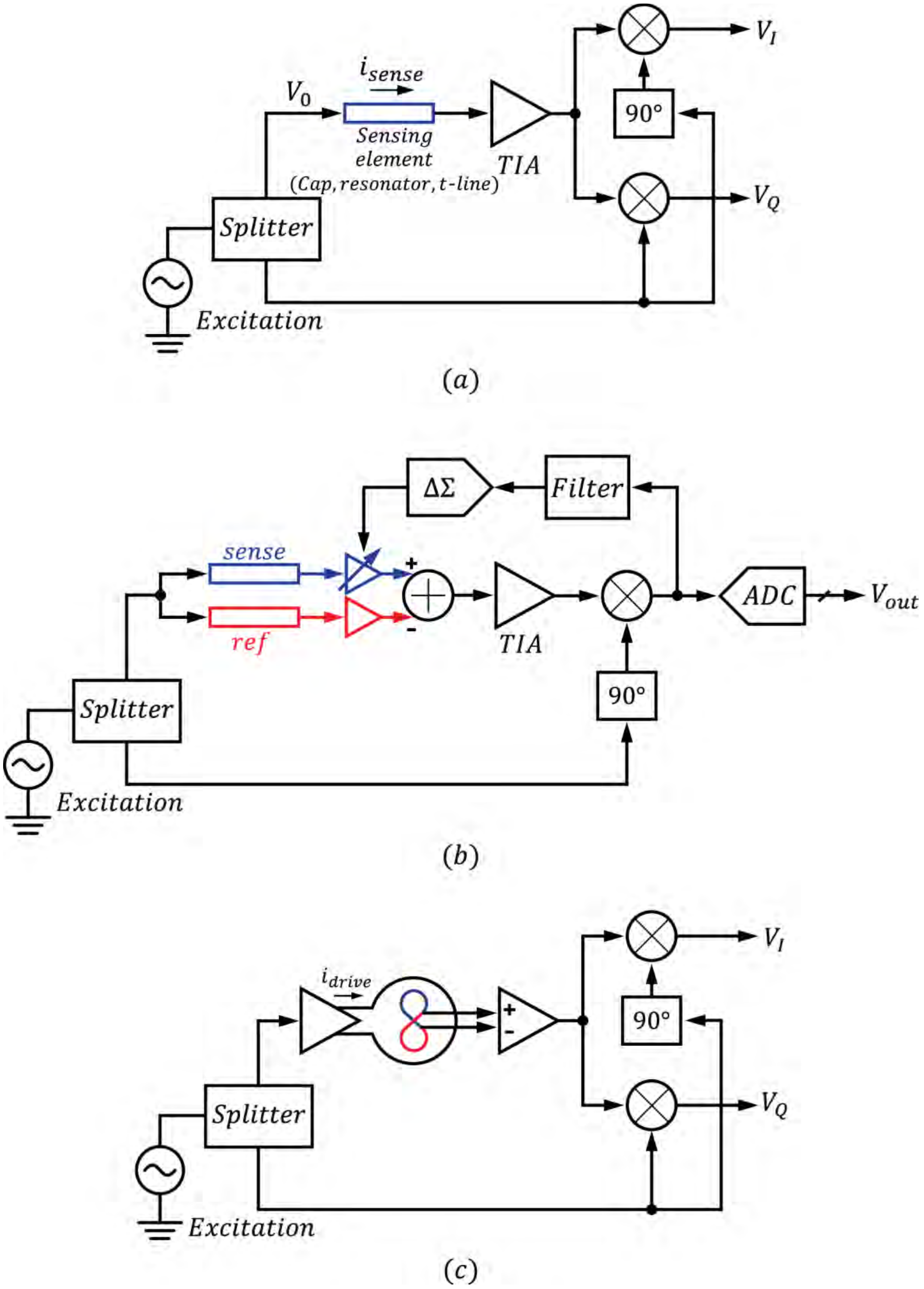

Figure 3.3: Impedance analyzer architectures.

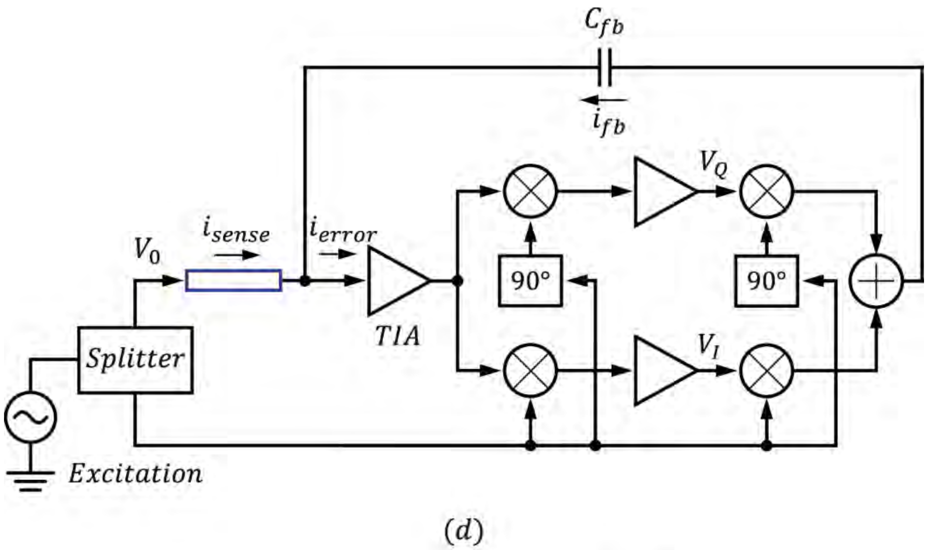

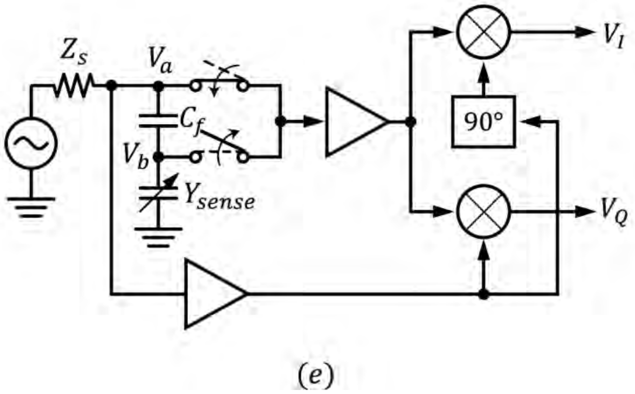

Figure 3.3(cont'): Impedance analyzer architectures.

On the other hand, the *sensing* signal, which is defined as the percentage change in the sample impedance, is proportional to the driving amplitude:

$$\Delta i = \frac{\Delta Z}{Z_{sense}} I_0 = \frac{\Delta Z}{Z_{sense}} \left(\frac{V_0}{Z_{sense}}\right). \tag{3.16}$$

Consequently, sensor *SNR* can be significantly improved with higher driving voltage. However, it is important to be aware that the driving amplitude cannot be arbitrary large; in fact, it is either determined by the affordable signal swing and the acceptable distortion level at the transmitter or the dynamic range specification at the receiver. For example, 10-dB back-off from the 1-dB compression point of the receiver is mandatory to avoid measurement error due to distortion.

Due to its architectural simplicity, several CMOS impedance analyzers have been implemented for bio-sensing applications. In [38], a CMOS impedance analyzer with 10 × 10 sensing sites is demonstrated for label-free bio-molecular sensing. With 3.3-V supply, the work demonstrates a dynamic range of more than 90 dB in 10-Hz bandwidth. To further improve the performance, [39] implements a sensor front-end with baseline cancellation. By driving the two sensors with a common excitation, the relative difference between the reference and the sensing channels can be distilled without saturating the subsequent amplifiers (Fig. 3.3(b)). Optimum cancellation is achieved with auto-calibration prior to the actual measurements using delta-sigma modulator. Note that such baseline signal can also be cancelled with passive devices. For instance, [40] embeds a *figure-8* pick-up transformer within an excitation coil for the detection of magnetic beads (Fig. 3.3(c)). Feedback is another popular technique to relax the dynamic range requirement for the readout circuits. Fig. 3.3(d) shows the conceptual view of the architecture presented in [41]. The signal of interest is first I/Q demodulated to DC, amplified with high-gain integrators, and modulated back to RF to drive a feedback capacitor. With such global feedback, the outputs (V_R and V_I) will self-adjust such that the error signal i_{error} can be minimized. The impedance of the sensor (Z_{sense}) is therefore related to the output voltages V_R and V_I at DC with the following expression:

$$s\omega C_{FB}(V_R \cos\omega_0 t + V_I \sin\omega_0 t) = -\frac{V_0 \cos\omega_0 t}{Z_{sense}}. \tag{3.17}$$

The system can perform impedance measurements up to 150 MHz, achieving 0.6-aF$_{rms}$ noise floor in 10-Hz bandwidth at 1-V amplitude drive.

The aforementioned impedance analyzers are limited to frequencies less than 1 GHz. For microwave sensing, [42] implements an impedance analyzer with a capacitive half-bridge. Ratiometric measurement is carried out from 0.62 – 10 GHz by measuring both the complex voltages at V_a and V_b sequentially (Fig. 3.3(e)). Such an approach mitigates the load-pull effect on the signal source.

3.4 Broadband Dielectric Sensor in CMOS

To circumvent the aforementioned frequency limitation, a broadband dielectric sensor integrating an on-chip waveguide sensor and receiver front-end is discussed in this section. Measurement technique for drift mitigation and baseline cancellation is proposed. Experiment results on different chemicals are presented.

3.4.1 Sensor and Reference Liquid Calibration

Fig. 3.4 shows the device photo. The CMOS IC with on-chip sensor is clamped between a microfluidic module to perform sensing directly on top of the chip. In this work, a coplanar waveguide (CPW) transmission line (t-line) is used as the sensing element due to its broadband nature. Fringing fields, originating from the center signal

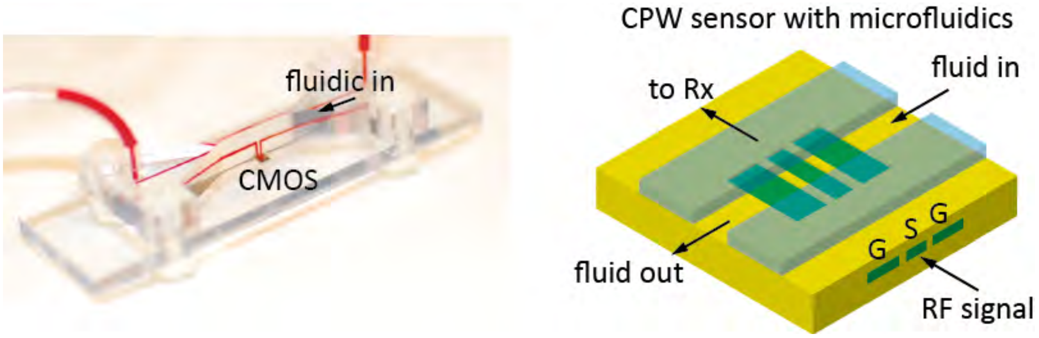

Figure 3.4: Photograph of dielectric spectroscopy biosensor.

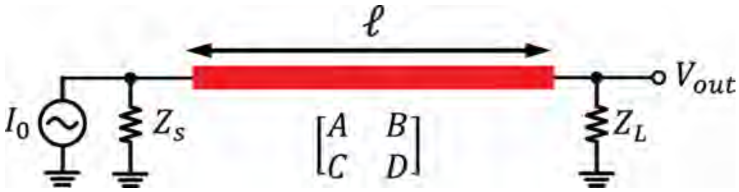

Figure 3.5: Sample-loaded t-line model for reference liquid calibration.

line and terminating in the adjacent ground, pass through the biological sample, enabling dielectric detection. To maximize sensor sensitivity, the passivation layer on top of the sensing metal is removed using pad-open layer. Unlike conventional S-parameter measurements using VNAs which requires bulky directional couplers, transmission measurement in voltage is adopted due to its simplicity in system architecture. To relate measured output voltage with sample permittivity ($\varepsilon = \varepsilon' - j\varepsilon''$), a novel model is proposed. Fig. 3.5 shows the model of a sample-loaded t-line. The reciprocal of V_{out} can be expressed as a linear function of t-line ABCD matrix:

$$\frac{1}{V_{out}} = \frac{1}{I_0}\frac{Z_L}{Z_S Z_L}A + \frac{1}{I_0 Z_S Z_L}B + \frac{1}{I_0}C + \frac{1}{I_0}\frac{Z_S}{Z_S Z_L}D. \tag{3.18}$$

$$\begin{bmatrix} A & B \\ C & D \end{bmatrix} = \begin{bmatrix} cosh(\gamma\ell) & Z_0 sinh(\gamma\ell) \\ {Z_0}^{-1} sinh(\gamma\ell) & cosh(\gamma\ell) \end{bmatrix}. \tag{3.19}$$

Note that $Z_0\gamma = R + j\omega L$ and $\gamma/Z_0 = G + j\omega C$ where R, L, G, and C are circuit parameters of a t-line in quasi-TEM mode with units of ohm/m, H/m, S/m, and F/m. Since the t-line metal is exposed to the sample directly without passivation in between, the following equation holds:

$$G + j\omega C = F(\omega) \cdot (\varepsilon' - j\varepsilon''). \tag{3.20}$$

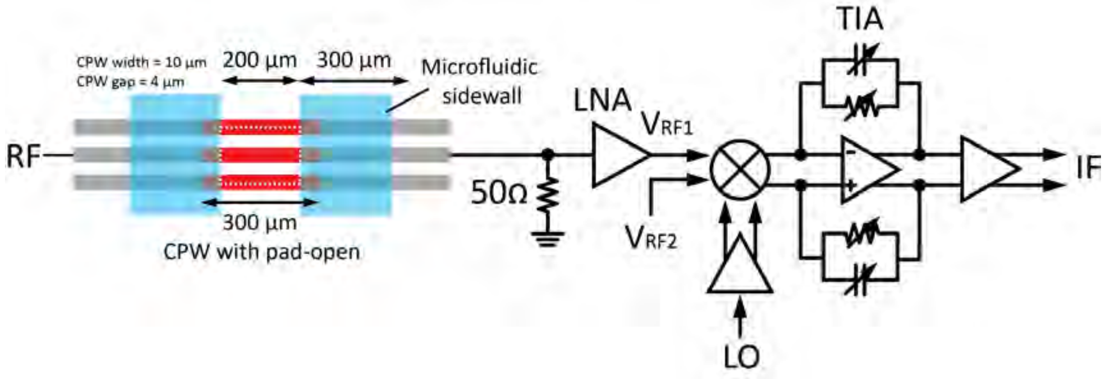

Figure 3.6: System architecture of the proposed sensor.

Here $F(\omega)$ is a geometric dependent parameter and is constant for a given CPW dimension. By applying Taylor series expansion on *sinh* and *cosh* functions up to 4th term, (3.18) can be re-expressed as a polynomial function of sample permittivity:

$$\sinh x = x + \frac{x^3}{3!} + \frac{x^5}{5!} + \cdots \tag{3.21}$$

$$\cosh x = 1 + \frac{x^2}{2!} + \frac{x^4}{4!} + \cdots \tag{3.22}$$

$$V_{out}{}^{-1} = a \cdot \varepsilon^3 + b \cdot \varepsilon^2 + c \cdot \varepsilon + d. \tag{3.23}$$

In (3.23), the unknown coefficients *a*, *b*, *c*, and *d* can be calibrated by measuring four reference liquids with the least-square method. More importantly, the interconnect as well as the signal conditioning circuitry before and after the sensor, which exist in practical system implementation, can all be absorbed into the coefficients. Consequently, as compared to conventional approach using VNA where the sensor boundary must be precisely known [29], the proposed model is more robust to misalignment of microfluidics.

3.4.2 Receiver

A heterodyne architecture is utilized in the broadband receiver (Fig. 3.6). The sensing signal is first amplified by a distributed amplifier (DA) with 50-Ω input impedance, down-converted to 100-MHz IF frequency, and demodulated off-chip for vector measurements. The DA (Fig. 3.7(a)) consists of five unit cells. The input and output transmission lines are implemented with center-tapped inductors (Fig. 3.7(b)) for area reduction [43]. Series peaking inductors are inserted at the cascode nodes to further enhance the bandwidth. Note that DA exhibits excellent noise figure in the pass-band

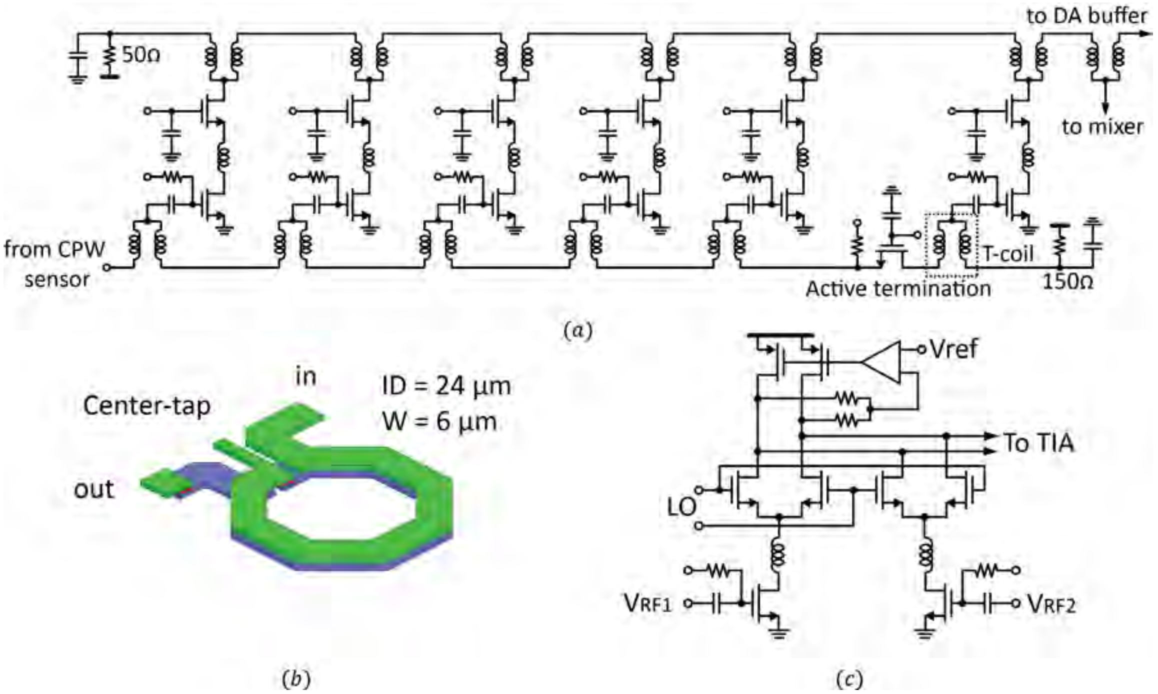

Figure 3.7: (a) Distributed amplifier. (b) Vertically-coupled center-tapped inductor. (c) Double-balanced mixer.

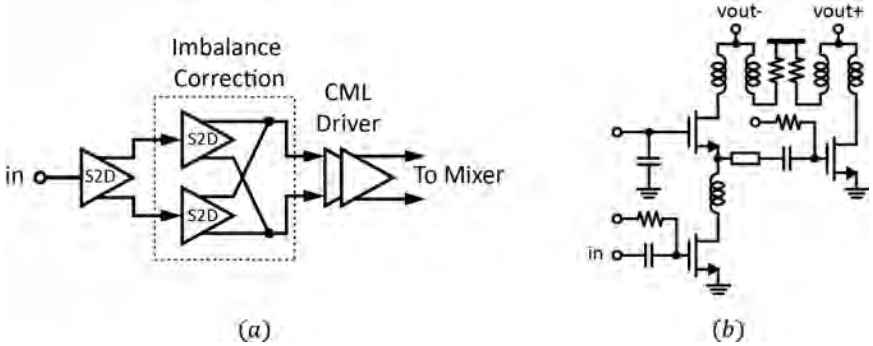

Figure 3.8: (a) LO chain block diagram. (b) CS-CG S2D cell.

except at frequency below ¼ of the line cut-off (~ 18 GHz) due to increased noise contribution from the gate termination. On the other hand, as dipole relaxation for biological substance also occurs around this frequency band, it is desirable to improve the sensitivity through circuit techniques. In this work, a noise-cancellation (NC) DA is proposed. Instead of 50-Ω polysilicon resistor, the gate-line is terminated with a common-gate (CG) amplifier followed by a cascode stage. Signal is summed constructively at the output while the noise from the active termination is cancelled due to sign inversion [44]. The CG amplifier employs T-coil peaking for bandwidth enhancement. A second 2-stage DA is cascaded for testing purpose.

The mixer (Fig. 3.7(c)) employs a double-balanced structure to prevent LO

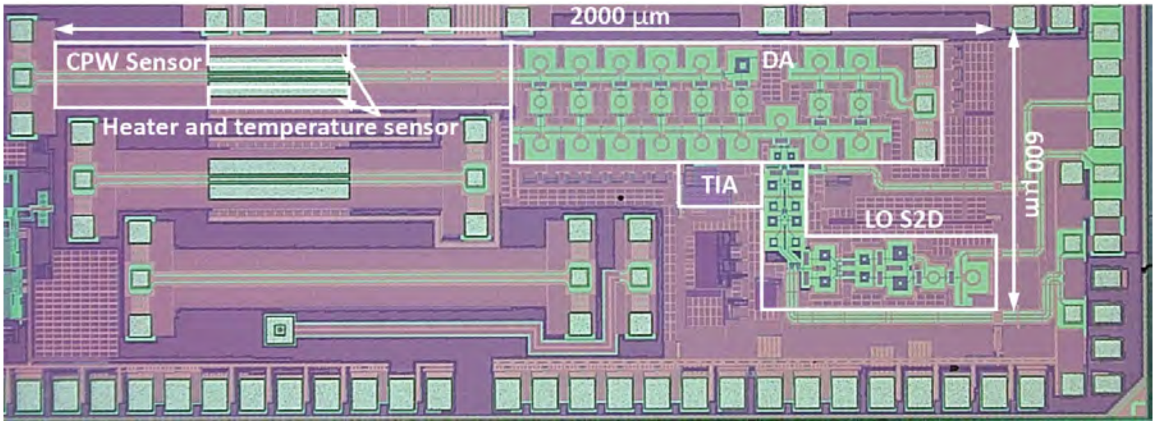

Figure 3.9: Photograph of CMOS sensor.

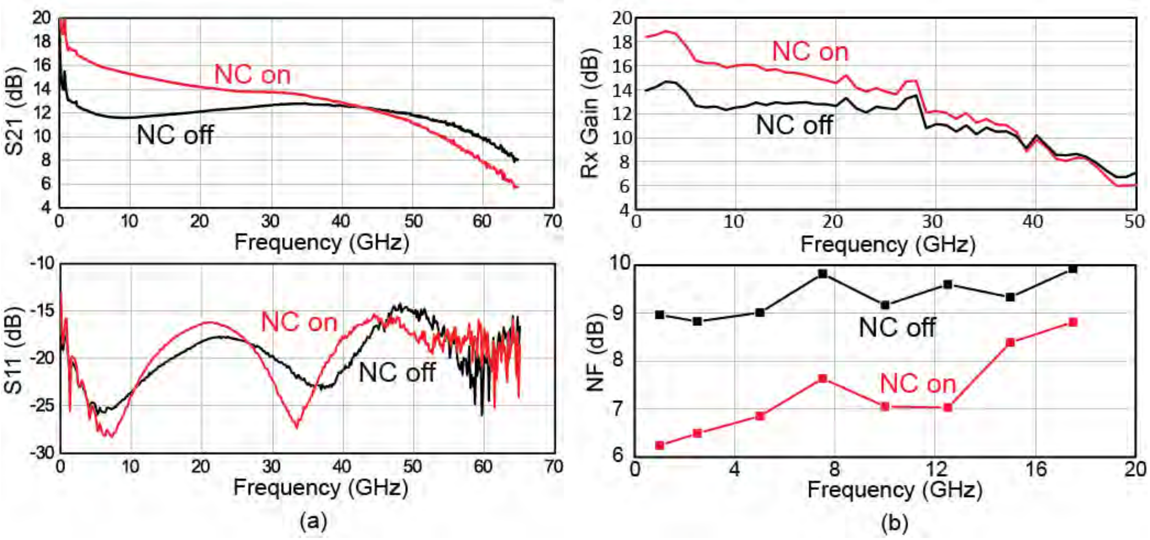

Figure 3.10: Measurement results of (a) 2-stage DA (b) receiver.

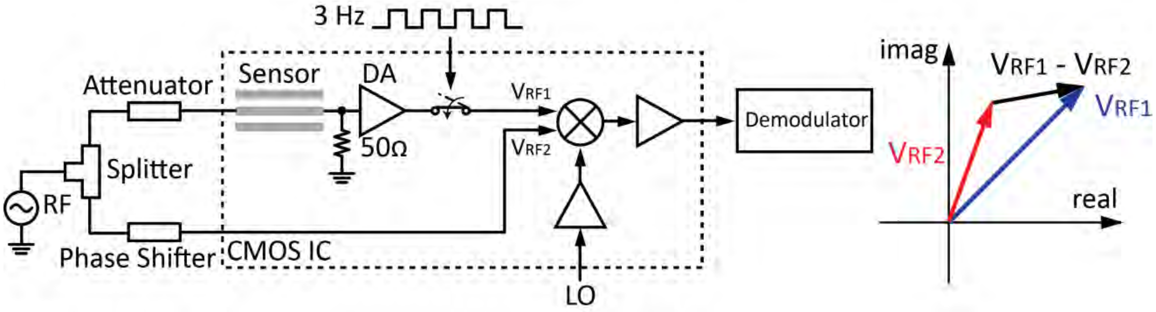

Figure 3.11: Measurement setup employing correlated-double-sampling.

feedthrough. V_{RF1} is driven by the DA while V_{RF2} can either be AC grounded or driven by another signal at RF frequency. The purpose of the latter approach will be discussed in the next section. To maximize both the bandwidth and the linearity, the mixer is inductively-peaked and loaded by pseudo-differential inverter-based TIA. In this prototype, the LO signal is fed off-chip. The LO chain (Fig. 3.8(a)) consists of a single-to-differential (S2D) stage followed by two CML buffers. The S2D stage consists of three CS-CG cells with the outputs of the last two connected in cross-coupled fashion. In this way, the phase error due to path mismatch is averaged out. Fig. 3.8(b) shows the schematics of the CS-CG S2D cell.

3.4.3 Experimental Results

Fig. 3.9 shows the die photo of the sensor in 65-nm CMOS. First, the electrical performance of the front-end is measured through on-wafer probing. The 2-stage DA measures a pass-band gain of 12 dB and a NF of 6dB at low frequency with 60-GHz -3-dB bandwidth (Fig. 3.10(a)). As the noise cancellation is activated, the low frequency gain is boosted by 4 dB while the NF is reduced by 2 dB. Without NC, the DA achieves an average input P_{-1dB} of -8 dBm. A 3.5 dB reduction is observed as NC is enabled at frequency below 10 GHz. Fig. 3.10(b) shows the electrical performance of the front-end. The combined DA-mixer-TIA provides a gain of 18 dB and 7 dB NF at 1 GHz (NC on) while providing gain up to 50 GHz. The gradual gain roll-off is due to insufficient LO drive at high frequencies. The measured average NF from 1 to 18 GHz is 7.5 dB. The input-referred P_{-1dB} is -31 dBm and -26.8 dBm at 1 and 20 GHz, respectively. Consequently, the linearity is limited by the baseband stages.

Fig. 3.11 shows the measurement setup based on correlated double sampling (CDS) with the capability of rejecting phase wander between RF/LO for the on-chip Rx and the reference clock for the external demodulator. The idea is to monitor the system drift through another RF signal that is insensitive to the presence of the sample. This is achieved by injecting a phase-coherent signal at V_{RF2} of the mixer and switching the DA on and off. Measurements of $-V_{RF2}$ and $V_{RF1} - V_{RF2}$ (Fig. 3.11) are collected sequentially. The desired voltage (V_{RF1}) can be re-constructed by normalizing to its adjacent measurement:

$$\frac{V_{RF1}}{V_{RF2}} = -\left(\frac{V_{RF1} - V_{RF2}}{-V_{RF2}} - 1\right). \tag{3.24}$$

Another benefit of injecting at V_{RF2} is to cancel out the baseline signal exciting the CPW sensor at IF. This allows maximizing the SNR without saturating the mixer, which is beneficial for low frequency operation as the phase shift across the CPW t-line is smaller. In order to achieve optimum baseline signal cancellation, an off-chip 20-GHz phase shifter (PDL-100A, Colby Instrument) with electronic control is used to null the output prior to the sample measurements.

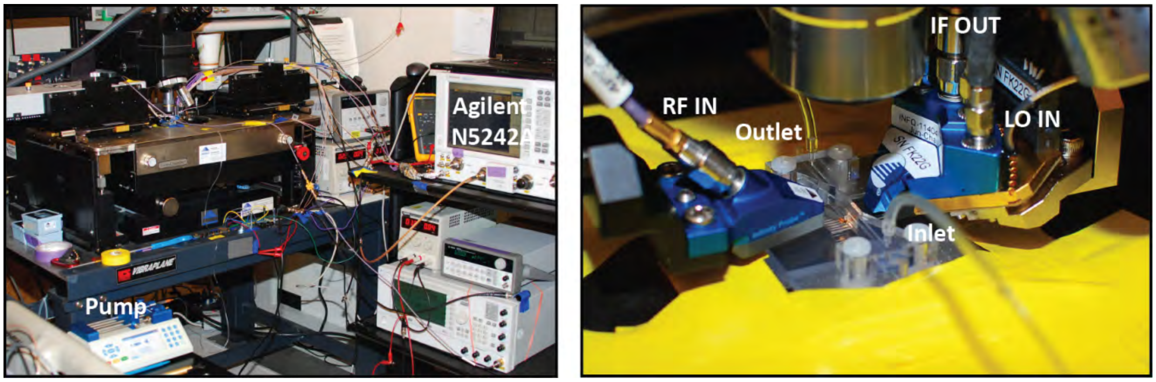

Figure 3.12: Measurement setup.

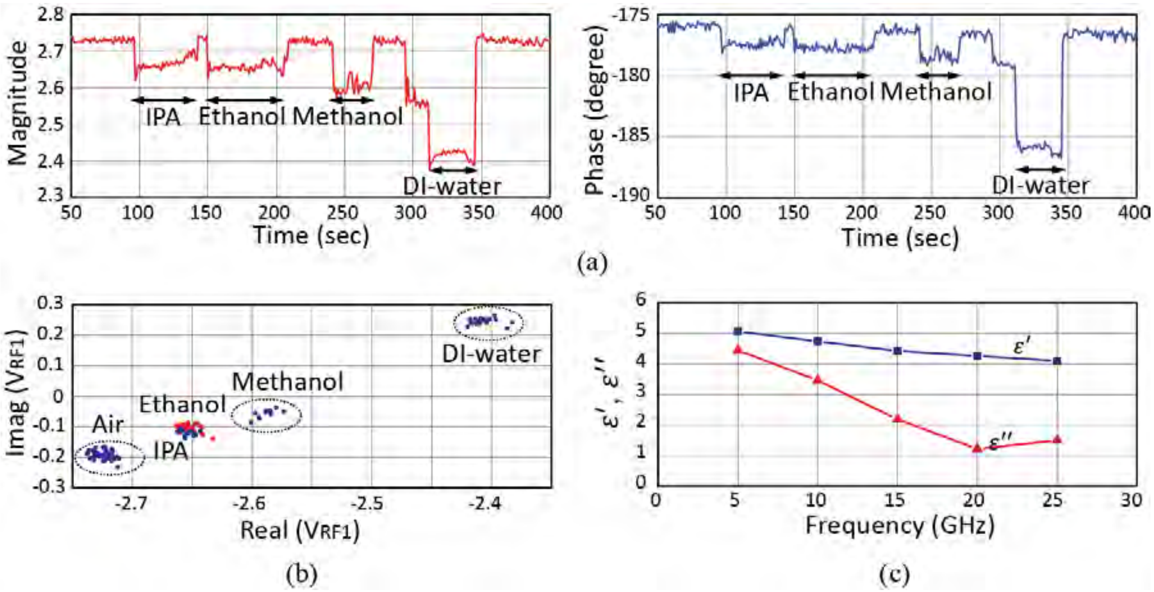

Figure 3.13: Measured signals of 4 different liquids in (a) time-domain (b) vector-plane. (c) Extracted permittivity of IPA.

Fig. 3.12 shows the photo of the measurement setup. Liquid samples are injected into the channel using a syringe pump and high precision step motor. Time-domain waveforms of normalized V_{RF1} at 20 GHz with four different sample liquids are shown in Fig. 3.13, which matches theoretical permittivity values. The normalized V_{RF1} for different samples is shown in the scatter plot on a vector plane. Clusters of different samples are clearly observed. With (3.23), the extracted permittivity of IPA versus frequency is plotted, showing accurate behavior that matches to the theoretical model [45]. The standard deviation of the extracted permittivity at 20 GHz is less than 1%. The sensitivity (SNR = 1) is also 1 % (= $|\Delta\varepsilon/\varepsilon|$) at $|\varepsilon|$= 4.45 at 100-Hz bandwidth. The effectiveness of CDS of canceling the baseline drift is demonstrated in Fig. 3.14. It is found that the sensitivity is not limited by the thermal noise as the output standard deviation remains relatively constant when adjusting the bandwidth between 10 and 1000

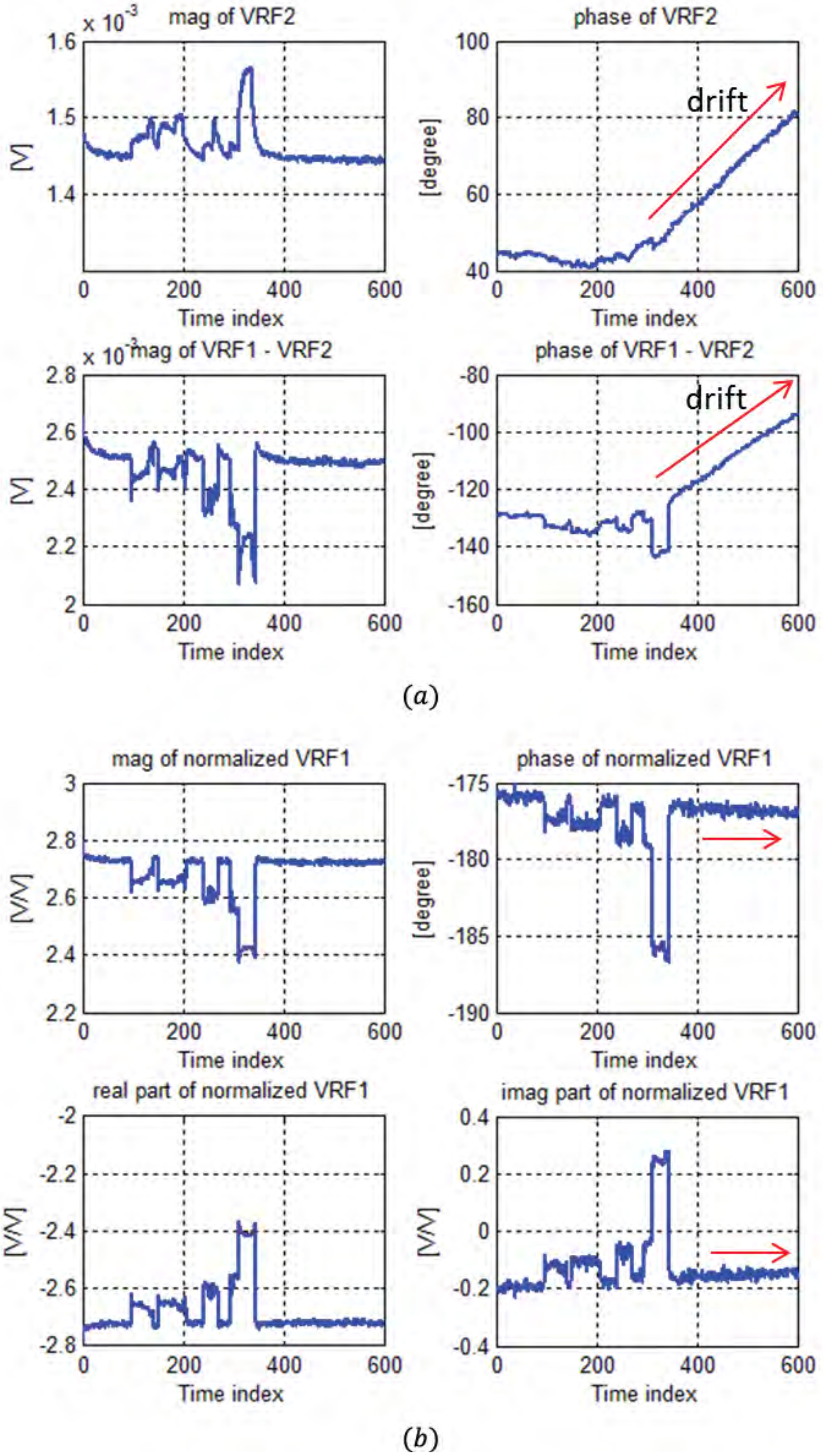

(a)

(b)

Figure 3.14: Drift mitigation: (a) measured raw data and (b) after applying CDS.

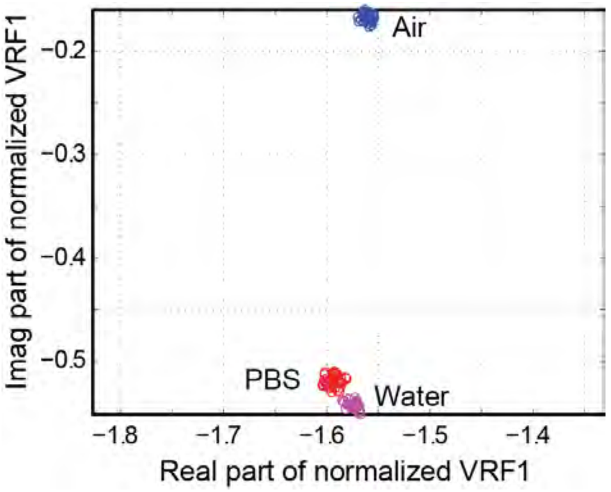

Figure 3.15: Measured normalized V_{RF1} of air, water, and PBS at 20 GHz.

General		
Technology		65-nm CMOS
Area		2000 µm x 600 µm
Power	DA	35 mA from 2.5V (1.3V on 50 Ω)
	Mixer/TIA	24 mW
	LO S2D	48 mW
Rx		
2-stage DA	Gain	12 dB w/o NC; 16dB w/ NC (5 GHz)
	3dB Bandwidth	60 GHz (w/o NC)
	Min. Noise Figure	4.2 dB
Rx	Gain	13 dB w/o NC; 16 dB w/ NC (5 GHz)
	Bandwidth	50 GHz (w/o NC)
	Min. Noise Figure	6.3 dB
Sensor		
CPW width/gap		10/4 µm
Microfluidics width		200 µm
Min. required sensing volume		30 µm x 200 µm x 15 µm (depth) ≈ 0.09 nL
Spectrum range		1 – 50 GHz
Sensitivity ($\lvert\Delta\varepsilon/\varepsilon\rvert$) at 20 GHz with SNR = 1 (100 Hz BW)		1 % at $\lvert\varepsilon\rvert$ = 4.45

Table 3.1: Performance summary.

Hz. More likely the noise floor is limited by the slow CDS switching rate (3 Hz) constrained by the MATLAB communication between the PC, FPGA, and the data acquisition of Agilent N5242 PNA. Fig. 3.15 shows the measurement of water versus

PBS (phosphate buffer saline, which resembles blood serum) at 20 GHz. Table 3.1 summarizes the sensor performance.

3.5 Chapter Summary

This chapter starts with an introduction of dielectric spectroscopy and explained the origin of dispersion in the complex permittivity. After discussing various sensor topologies, different impedance analyzer architectures were reviewed. To extend the frequency range with miniaturized instrumentation, a 1 – 50 GHz sensor prototype implemented in CMOS was presented. Measurement technique against sensor drift were highlighted and experimental results demonstrating the capability of the sensor for chemical mixture detection were presented.

Chapter 4

Injection-Locked Oscillator Sensors for Single-Cell Analysis

Flow cytometry, a process of electronically sorting and counting cells, is routinely used for medical diagnosis and disease monitoring, as commonly seen with CD4+ T-cell counts in HIV patients [46] and more recently with identifying circulating tumor cells (CTC) in cancer patients [47]. Most present day clinical flow cytometers use fluorescence-activated cell sorting (FACS), which requires bulky optical detection system. More importantly, the complex sample-labeling process, required by both fluorescent and magnetic-based assay systems, is the rate-limiting step both in regards to assay time as well as the wide-spread adoption in the point-of-care (POC) setting. In the application of regenerative medicine, labeling of cells with surface biomarker, which potentially interferes with cellular functionality, must be avoided when sorting cells of desired phenotype after stem cells differentiation [48]. This motivates the development of label-free flow cytometry.

Electrical impedance spectroscopy (EIS) [49] is an attractive approach for single-cell analysis. By measuring the electrical responses of the target sample under field excitation, direct assessment of biophysical properties enables label-free detection, an approach similar to mass, elasticity, and morphology measurements [50]. As an example, [51] demonstrates an impedance cytometer for whole blood cell analysis at 0.5 and 1.7 MHz with the integration of sample preparation in the microfluidics. One critical issue for low-frequency measurement is the screening of the signal due to both electrical double layer (EDL) at the electrode-electrolyte interface and the interfacial relaxation of cell membrane (the β-dispersion), resulting in ambiguous identification of different cellular subpopulation. Moreover, interferences caused by the variation of ionic strength in the physiological medium can hinder the signal of interest. Such effects are captured using equivalent circuit model of a cell passing through the sensing electrodes shown in Fig. 4.1(a) [52]. Additional chemical stimuli to modify cellular physiology or membrane permeability as well as polystyrene labeling are still inevitable [53 – 54].

The application of microwaves allows the probing of the intrinsic cytoplasm as the electric field easily penetrates through the cell membrane (Fig. 4.1(b)). Such bi-lipid layer

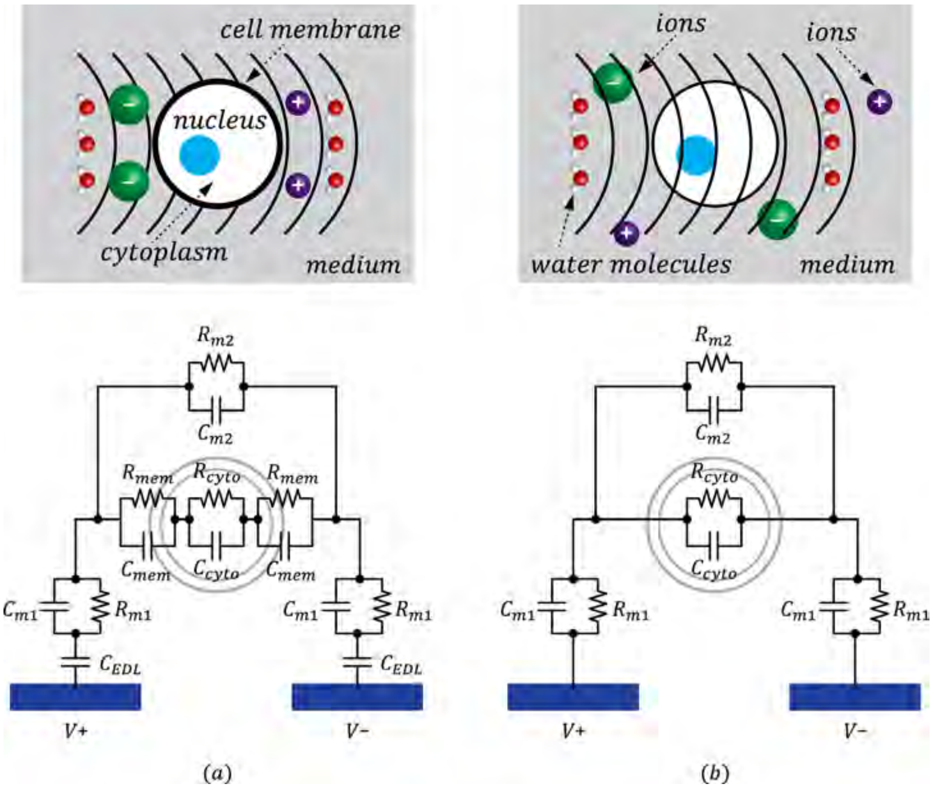

Figure 4.1: Equivalent circuit models at (a) MHz and (b) GHz for cells suspended in the medium.

with 5 nm of thickness presents 3 ~ 4 pF of capacitance for 10-µm diameter cells and becomes transparent at frequency above 1 GHz. This motivates the investigation of using microwave signature as effective discrimination between cells of different phenotypes [22]. In the past, such study is carried out with large amount of cells suspended in aqueous medium [31]; it is not until recently that [55] demonstrates there indeed significant difference (~ 10 %) in permittivity between colorectal cancer cells at different aggressive stages at 5 – 15 GHz. Though showing promising results, these measurements are carried out by dehydration of the medium after cells being loaded onto a MEMS resonator, potentially altering its physiological status. Therefore study in the frame closer to the clinical setting at larger scale is still necessary. It is worth mentioning that [56] implements an impedance sensor using off-the-shelves components at 500 MHz and is able to detect the size and the distribution of vacuoles between two different yeast cells while [57] is capable of studying yeast cell viability at 5 GHz using MEMS-based RF interferometry and vector network analyzer (VNA). Current state-of-the-art microwave (1.5 GHz) sensor for single-cell detection is presented in [58]; instead of probing the intracellular content, the sensor is aiming to detect the position of cells in the channel after dielectrophoresis (DEP) actuation.

CMOS has been the optimal technology for biomedical devices in clinical use. In addition to system miniaturization, unprecedented sensitivity can be achieved with on-CMOS direct sensing. Recently, different modalities have been demonstrated for cell-based analysis in CMOS, including the detection of red blood cell deformability using impedance analysis at 0.4 MHz [39], study of the pulsatile movement from mouse cardiac progenitor cells under changes in extracellular ion concentration using magnetic labeling [59], assay for personalized drug development using multi-modalities sensing platform [60], and extracellular recording of neuron network with large-scale microelectrode arrays [61]. CMOS systems dedicated for microwave sensing have also been demonstrated. For example, [62] integrates an on-chip coplanar waveguide (CPW) transmission-line sensor with broadband receiver for 1 – 50 GHz spectroscopy using S_{21} measurements; [63] utilizes similar approach at 9 MHz – 2.4 GHz with integrated on-chip signal source; [64] measures the frequency shift of a sensing oscillator in a phase-locked loop (PLL) at 7 – 9 GHz; [42] derives the complex permittivity of material-under-test (MUT) between 0.62 – 10 GHz from a capacitive half bridge. In addition, [65] and [66] implement integrated VNAs in SiGe process to measure the complex permittivity of aqueous solutions at frequencies ranging from 50 – 100 GHz and 118 – 133 GHz. However, none of the work offers the capability for single-cell detection; only chemical mixture is experimented at relatively large sample volume (e.g. 0.09 nL from [62]).

In this chapter, we present a CMOS spectrometer architecture aiming at characterizing dielectric responses at single-cell level between 6.5 – 30 GHz [67]. With sensing oscillator injection-locked to an excitation source, sample-induced frequency perturbation is converted to an output phase shift with electronically adjustable transducer gain. By exploiting such inherent phase amplification property, the proposed sensor offers sub-aF of capacitive sensitivity level at 100-kHz noise bandwidth under 1-V supply, allowing high-throughput flow cytometry for large-scale statistical study. Though the link between frequency modulation and phase shift has been widely exploited in different applications such as clock de-skewing [68], wireless beam-forming [69], frequency tuning in sub-THz signal generation [70], and Doppler radars [71 – 72], this work, to the authors' knowledge, explores the use of ILO phase amplification property in reactance sensing for the first time.

The chapter is organized as follows. Section 4.1 discusses the system specification for the sensor based on signal analysis and throughput requirement. The proposed system architecture based on injection-locked oscillator sensor is introduced in Section 4.2. System implementation, chopping techniques, and system noise analysis are discussed in Section 4.3. Section 4.4 and 4.5 presents the measurement results including both electrical characterization and the flow cytometry. Discussions are given in Section 4.6.

4.1 Signal Analysis and System Requirement

Fig. 4.2 shows a pair of coplanar electrodes in the flow cytometry setting performing differential-like measurements. As a cell flows across the sensing electrodes, the perturbed electrical fields result in a capacitance change between the electrodes. Such a

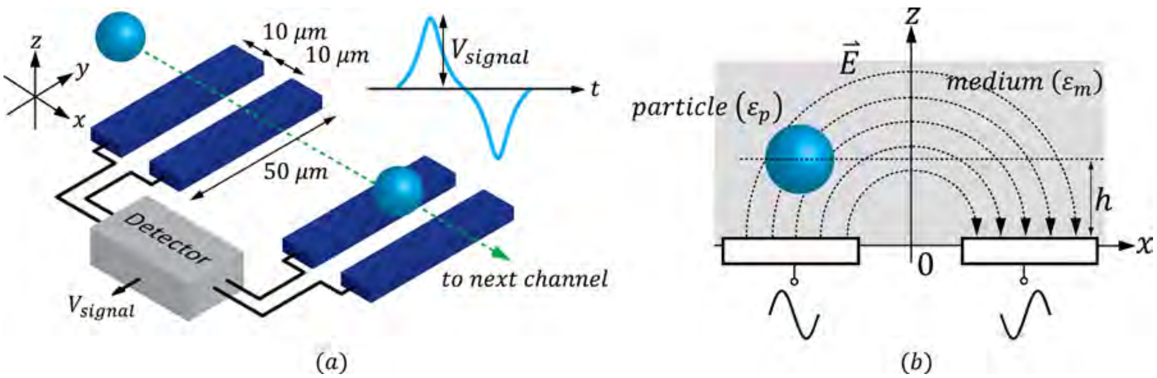

Figure 4.2: Electrodes arrangement in flow cytometry: (a) 3-D and (b) cross-section illustrations.

change can be derived by finding the perturbed system energy caused by an induced dipole moment ($\vec{p}$) due to the polarization of the cell:

$$\Delta U = \frac{1}{2}\Delta C {V_0}^2 = -\frac{1}{2}\vec{p}\cdot\overrightarrow{E_0}(\vec{r}), \tag{4.1}$$

where V_0 is the driving voltage, $E_0(r)$ is the electric field intensity in the medium, and the dot represents the inner product. From (4.1), the induced capacitance change can be expressed as [58]

$$\Delta C = 4\pi\varepsilon_m a^3 \mathrm{Re}\{K_{CM}\}\frac{|E_0|^2}{V_0^2}, \tag{4.2}$$

$$\begin{aligned} K_{CM} &= \frac{\varepsilon_p(\omega) - \varepsilon_m(\omega)}{\varepsilon_p(\omega) + 2\varepsilon_m(\omega)} = \frac{\Delta\varepsilon(\omega)}{\Delta\varepsilon(\omega) + 3\varepsilon_m(\omega)} \\ &= \frac{1}{1 + 3\frac{\varepsilon_m(\omega)}{\Delta\varepsilon(\omega)}}, \end{aligned} \tag{4.3}$$

where ε_m and ε_p are the permittivity of the medium and the cell, respectively, a is the radius of the cell, and K_{CM} is the Clausius-Mossotti factor, which describes the permittivity contrast between the cell (in shape of perfect sphere) and the medium. In the proposed sensor, K_{CM} is the main quantity to be measured; however, as can be seen in (2), both cell size and field intensity contribute to the overall capacitance change and require careful interpretation or calibration of the data. The size of the cell can be inferred by the addition of low frequency conductivity change similar to conventional Coulter counter [73]. On the other hand, field intensity is a strong function of the elevation and mandates precision control on the position of cells in the microfluidic channel to ensure consistent data while maximizing signal level. Fig. 4.3(a) shows the simulated field intensity along

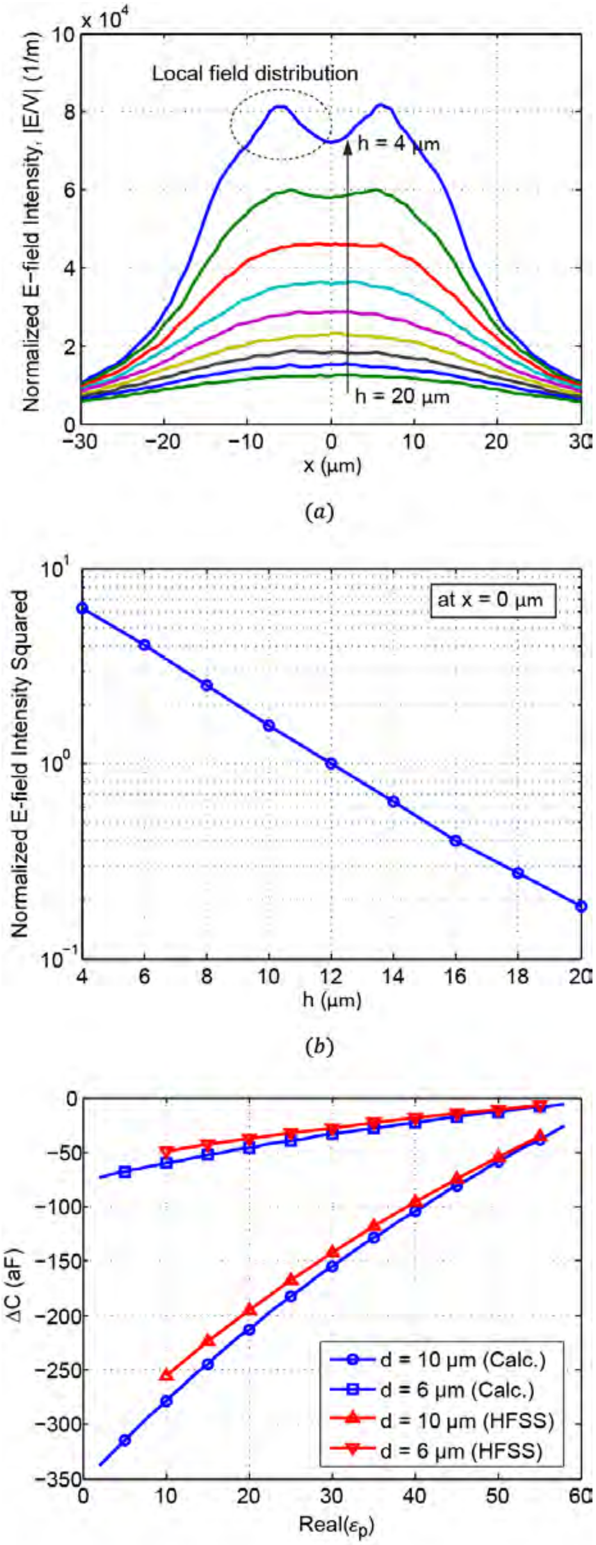

(a)

(b)

(c)

Figure 4.3: (a) Field distribution and (b) normalized field intensity at the center of electrodes. (c) Induced capacitance change.

different streamlines at an elevation *h* ranging from 4 to 20 μm above the electrodes. In this work, a pad-open layer with aluminum is used to define the electrodes and therefore no post-fabrication is required. Both the electrode width and pitch are 10 and 20 μm, respectively, optimized based on the integrity of the signal waveforms. Fig. 4.3(b) plots the square of the field intensity at different elevation along the *z*-axis with all the fields normalized to that at *h* of 12 μm. From Fig. 4.3(b), it is seen that the signal level is inversely proportional to the elevation, emphasizing the importance of the position control of the cells during the flow. Fig. 4.3(c) plots the capacitance changes from both the calculation (Eq. 2) and the HFSS simulation at different cell sizes. The induced capacitance change shows a sensitivity of 4 aF in 2.5 % of particle permittivity change (at nominal ε_p of 40) assuming the medium has permittivity (ε_m) of 65. Such an analysis can therefore be utilized to estimate the capacitance signal for system design. Note that discrepancy between the simulation and calculation is clearly observed in the figure. This is mainly due to the constant-field assumption in the calculation. On the other hand, it is important to point out that the HFSS simulated *absolute* capacitance change heavily depends on the granularity of the meshing. In order to resolve minute capacitance change during the permittivity sweep, *mesh re-use* must be employed between each simulation.

The requirements for the sensing precision in terms of the minimum detectable capacitance, is determined as follows. According to [55], there is approximately 10 % difference in the relative permittivity between the colorectal cancer cells at different aggressive stages. These percentage differences in permittivity translate to a capacitance change of 16 aF for cells with diameter of 10 μm. Consequently, sensor noise floor of 1 $\mathrm{aF_{rms}}$ is necessary for sufficiently high signal-to-noise ratio (*SNR*). In the layout, the electrodes length (50 μm) is selected to be comparable to the fluidic channel width (60 μm) to mitigate precise control of the flow streamline in the y-coordinate (Fig. 4.2(a)). Such geometry leads to water-loaded electrode capacitance of 29 and 16 fF at 5 and 30 GHz, respectively. Therefore the required detection limit of the sensor is 34.4 ppm (1 $\mathrm{aF_{rms}}$ out of 29 fF). In practice, due to extra routing and circuit capacitance, such limit will be lowered to 10 ppm (1 $\mathrm{aF_{rms}}$ out of 100 fF).

To achieve throughput comparable with the existing flow cytometry (> 1 kcells/sec), a filtering bandwidth of more than 1 kHz is necessary by approximating the measured signal with Gaussian pulses (signal bandwidth ≈ 0.44/FWHM). In practice, much higher bandwidth is mandatory as the flow rate needs to be increased to accommodate for the diluted cell concentration. This is to prevent the channel from clogging. In this work, the bandwidth requirement is much more stringent (~ 100 kHz) as the system must resolve local field distribution at the edge of the electrodes, as shown in Fig. 4.3(a)). As described in the flow cytometry experiments in section 4.5, such local peaks are used as an indication of the cell elevation.

It is essential to perform sensor calibration using size-traceable beads with known material properties prior to the cell measurements. As most polymers have relatively low permittivity, the sensor must support a dynamic range of 51 dB (= 350 aF / 1 $\mathrm{aF_{rms}}$) when calibrating with 10-μm diameter polystyrene beads ($\varepsilon_r = 2.2$) according to the curve in Fig. 4.3(c). Note that one extra bit (6 dB) must be included if the sensor outputs bipolar waveform (Fig. 4.2(a)). In fact, smaller bead size is acceptable for calibration purpose,

	Specification
Frequency Range	Microwave (5 ~ 30 GHz)
Minimum Resolvable Permittivity Difference	10 % ($\Delta\varepsilon = 4$ for $\varepsilon_{\text{cell}} \approx 40$)
Background (Physiological Solution)	$\varepsilon_{\text{m}} \approx 60$ (frequency dependent)
Signal Level (10-µm diameter cell)	16 aF
Required Noise Floor (SNR ≈ 16)	1 aF_{rms}
Target Throughput	1 ~ 10 kcell/sec
System Bandwidth	100 kHz
Dynamic Range (calibrate with 10-µm polystyrene beads)	51 dB (monopolar pulse) 57 dB (bipolar pulse) 44 dB (bipolar pulse, cal. with 6-µm polystyrene beads)

Table 4.1: Specification for dielectric spectroscopy flow cytometry.

relaxing the required dynamic range to 44 dB. Note that the fringing field measurement results in certain non-linearity in the capacitance-permittivity curve caused by the series configuration of the coupling and the sensing capacitors. Such curvature in the transfer curve can be calibrated with beads of known but different permittivity. Table 4.1 summarizes the design specification for the proposed flow cytometry.

4.2 Sensor Architecture

4.2.1 Conventional Oscillator-based Sensor

Oscillators are widely used for reactance sensing through shift in oscillation frequency [74, 75, 76, 77, 78]. As shown in Fig. 4.4(a), both high resolution and direct digitized readout can be achieved with simple counter-based frequency detection. Such an approach provides nearly unlimited dynamic range while the minimum resolvable frequency shift is limited by the residue frequency noise of the oscillator itself:

$$\Delta\omega_{n,rms}^{2} = \int_{0}^{\infty} S_{\phi}(\omega)|j\omega|^{2}|H_{LPF}(\omega)|^{2}d\omega, \tag{4.4}$$

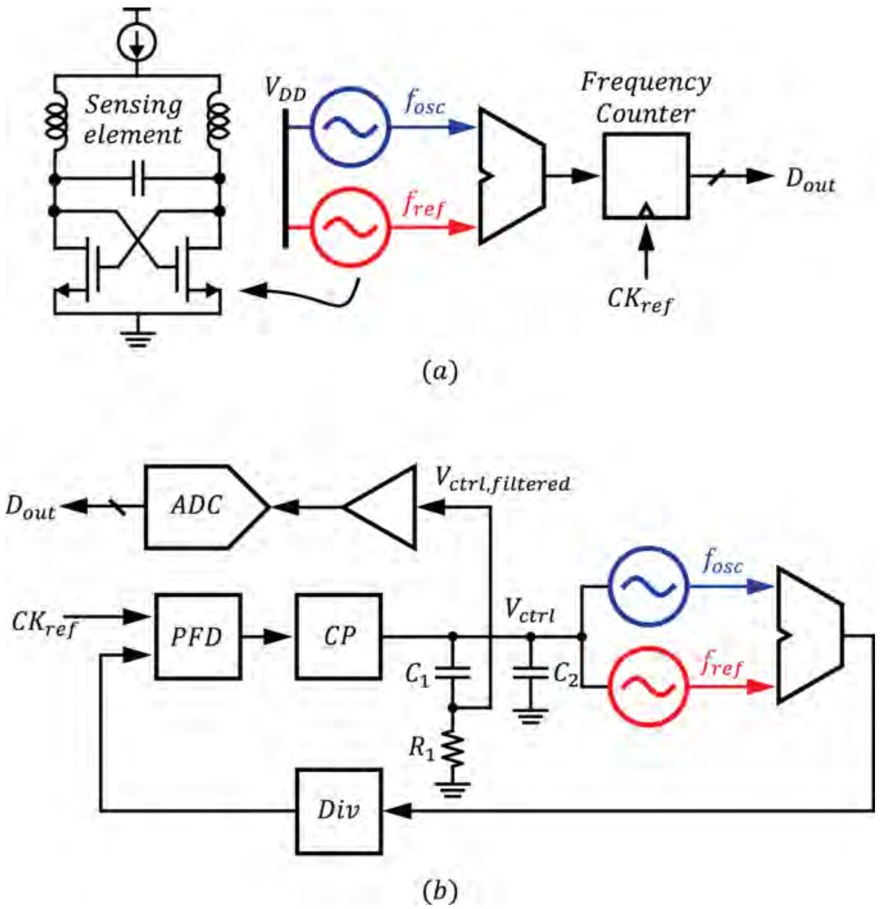

Figure 4.4: Oscillator-based sensor architecture. (a) Frequency counting and (b) PLL.

where $S_\phi(\omega)$ is the SSB phase noise of the oscillator and $H_{\mathrm{LPF}}(\omega)$ describes the noise-filtering applied to the sensor. In the actual implementation, the noise floor is determined by the accumulated timing jitter within the counting window τ_w [79][80]. By normalizing against the oscillation frequency ω_0, the noise-limited resolution is expressed as

$$\left(\frac{\Delta\omega}{\omega_0}\right)^2_{n,rms} = \frac{4}{\pi\omega_0^2\tau_w^2}\int_0^\infty S_\phi(\omega)\left[\sin\left(\frac{\omega\tau_w}{2}\right)\right]^2 d\omega. \tag{4.5}$$

For example, an oscillator at 10 GHz having a phase noise of -100 dBc/Hz at 1-MHz offset frequency will accumulate 10 ps of jitter in 100 μsec of counting window. The normalized frequency uncertainty is 0.1 ppm according to (4.5). Note that the counter noise has been excluded in the calculation.

To reduce frequency drift due to temperature variation and environmental interference, differential measurement with a reference oscillator is necessary and is carried out in a time-interleaving fashion to avoid mutual locking. Though slow-varying

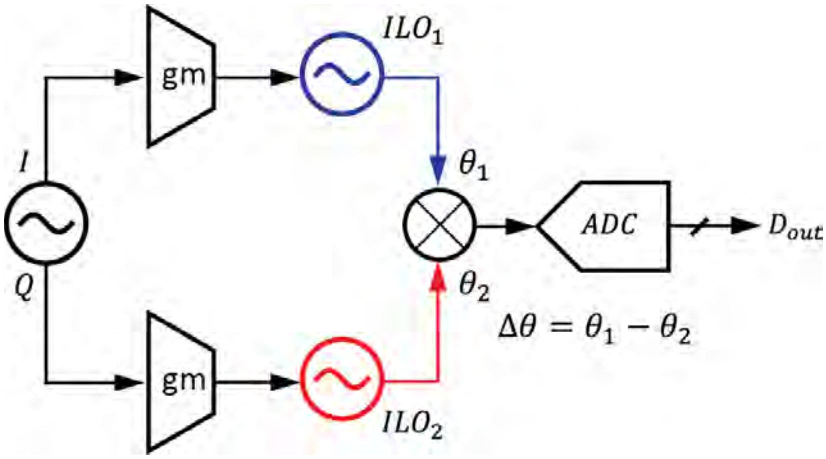

Figure 4.5: Proposed sensor architecture.

common-mode noise is mostly rejected, the measurement discontinuity between each oscillator can potentially incur unwanted noise penalty due to incomplete cancellation. This could be one of the reasons that even the state-of-the-art oscillator sensors do not reach the theoretical sensitivity limit calculated from (4.5) [80]. On the other hand, pushing the sensing frequency toward microwaves (~ 30 GHz) significantly increases the design complexity for the detection circuitries as both the multiplexer and the counter, in particular the 1st-stage in the counter chain, must be operating at the maximum speed. Frequency calibration is inevitable if narrowband tuned-loads are utilized in those building blocks. Down-conversion can be employed to relax power-speed trade-offs at the cost of higher susceptibility to the mixer noise due to slew rate reduction after low-pass filtering [78].

Another modality for detecting frequency shift is by embedding the oscillator within a phase-locked loop (PLL), as shown in Fig. 4.4(b) [64]. In such scheme, the sample-induced frequency shift is reflected on V_{ctrl} from the action of feedback. Though it is known that PLL shapes the VCO phase noise with high-pass filtering at the *output*, this is not true for sensing application as the VCO noise is also referred to V_{ctrl} through the phase error correction mechanism within the loop bandwidth. Besides the advantage of consistent excitation frequency during the sensing, such PLL-based measurements suffer from extra noise sources such as reference clock and charge pump. The speed is also limited speed due to stability constraint. Moreover, high performance baseband processing poses design challenges when K_{VCO} is high. Lastly, the demand for differential measurements results in higher complexity in the calibration procedure making this approach unsuitable for flow cytometry applications [81 – 82].

4.2.2 Proposed Injection-locked Oscillator (ILO) Sensor

Fig. 4.5 shows the simplified sensing architecture implemented in this work where both the sensing and the reference oscillators can operate in continuous mode, achieving the highest possible common-mode rejection. By injection locking the sensing oscillators with an excitation source, the perturbation of the oscillation frequency of either one of the

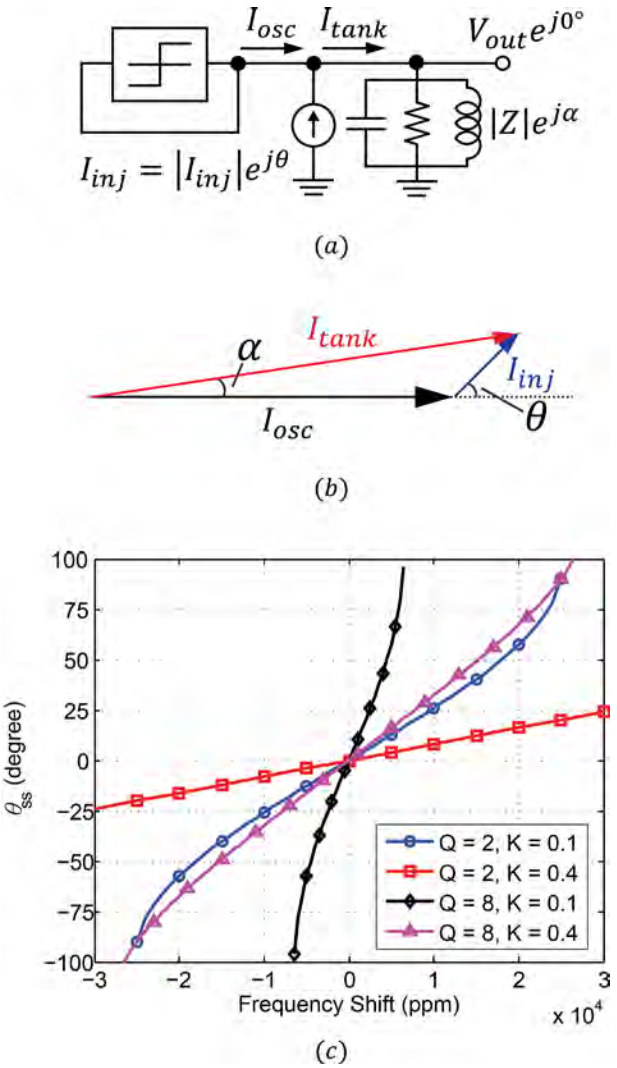

Figure 4.6: (a) Injection-locked oscillator model. (b) Steady-state phasor diagram. (c) Sensor transfer curve.

ILOs transduces to a differential phase shift presented at the input of the phase detector (PD). Fig. 4.6 shows the ILO model and the phasor diagram [83 – 84]. As ω_{inj} deviates from ω_{osc}, the injection current I_{inj} must bear a phase shift θ with respect to I_{osc} such that the total current I_{t} flowing into the tank exactly compensates the extra phase shift α introduced by the resonator. From trigonometry shown in the phasor diagram, it is obvious that the phase of the resonator α due to frequency perturbation is enhanced when referring to θ. It is such a phase amplification property that plays the major role in improving the sensor performance.

From Fig. 4.6(b), the steady-state phasors satisfy

$$\tan\alpha = \frac{I_{inj}\sin\theta_{ss}}{I_{osc} + I_{inj}\cos\theta_{ss}} \approx 2Q\frac{\Delta\omega}{\omega_0}, \tag{4.6}$$

where $\Delta\omega$ (= $\omega_0 - \omega_{\text{inj}}$) represents the frequency deviation between the injection and the resonance of the LC-tank. The *transducer* gain of the ILO can be found:

$$S_{\frac{\Delta\omega}{\omega_0}\to\theta_{ss}} = \frac{d\theta_{ss}}{d(\Delta\omega/\omega_0)} = 2Q\frac{(1 + K\cos\theta_{ss})^2}{K(K + \cos\theta_{ss})}, \tag{4.7}$$

where

$$K = \frac{I_{inj}}{I_{osc}}, \tag{4.8}$$

defines the coupling coefficient. Under weak injection ($K \ll 1$) and $\omega_{\text{inj}} \approx \omega_0$,

$$S_{\frac{\Delta\omega}{\omega_0}\to\theta_{ss}} \approx \frac{2Q}{K} = 2Q\frac{I_{osc}}{I_{inj}}, \tag{4.9}$$

which is proportional to the resonator *Q* and inversely proportional to the injection strength. Consequently, the weaker the injection, the higher the transducer gain. Another viewpoint for such phase amplification can be explained using ILO locking range. From transfer curve shown in Fig. 4.6(c), it is seen that θ_{ss} reaches approximately ±90° across the locking range. This is because phase synchronization effect is minimum as the injection and the oscillation currents are in quadrature, i.e. the impulse sensitivity of the oscillator is minimum at its voltage maximum [85]. Consequently, the injection locking transduces the frequency shift, which is an unbound parameter, to a bounded phase quantity with maximum of 180º, leading to an inherent sensitivity enhancement. Another important advantage of employing phase detection is that the sensor is capable of capturing a rapid response since the measurement is resolved at an edge-to-edge basis in contrast to frequency counting measurements where higher resolution mandates longer counting time.

4.2.3 Sensor Noise Analysis

As the system is configured as an interferometer, noise of the excitation source can be neglected due to self-mixing. On the other hand, phase noise of the ILOs is 1st-order high-pass filtered by the injection locking due to phase synchronization effect [86]. The high-pass filtering corner frequency can be derived through the *General Adler's Equation* [84]:

$$\frac{d\theta}{dt} = \omega_0 + \frac{\omega_0}{2Q}\frac{I_{inj}\sin\left(\theta_{inj} - \theta\right)}{I_{osc} + I_{inj}\cos\left(\theta_{inj} - \theta\right)}. \tag{4.10}$$

In (4.10), θ and θ_{inj} represents the instantaneous phase of the oscillation and injection currents, respectively. At locked state, $\theta = \omega_{\mathrm{inj}}t$ and $\theta_{\mathrm{inj}} = \omega_{\mathrm{inj}}t + \theta_{\mathrm{ss}}$. Applying perturbation analysis with $\theta = \omega_{\mathrm{inj}}t + \hat{\theta}$, $\left|\hat{\theta}\right| << 1$, and Taylor Series expansion, we arrive at the following differential equation describing the system dynamics [68][84][87]

$$\frac{d\hat{\theta}}{dt} = -\frac{\omega_0}{2Q}\frac{K(K + \cos\theta_{ss})}{(1 + K\cos\theta_{ss})^2}\hat{\theta} = -\frac{1}{\tau}\hat{\theta}. \tag{4.11}$$

where τ is the time constant for the system to reject the perturbation. The corner frequency of the high-pass filtering, or the injection-locking bandwidth, is therefore

$$\omega_p = \frac{1}{\tau} = \frac{\omega_0}{2Q}\frac{K(K + \cos\theta_{ss})}{(1 + K\cos\theta_{ss})^2}. \tag{4.12}$$

The total integrated phase noise at the output of ILO is

$$\phi_{n,rms}^2 = \int_0^\infty S_\phi(\omega)\left|H_{inj,HPF}(\omega)\right|^2 |H_{LPF}(\omega)|^2 d\omega, \tag{4.13}$$

$$H_{inj,HPF}(\omega) = \frac{j\dfrac{\omega}{\omega_p}}{1 + j\dfrac{\omega}{\omega_p}}. \tag{4.14}$$

Assuming the bandwidth of noise filtering is much smaller than that of injection locking, the minimum detectable frequency shift normalized to ω_0 can be derived by dividing (4.13) to (4.7) with (4.12):

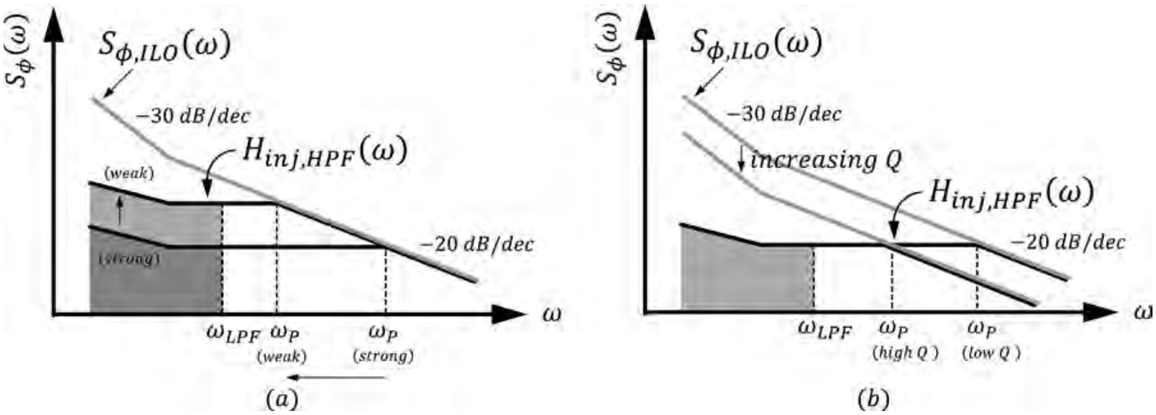

Figure 4.7: ILO phase noise shaping: (a) reducing injection strength and (b) increasing tank Q.

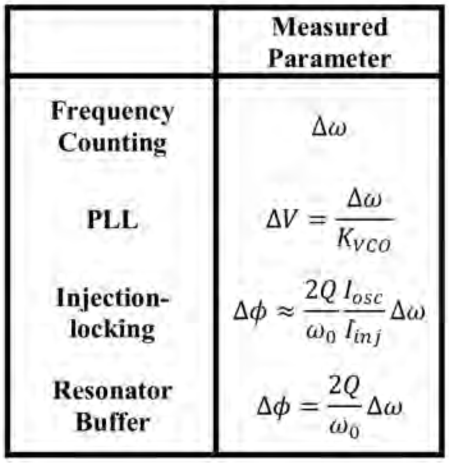

	Measured Parameter
Frequency Counting	$\Delta\omega$
PLL	$\Delta V = \frac{\Delta\omega}{K_{VCO}}$
Injection-locking	$\Delta\phi \approx \frac{2Q}{\omega_0}\frac{I_{osc}}{I_{inj}}\Delta\omega$
Resonator Buffer	$\Delta\phi = \frac{2Q}{\omega_0}\Delta\omega$

Table 4.2: Measurement parameters.

$$\begin{aligned}\left(\frac{\Delta\omega}{\omega_0}\right)^2_{n,rms,ILO} &= \frac{1}{\omega_0^2}\frac{\phi_{n,rms}^2}{S^2_{\frac{\Delta\omega}{\omega_0}\rightarrow\theta_{ss}}} \\ &\approx \int_0^\infty S_\phi(\omega)\frac{\omega^2}{\omega_0^2}|H_{LPF}(\omega)|^2 d\omega. \qquad (4.15)\end{aligned}$$

Interestingly, (4.15) shows that the noise floor is constant regardless of *K* and θ_{ss}. This is because ω_p scales with the transducer gain in an opposite way, i.e. weak injection results in the lowering of the injection locking bandwidth, which compensates the increase of the transducer gain. Fig. 4.7(a) illustrates the effect of injection strength on the shaped phase noise. It is important to note that (4.15) bears the same result as (4.4), the sensitivity limit in frequency counting approach. This is of no surprise as both modalities shares the same sensing principle. Nevertheless, the high transducer gain offered by the injection locking is still beneficial in sensor design for rejecting noise sources from the subsequent stages, similar to the role of low-noise amplifier (LNA) in a receiver chain. Including the noise from PD, the input-referred noise floor is

$$\left(\frac{\Delta\omega}{\omega_0}\right)^2_{n,rms} = \left(\frac{\Delta\omega}{\omega_0}\right)^2_{n,rms,ILO} + \int_0^\infty \frac{v^2_{n,PD}(\omega)}{K^2_{PD}\cdot S^2_{\frac{\Delta\omega}{\omega_0}\rightarrow\theta_{ss}}}|H_{LPF}(\omega)|^2 d\omega, \tag{4.16}$$

where $v_{\mathrm{n,PD}}(\omega)$ and K_{PD} are the noise PSD and the gain of the phase detector, respectively.

It is of interest to compare the signal and noise property between the frequency counting and injection locking as a function of the resonator *Q*. In the frequency counting measurement, the sensitivity limit improves with higher *Q* due to the reduction of the oscillator phase noise. On the other hand, the integrated phase noise at the output of ILO stays constant; it is the enhancement in transducer gain that helps in lowering the input-referred noise floor. Such phenomenon is depicted in Fig. 4.7(b) graphically. Finally, it is important to bear in mind that the proposed sensing architecture avoids time interleaving and hence maintains the highest possible common-mode rejection.

Table 4.2 compares the measured parameters between different modalities. By stopping the oscillation, the LC resonator can be configured as the load of an amplifier in the same phase-detecting interferometry. Such an approach avoids the phase noise amplification due to the absence of the positive feedback [88]. However, as the signal is only amplified by the *Q* of the resonator, the minimum detectable frequency shift is identical with that of the ILO sensors. This is again of no surprise as it is the same resonator that implements the fundamental sensing element. Nevertheless, injection locking outperforms all the methods due to its inherent phase amplification.

From the aforementioned discussion, two mutual injection-locked oscillators seem to be the optimum sensor configuration, which combines the benefits of interferometry and injection-locking signal amplification. Indeed, noise is reduced but not completely nulled while the effective phase shift induced by frequency perturbation is lowered, leading to constant SNR. Detailed analysis on two mutual injection-locked oscillators will be shown in Section 4.6.2. The results are also generalized to N-stage coupled oscillators.

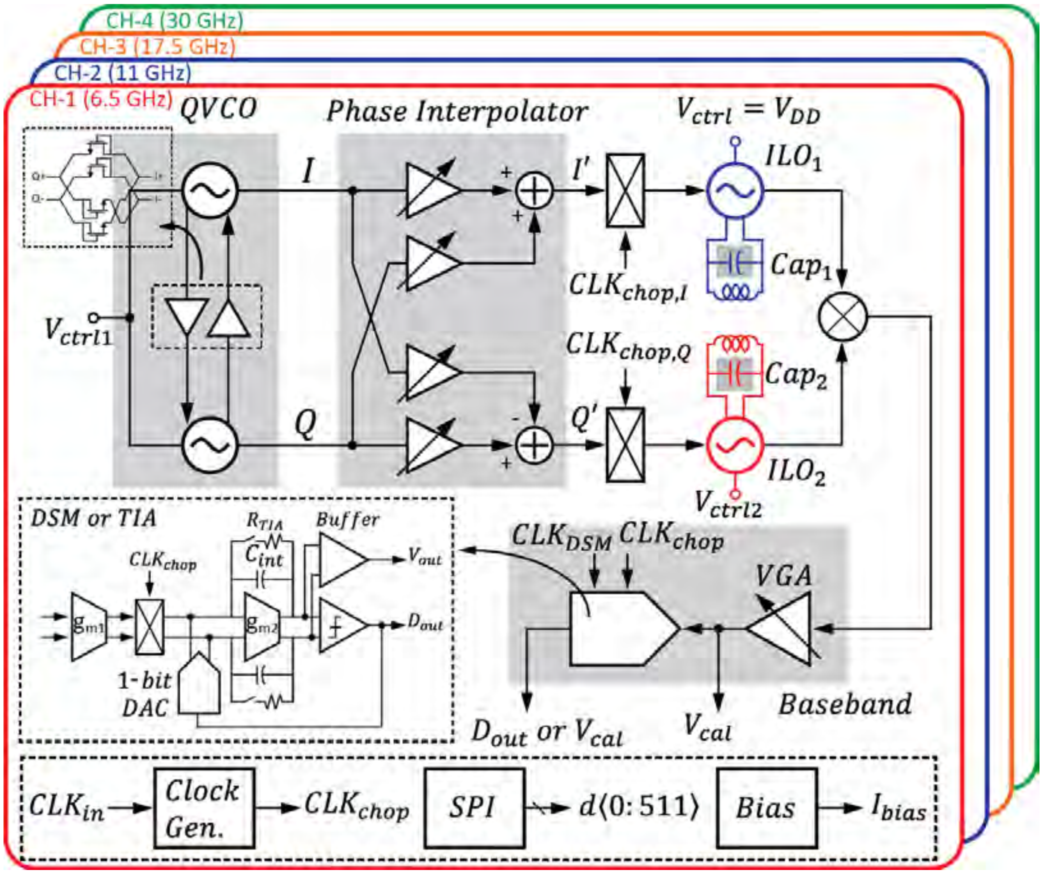

Figure 4.8: Sensor block diagram.

4.3 Circuit Implementation

4.3.1 System Architecture

Fig. 4.8 shows the complete system block diagram of the proposed spectroscopic sensor prototype consisting of four channels in series to probe the dielectric property of the target cells at 6.5-, 11-, 17.5-, and 30-GHz frequencies. Such frequency range is selected to cover the broad dispersion of water relaxation centered around 18 GHz while each frequency is determined to avoid inter-channel coupling at higher harmonics and more importantly, the mutual pulling between the oscillators. The core of each channel consists of two injection-locked oscillators (ILOs) performing differential sensing using pairs of 50 µm × 10 µm pad-layer electrodes with 20-µm pitch, driven by a wideband QVCO, and a Gilbert mixer for phase detection. The ILOs are implemented with NMOS differential oscillator with analog controlled varactor for frequency calibration purpose. The QVCO is implemented with two differential LC-oscillators anti-phase coupled with

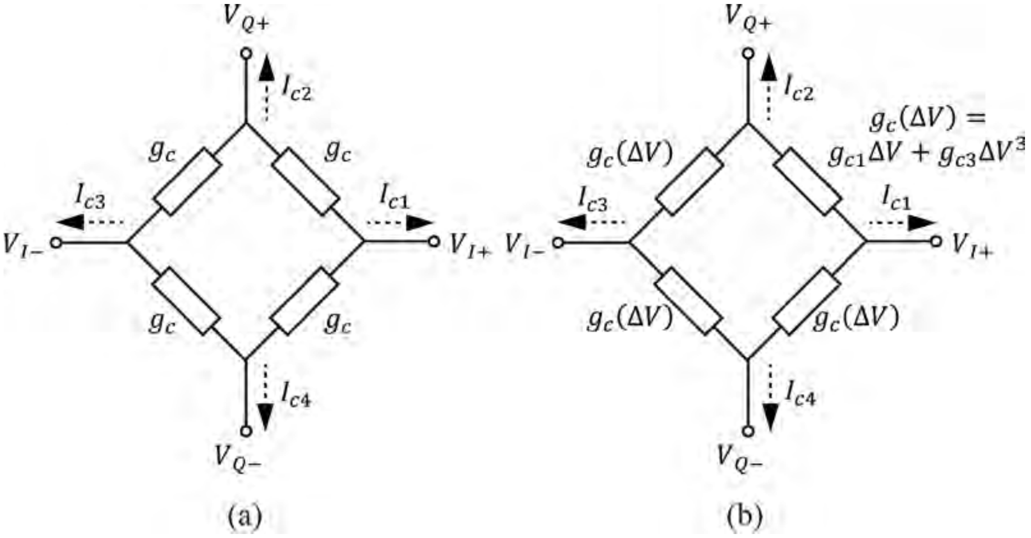

Figure 4.9: Four-port coupled oscillator (a) with linear couplers and (b) nonlinear couplers.

diode-connected NMOS. Such an approach is preferred against passive 90º phase shifter due to its simplicity and highly symmetric layout. To accommodate large frequency deviation (~ 5 %) as ILOs are loaded with air ($\varepsilon_r = 1$) and aqueous sample such as water ($\varepsilon_r = 80$), the QVCO is designed with > 14 % of tuning range. To maximize the conversion gain of the phase detector (PD), the QVCO outputs are interpolated through summation and subtraction to cancel the quadrature phase error. Moreover, such phase interpolation rejects the uncorrelated phase noise from the QVCO outputs through PM-to-AM conversion. Chopping is included through phase modulation along the RF path to mitigate signal corruption due to baseband flicker noise and will be discussed in the next section. A 8.5 – 24.5 dB gain VGA is followed by a 1st-order CT-ΣΔ modulator for signal digitization with off-chip decimation filtering. The demodulation of the signal is embedded within the modulator with NMOS switches. The integrator in the ΣΔ modulator can also be configured into a TIA by enabling the resistive paths for direct analog readouts.

4.3.2 QVCO with Passive Couplers

In this section, the fundamentals of the QVCO employing passive couplers are presented. Consider a four-port oscillator model coupled through linear passive devices shown in Fig. 4.9(a). The coupling currents injected into V_{I+} are

$$I_{c1} = g_c\left[\left(V_{Q+} - V_{I+}\right) + \left(V_{Q-} - V_{I+}\right)\right] = -2g_cV_{I+}, \tag{4.17}$$

where g_c is the conductance of the coupling devices. As expected, coupled oscillator with linear devices bears a desirable in-phase injection. However, due to such in-phase coupling, any phase relationship can be sustained at four ports as long as the net phase

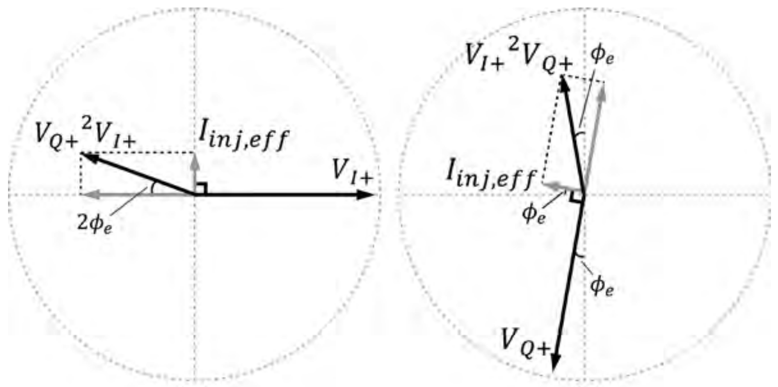

(a) (b)

Figure 4.10: Phasor diagram illustrating effective injection currents in (a) I_{c1} and (b) I_{c2}.

around the loop is an integer multiple of 2π. This can be understood in another way. Suppose that such a linearly coupled oscillator is already in perfect quadrature and no LC-tank mismatch exists. What happens when one of the tank's resonance frequencies is lowered by Δω? Since all the coupling currents are in-phase with respect to the terminal voltages, there's no mechanism to compensate for such a frequency-induced phase shift in the LC-tank and hence Bark- hausen's criteria cannot be maintained. On the other hand, assume the coupling device exhibits the following nonlinear *I-V* behavior: $I_c = g_{c1}\Delta V + g_{c3}\Delta V^3$, where ΔV is the terminal voltage across the device. The coupling currents injected into V_{I+} is

$$I_{c1} = g_{c1}\left[\left(V_{Q+} - V_{I+}\right) + \left(V_{Q-} - V_{I+}\right)\right] + g_{c3}\left[\left(V_{Q+} - V_{I+}\right)^3 + \left(V_{Q-} - V_{I+}\right)^3\right]$$

$$= -2g_{c1}V_{I+} - g_{c3}\left(2V_{I+}{}^3 + 6V_{Q+}{}^2V_{I+}\right). \qquad (4.18)$$

Since V_{I+} and $V_{I+}{}^3$ are both in-phase with the nodal voltage, they behave exactly the same as the coupled oscillator using linear passives. On the other hand, $V_{Q+}{}^2V_{I+}$ bears an orthogonal component (with respective to nodal voltage) that allows the compensation of phase shift due to mismatch in the LC-tank. To see this, the fundamental component in $V_{Q+}{}^2V_{I+}$ is derived supposing that $V_{I+} = V_0\cos(\omega_0 t)$ and $V_{Q+} = V_0\cos(\omega_0 t - \pi/2 - \phi_e)$:

$$V_{Q+}{}^2V_{I+} = \frac{1}{2}V_0{}^2V_{I+} - \frac{1}{4}V_0{}^3cos(\omega_0 t - 2\phi_e), \qquad (4.19)$$

where ϕ_e is the quadrature phase error and V_0 is the oscillation amplitude. Note that the 2nd term in (3) can be decomposed into an in-phase and orthogonal components:

$$cos(\omega_0 t - 2\phi_e) = cos(2\phi_e)cos(\omega_0 t) + sin(2\phi_e)sin(\omega_0 t). \qquad (4.20)$$

Fig. 4.10(a) plots the phasor diagram. It can be seen that the nonlinear coupler creates an orthogonal component ($I_{inj,eff}$) to compensate for any frequency-mismatch-induced phase

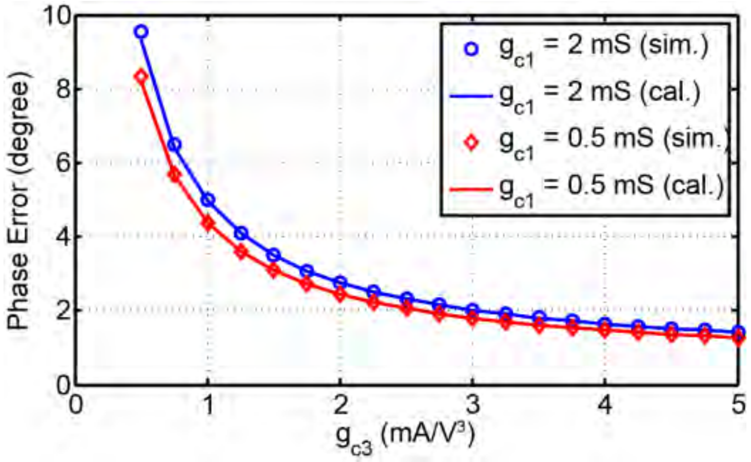

Figure 4.11: Phase error versus g_{c3} at different g_{c1}.

shift from the LC-tank. Therefore quadrature phase locking can be achieved. The same procedure can be applied to the coupling current (I_{c2}) flowing into V_{Q+} with corresponding phase diagram shown in Fig. 4.10(b).

Phase error dependency on the matching property of different parameters can be analyzed using a perturbation method around the ideal quadrature solution using KVL matrices. Alternatively, the phasor diagram in Fig. 4.10 can assist the derivation of phase error if only the reactance mismatch between the two oscillators is of interest. From (4.18) and (4.20),

$$I_{\mathrm{inj,eff}} = \frac{3}{2} g_{c3} sin(2\phi_{\mathrm{e}}) {V_0}^3. \tag{4.21}$$

Given I_{osc} to be the oscillation current in each differential oscillator and assuming that the in-phase coupling current is negligible compared to I_{osc}, the phase shift introduced by $I_{\mathrm{inj,eff}}$ of I_{c1} (or I_{c2}) is

$$tan\theta \approx \theta = \frac{I_{\mathrm{inj,eff}}}{I_{\mathrm{osc}}} = \frac{\frac{3}{2} g_3 \, sin(2\phi_{\mathrm{e}}) \, {V_0}^3}{I_{\mathrm{osc}}}. \tag{4.22}$$

The phase error with respect to LC-tank mismatch is derived:

$$2\phi_{\mathrm{e}} = \frac{2}{3} \frac{I_{\mathrm{osc}}}{g_{c3} {V_0}^3} Q \frac{\Delta\omega}{\omega_0}. \tag{4.23}$$

Assuming the oscillation amplitude is proportional to the oscillation current ($I_{\mathrm{osc}} = V_0 G_{\mathrm{tank}}$) and with $Q = \omega_0 C_{\mathrm{tank}} / G_{\mathrm{tank}}$,

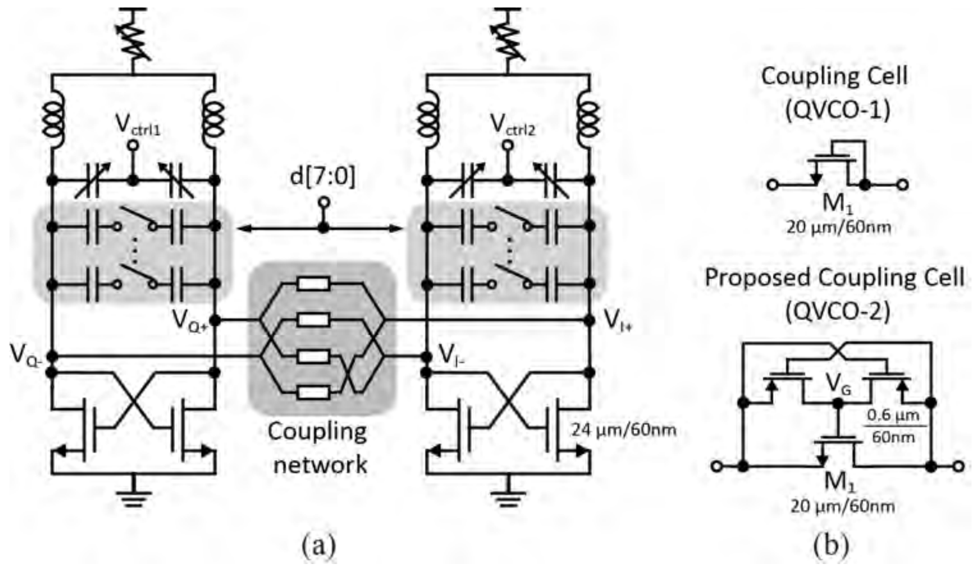

Figure 4.12: (a) QVCO schematic and (b) the coupling cells.

$$\phi_{\mathrm{e}} = \frac{1}{3}\frac{\omega C_{\mathrm{tank}}}{g_{\mathrm{c3}}{V_0}^2}\frac{\Delta\omega}{\omega_0} \sim \frac{1}{g_{\mathrm{c3}}{V_0}^2}. \tag{4.24}$$

From (4.24), two properties are observed. First, phase error is reduced with larger g_{c3} due to increased $I_{\mathrm{inj,eff}}$. Second, the phase error is inversely proportional to the amplitude square and hence increasing the oscillation amplitude helps in lowering phase error with much greater extent. To validate (4.24), Fig. 4.11 shows the simulated and the calculated phase error of a QVCO using modeled nonlinear passives with 1% capacitance mismatch introduced between the two LC-tanks. Excellent match between simulation and modeling is achieved. Note that in order to decouple the influence of high order harmonics on the phase error, an ideal filter is used such that all the high-order harmonics from coupling device are filtered out before entering into the corresponding tank. In this way, the simulation result reflects only the effect from the device nonlinearity on the coupling currents at the fundamental frequency. Indeed high order harmonics affect phase accuracy; nevertheless, their impact is already not pronounced due to the frequency selectivity of the LC-tank. A full transistor model is utilized in each differential oscillator with a total width of 48 μm for the cross-coupled pair. Inclusion of harmonic filter ensures that the quadrature locking is not achieved through super-harmonic coupling. Simulation is conducted at 26 GHz with the following LC-tank values: L = 125pH with Q = 12 at 26 GHz and C_{tank} = 0.15pF.

Study of the g_{c1} impact is also shown in Fig. 4.11. Phase error is degraded with larger g_{c1}. This is caused by the lowering of the tank swing as the effective loading from the couplers to the LC-tank is increased. However, 3rd-order nonlinearity plays a more dominant role.

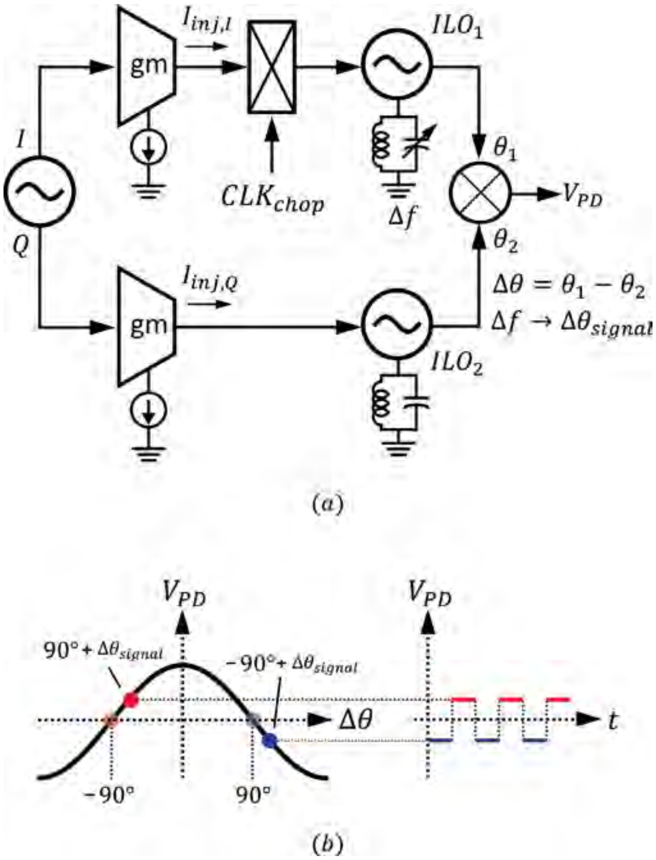

Figure 4.13: (a) BPSK chopping technique and (b) its operation plotted on PD transfer curve.

4.3.3 Coupler Non-linearity Enhancement

After discussing the importance of coupler nonlinearity, two coupling cells are implemented for comparison (Fig. 4.12). QVCO-1 employs conventional diode-connected devices where the phase accuracy can only be improved through up-sizing the devices at the expense of significant parasitic loading. Fig. 4.12(b) shows the schematic of the proposed coupling cell (QVCO-2). The idea is to implement a bi-directional diode with the addition of two tiny PMOS switches which turn on alternatively, allowing coupling current through M_1 to reverse its direction within an oscillation cycle. Consequently, $g_{c1}$and g_{c3} are doubled without introducing heavy loading. Interestingly,

such a configuration further helps in enhancing g_{c3} thanks to the nonlinearity of the PMOS. For another perspective, view the PMOS as a sampling mixer which generates 2nd harmonic at the gate of NMOS (V_G), which mixes with the coupling current at the fundamental frequency through M_1.

4.3.4 Phase Chopping Technique

Chopping is widely used in interferometers to mitigate the influence of interference and detector flicker noise by periodically blocking the signal in one of the paths. In this paper, we term such a scheme OOK modulation to resemble signal modulation in communication system. As phase is of interest in this work, chopping can be similarly achieved through BPSK modulation applied to one single path. Fig. 4.13 exhibits how the chopping is achieved with the aid of signal points on the PD transfer curve. It is important to point out that the actual phase signal is not truly chopped; in fact, it is the gain inversion property presented in the transfer curve of a mixer-based PD in the vicinity of ±90° that implements the chopping behavior at the PD output. The main advantage of pursuing BPSK modulation is the doubling of the signal level when compared with OOK modulation.

One critical issue for BPSK modulation is the high DC offset caused by large chopping ripples due to inevitable ILO locking transient. To understand this, let's examine the phase dynamics in an intuitive way as the injection signal experiences 180º phase inversion. First, consider the steady-state ILO waveforms in Fig. 4.14(a) where $\omega_{\mathrm{inj}} > \omega_{\mathrm{osc}}$ (high-side injection) and hence positive phase difference θ is presented between I_{inj} and V_{osc}. As I_{inj} is inverted, V_{osc} will shift in the direction of increasing θ to approach the new steady-state phase through phase interpolation between V_{osc} and the inverted I_{inj}. On the other hand, the phase inversion of I_{inj} will results in V_{osc} being pulled in the direction of decreasing θ_{ss} if $\omega_{\mathrm{inj}} < \omega_{\mathrm{osc}}$ (low-side injection), as shown in Fig. 4.14(b). On the phasor diagram, this indicates that V_{osc} will rotate in either clockwise or counter-clockwise direction depending on the polarity of the frequency difference, meaning that the process is deterministic.

Fig. 4.15(a) shows the phasor dynamics as BPSK modulation applied to the *Q*-path together with the signal trajectory along the PD transfer curve assuming high-side injection on both ILOs. As only *Q*-path is being chopped, input phase will traverse along the PD transfer curve from point A to C and wrap around to re-start from point A again.

As such a sequence determines the signal polarity of the chopping ripples, it is obvious that demodulation results in high DC offset as shown in the simulated waveforms (Fig. 4.16(a)).

One possible solution to prevent offset from saturating the basedband circuitries is time-gating the ripples at the PD output. However, this approach suffers from unpredictable residual ripple as the precise locking time constant is not known. On the other hand, a wider gating window results in significant loss in the signal level and is not preferred.

4.3.5 Ping-Pong Nested Chopping

This paper proposes a ping-pong chopping technique to circumvent such offset issue without introducing system complexity (Fig. 4.15(b)). The idea is to chop both I and Q

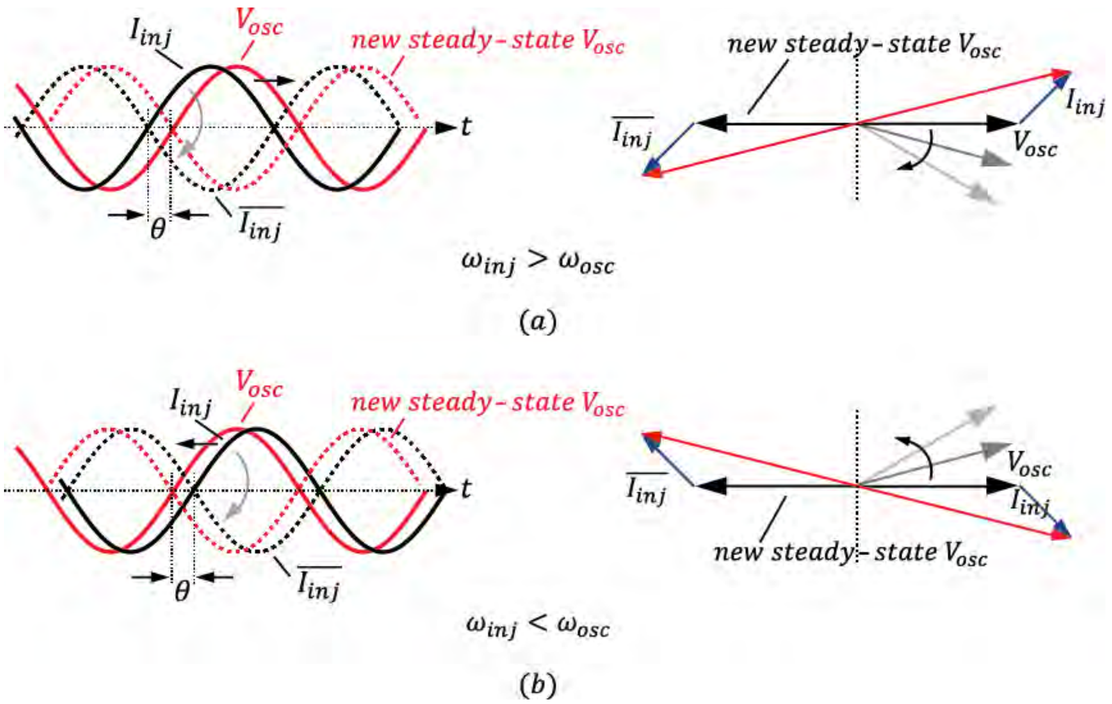

Figure 4.14: BPSK modulated phasor dynamics: (a) high-side injection and (b) low-side injection

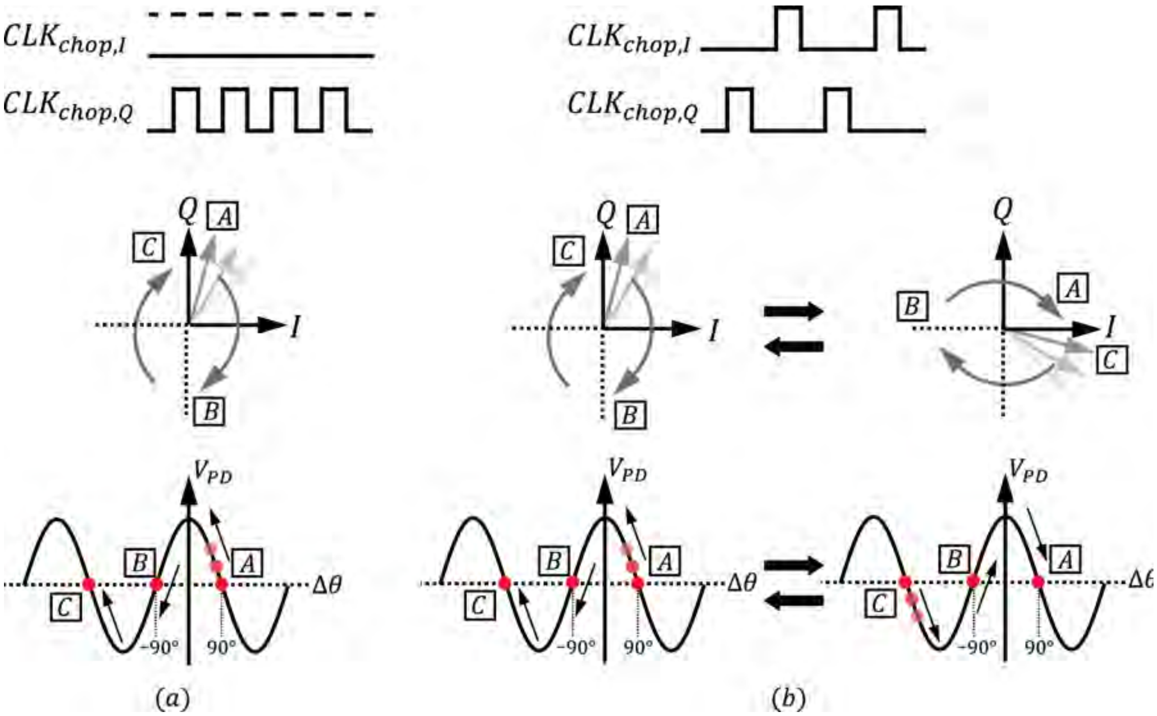

Figure 4.15: Phasor dynamics: (a) BPSK and (b) the proposed ping-pong nested chopping.

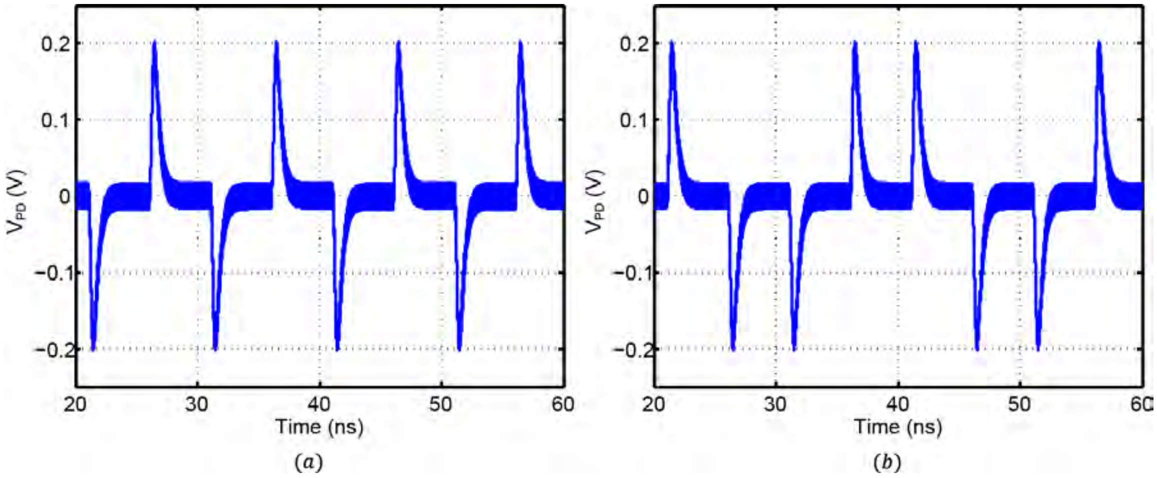

(a) (b)

Figure 4.16: Simulated waveforms at PD output with (a) BPSK chopping and (b) the proposed ping-pong nested chopping.

paths sequentially with 25% duty-cycle clocks such that the phase difference presented to PD will transverse back and forth along the PD transfer curve between point A and C and therefore modulating the ripple at half of the chopping frequency (Fig. 4.16(b)). This leads to the effect of nested chopping without introducing any additional choppers along the high-frequency signal paths. As ripples are self-cancelled pair-wise after demodulation, chopping offset is reduced. Finally, it is important to point out that ω_{inj} must be either higher or lower than the oscillation frequency of both ILOs. If ω_{inj} lies in between the two oscillation frequencies, the effect of nested chopping will vanish.

Fig. 4.17 shows the schematic of the injection-locked oscillator, PD, and clock generation circuitries. Phase chopping is achieved through current commutators stacking on top of the I/Q phase interpolation stage. The Gilbert mixer is split into two with their LO and RF inputs swapped to present balanced loads to each of the ILO sensors. Gating switches are inserted at the output of PD for comparison purpose. The ping-pong chopping clocks as well as the gating control signals are derived from an off-chip 400-MHz clock. The chopping frequency is 50 MHz and the gating windows can be selected between 2.5 and 5 ns.

4.3.6 System Noise Analysis

Fig. 4.18 shows the model for analyzing the sensor system noise. In addition to the ILO and PD noise discussed in section III-C, the sensor also suffers from both the injection current noise and the QVCO phase noise, which can leak to the output due to a path mismatch. Referring all noise sources to the input of the PD, the noise PSD can be described as

$$\phi_n^2(\omega) = 2S_{\phi,ILO}(\omega)\left|H_{inj,HPF}(\omega)\right|^2 + \frac{v_{n,BB}^2(\omega)}{K_{PD}^2} + 2i_{n,I_{inj}}^2(\omega)\cdot K_{I_{inj}}^2 \cdot \left|H_{inj,LPF}(\omega)\right|^2$$

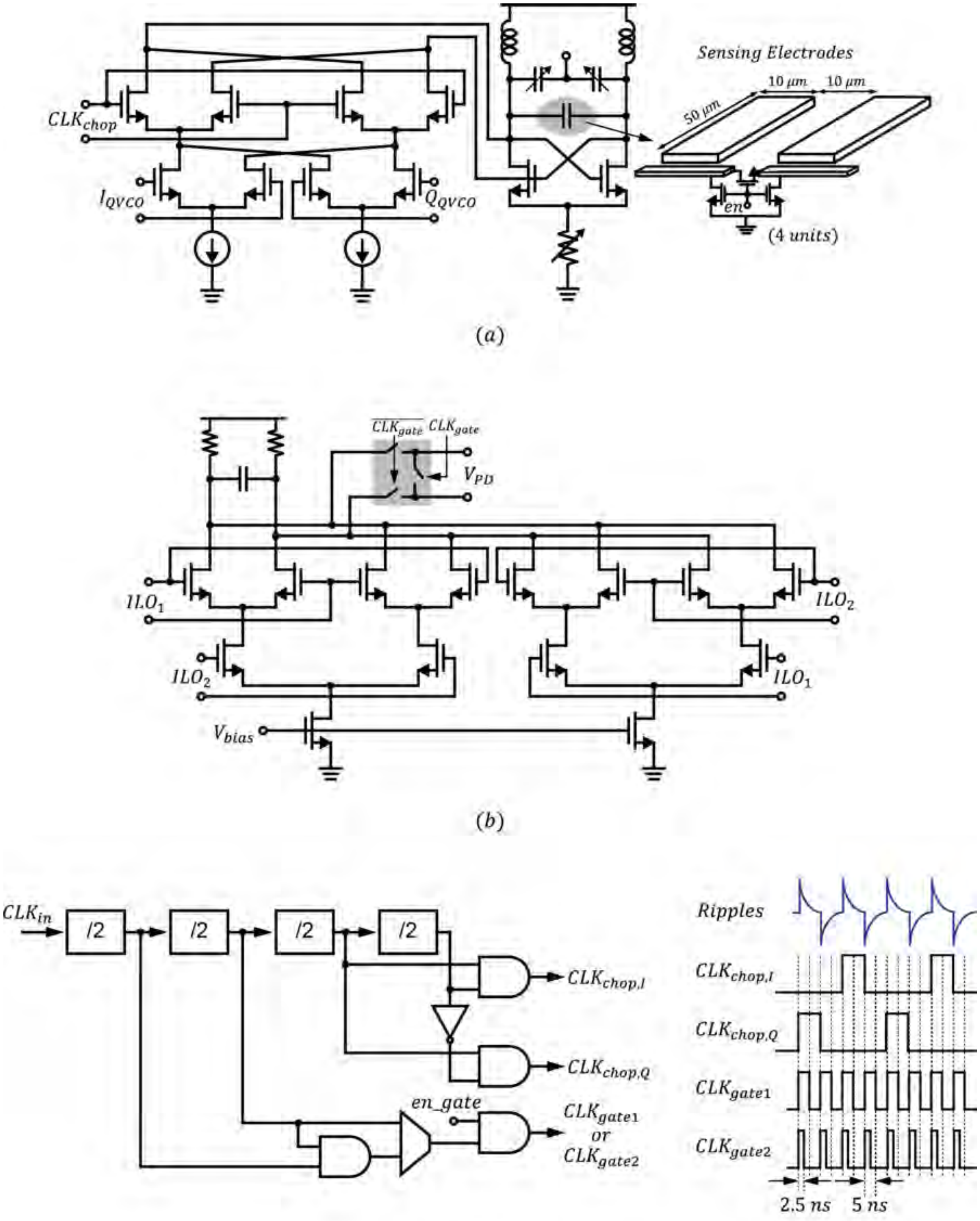

(a)

(b)

(c)

Figure 4.17: Circuit schematics: (a) injection-locked oscillator. (b) Phase detector. (c) Clock generation and the timing waveform.

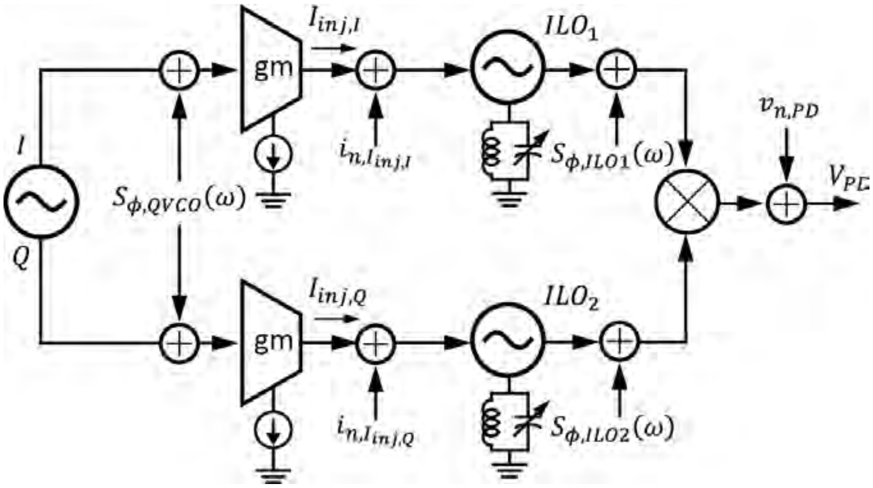

Figure 4.18: System noise model.

$$+S_{\phi,QVCO}(\omega)\cdot\left|H_{NTF,QVCO}(\omega)\right|^2. \tag{4.25}$$

In (4.25), $i_{n,\mathrm{Iinj}}(\omega)$ and K_{Iinj} represents the current noise and the corresponding phase sensitivity of I_{inj}, $H_{\mathrm{inj,LPF}}(\omega)$ is the input phase transfer function of ILO, and $S_{\phi,\mathrm{QVCO}}(\omega)$ and $H_{\mathrm{NTF,QVCO}}(\omega)$ are the QVCO phase noise and its noise transfer function. We will consider each of them separately.

The amplitude noise imposed on the injection current will *be* converted into phase modulation if the injection is off resonance ($\omega_{\mathrm{inj}} \neq \omega_0$), as shown in Fig. 4.19(a) and Fig. 4.19(b). The conversion gain is therefore a function of θ_{ss} and can be found with equation (4.6):

$$K_{I_{inj}}(\theta_{ss}) = \left|\frac{\partial\theta_{ss}}{\partial I_{inj}}\right| = \frac{\sin\theta_{ss}}{K+\cos\theta_{ss}}\cdot\frac{1}{I_{inj}} = F(\theta_{ss})\cdot\frac{1}{I_{inj}}. \tag{4.26}$$

The induced in-band phase noise at the output of the ILO is

$$S^2_{\phi,I_{inj}}(\omega) = F^2(\theta_{ss})\cdot\frac{i^2_{n,I_{inj}}(\omega)}{{I_{inj}}^2}. \tag{4.27}$$

To validate the model, the simulated $F(\theta_{\mathrm{ss}})$ are compared with the calculation in Fig. 4.19(c), and the result shows the expected noise increase with larger θ_{ss}. Nevertheless, the current noise of I_{inj} contributes 13 % even with $\theta_{\mathrm{ss}} = 60^{\circ}$ considering only the thermal noise at injection strength K of 0.4. However, simulation shows that the in-band noise (< 10 kHz offset) can be potentially dominated by the flicker noise of I_{inj} and hence resistive degeneration is applied to all the current sources.

The application of phase interpolation before the injection results in one additional level of noise conversion process. As shown in Fig. 4.19(d), amplitude noise on the tail

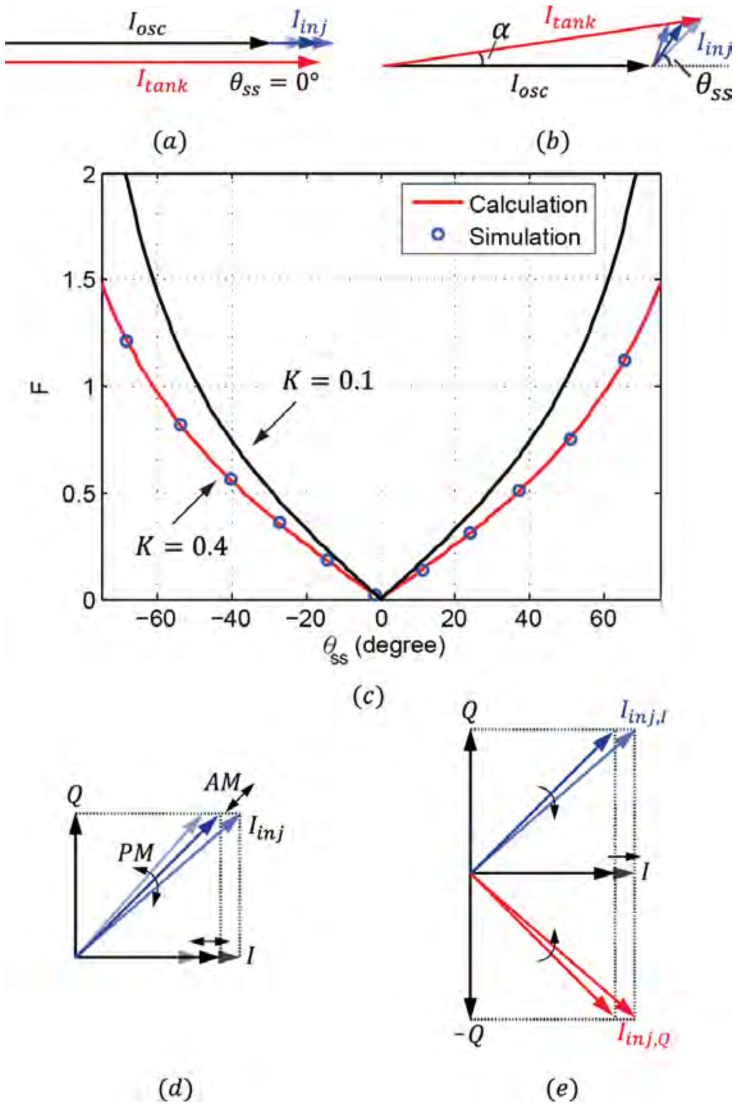

Figure 4.19: The effect of injection current AM noise.

current will incur both amplitude (AM) and phase modulation (PM) after the interpolation. The PM noise will directly appear at the output within the injection locking bandwidth while the AM noise is converted to phase fluctuation according to (4.26). Nevertheless, the overall noise contribution is similar to that without phase interpolation. Note that it is desirable to separate the tail currents for both summation and subtraction paths in order to avoid doubling the contribution due to noise correlation (Fig. 4.19(e)).

The noise arising from the QVCO leaks to the output if both paths are not perfectly matched. Fig. 4.20(a) depicts the noise model where the injection locking is described by two 1st-order low-pass filters $H_1(\omega)$ and $H_2(\omega)$. The noise appears at the output due to path mismatch is described by the transfer function:

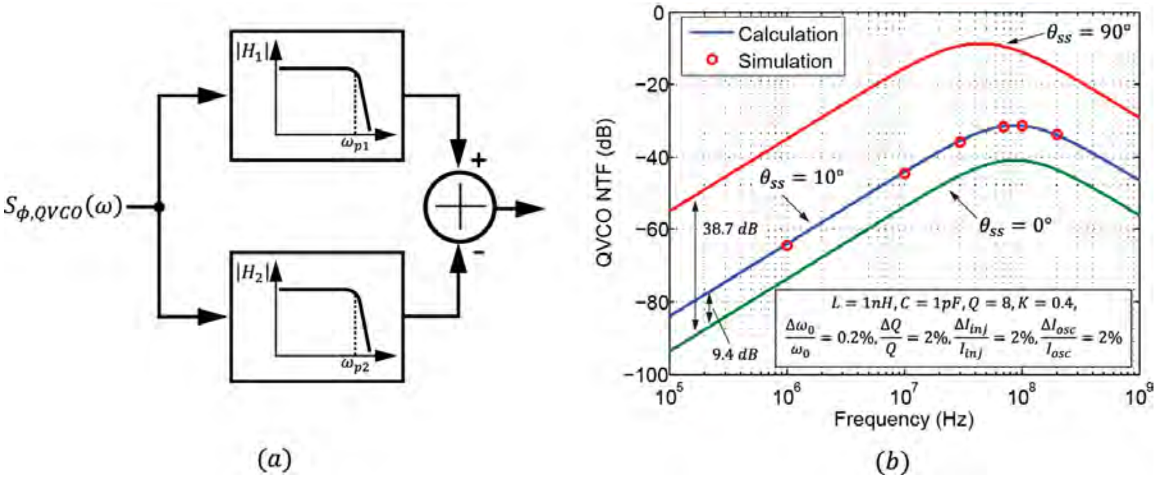

Figure 4.20: (a) Model for QVCO noise and (b) QVCO noise transfer function.

$$\left|H_{NTF,QVCO}(\omega)\right|^2 = |H_1(\omega) - H_2(\omega)|^2 = \left|\frac{1}{1 + j\dfrac{\omega}{\omega_{p1}}} - \frac{1}{1 + j\dfrac{\omega}{\omega_{p2}}}\right|^2, \tag{4.28}$$

where ω_{p1} and ω_{p2} represent the injection-locking bandwidth of each path, respectively. As signal bandwidth is much smaller than both ω_{p1} and ω_{p2}, (4.28) can be simplified to

$$\left|H_{NTF,QVCO}(\omega)\right|^2 \approx \omega^2 \frac{{\Delta\omega_p}^2}{{\omega_p}^4}. \tag{4.29}$$

Therefore, the amount of leakage can be determined by considering only the mismatch in the injection-locking bandwidth $\Delta\omega_p$ (= $\omega_{p1} - \omega_{p2}$). Such bandwidth mismatch arises from four parameters: ω_0, Q, I_{inj}, and I_{osc} according to (4.12), and can be derived with total derivatives shown in Section 4.6.3. The model is compared with the simulation in Fig. 4.20(b) with the given amount of mismatch shown in the inset. It is obvious that the rejection of QVCO noise is highly dependent on θ_{ss}. For simplicity, let's compare the case at θ_{ss} = 0° and 90° and the corresponding bandwidth mismatches are

$$\theta_{ss} = 0°\text{: } \Delta\omega_p = \omega_p \frac{\Delta\omega_0}{\omega_0} - \omega_p \frac{\Delta Q}{Q} + \frac{\omega_p}{(1+K)^2}\left(\frac{\Delta I_{inj}}{I_{inj}} - \frac{\Delta I_{osc}}{I_{osc}}\right), \tag{4.30}$$

$$\begin{aligned}\theta_{ss} = 90°\text{: } \Delta\omega_p &= \omega_p\left(1 + 2Q\frac{2K^2 - 1}{K^3}\right)\frac{\Delta\omega_0}{\omega_0} + \omega_p\left(\frac{K^2 - 1}{K^2}\right)\frac{\Delta Q}{Q} \\ &+ \omega_p \frac{1}{K^2}\left(\frac{\Delta I_{inj}}{I_{inj}} - \frac{\Delta I_{osc}}{I_{osc}}\right).\end{aligned} \tag{4.31}$$

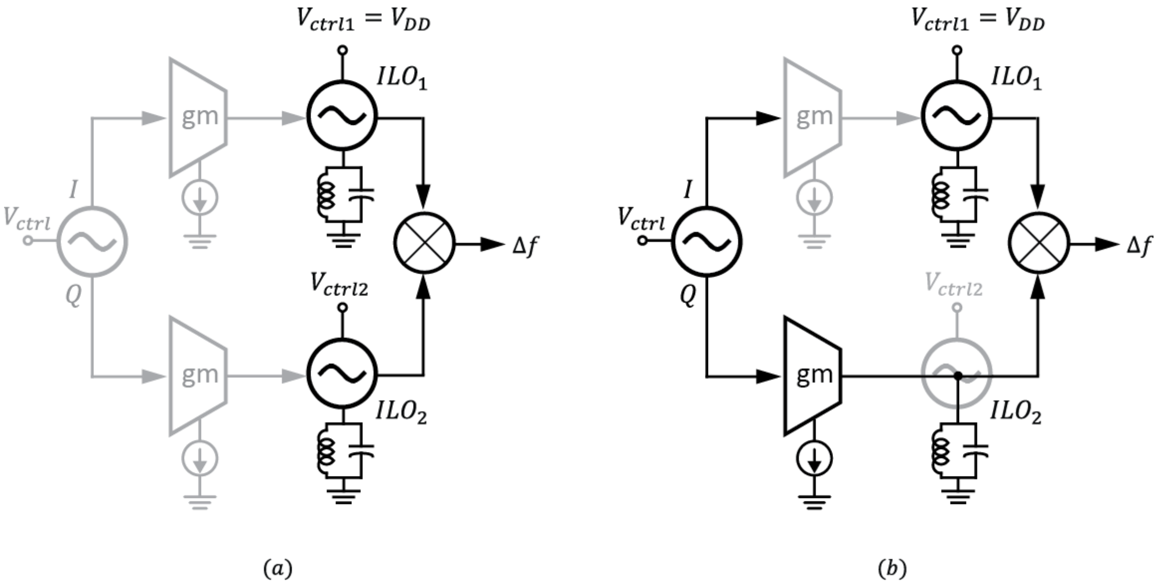

Figure 4.21: Frequency calibration between (a) ILOs and (b) QVCO and ILO.

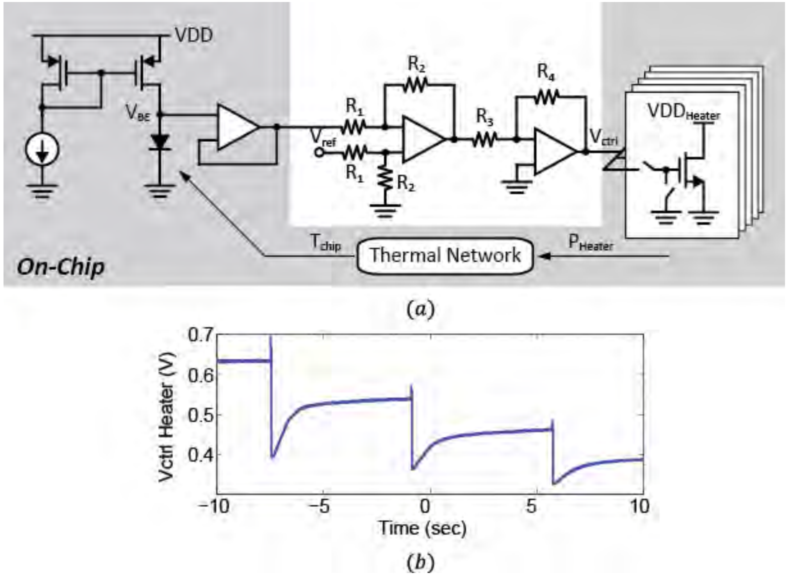

Figure 4.22: Temperature regulation: (a) schematics and (b) measured thermal time constant.

From the analysis, it is observed that injection at quadrature phase results in much higher sensitivity to mismatch compared to that of the in-phase injection. For example, the sensitivity to the oscillation frequency mismatch is increased by a factor of $2Q/K^3$. In this particular example, the difference can be as large as 38.7 dB, and therefore operating the sensor with on-resonance injection is recommended. Lastly, the noise contribution from QVCO leakage with the approximation in (4.29) can be calculated as

$$\phi^2_{n,rms,QVCO} \approx \int_0^\infty S_{\phi,QVCO}(\omega)\left(\frac{\omega}{\omega_p}\right)^2\left(\frac{\Delta\omega_p}{\omega_p}\right)^2 |H_{LPF}(\omega)|^2 d\omega. \qquad (4.32)$$

Assuming that QVCO has identical phase noise performance as the ILOs, the total noise contribution due to path mismatch is 0.15 % and 1 % for θ_{ss} of 10° and 60° according to the amount of mismatch shown in Fig. 4.20(b), respectively. Sensor performance against environmental drift and supply rejection can be analyzed in the same way if the oscillators do not track perfectly over PVT.

4.3.7 Calibration

Based on the aforementioned discussions, frequency calibration is necessary for optimum noise performance and is achieved by minimizing the frequency difference between each oscillator. As shown in Fig. 4.21, the calibration involves two steps by referencing both the oscillation frequency of QVCO and ILO_2 to that of ILO_1 through the measurement of the beat frequency. When calibrating the QVCO frequency, the ILO_2 oscillation is ceased and is configured as a LC-buffer. Due to close proximity in the layout, the two ILOs mutually lock if frequency deviation is less than 10 MHz. The calibration is therefore completed by placing the oscillators-to-be-calibrated at the center of the locking range

It is also essential to have a stable on-chip test structure in the dielectric (or capacitance) domain to facilitate gain calibration of each ILO. This is accomplished by implementing an array of four units on-chip switched capacitors made of metal overlapping (Fig. 4.17). Each unit presents approximately 20 aF of capacitance change based on the measurements. To mitigate sensor drift as well as the error induced by random mismatch, these test structures are clocked at 3 kHz during the measurements and the results are averaged.

4.3.8 Temperature Regulation and Thermal Effect

As dielectric relaxation is a strong function of molecular thermal energy, temperature regulation is implemented on-chip to avoid thermal interference. As shown in Fig. 4.22, PN junction diodes are used as V_{BE} temperature sensors and minimum-length NMOS transistors in linear region serve as heat actuators. The temperature is adjusted by controlling the gates of heaters, which are segmented to accommodate variation in the thermal network due to the custom microfluidic packaging. The stabilization loop is closed off-chip with loop gain of 66 and exhibits worst-case locking time of 4 sec when the medium is not in flow. The heater currents are supplied through an off-chip LDO.

As the ILO presents oscillation amplitude of less than 0.3 V, the power delivered to the medium is approximately 0.12 mW assuming the loss tangent of the medium is close to unity at frequency between 20 – 30 GHz. Hence microwave induced thermal effect on

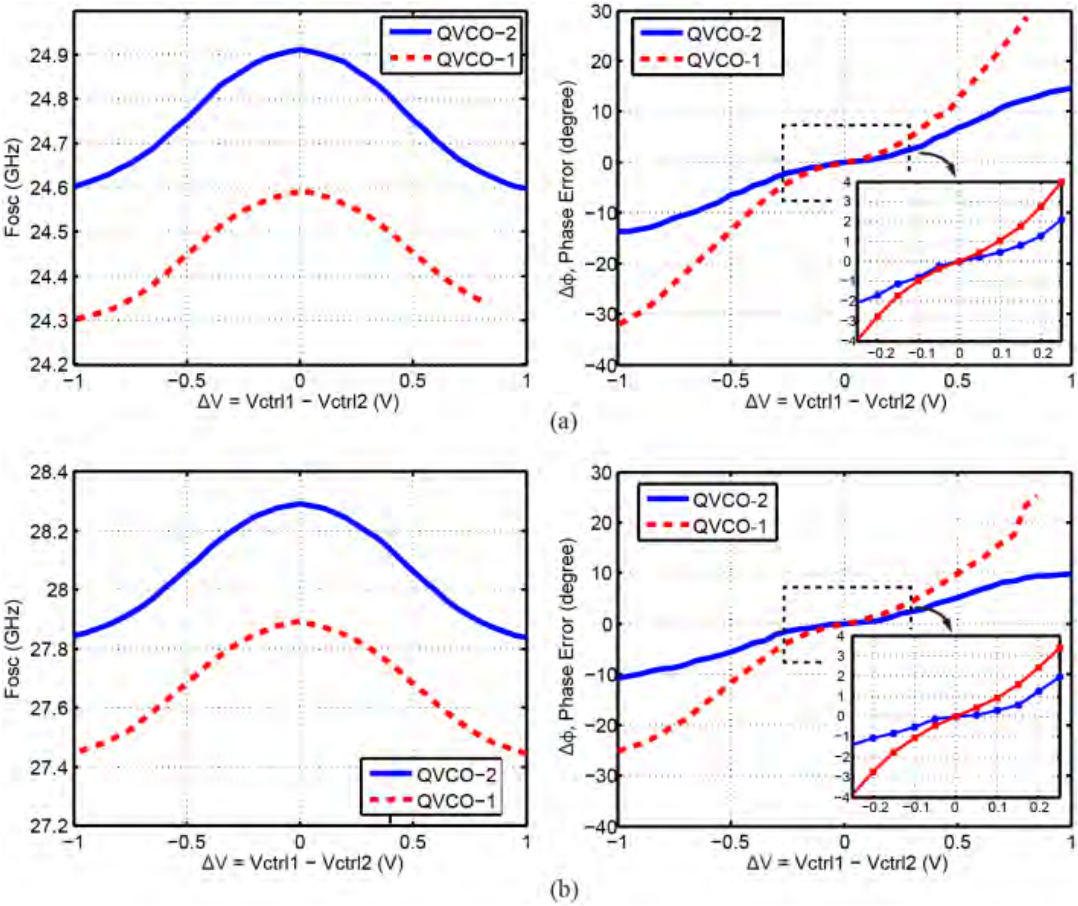

(a)

(b)

Figure 4.23: Measured frequency and phase error versus differential control voltage at two different bands ($\Delta V = 0$ at $V_{\text{ctrl}} = 1\text{V}$).

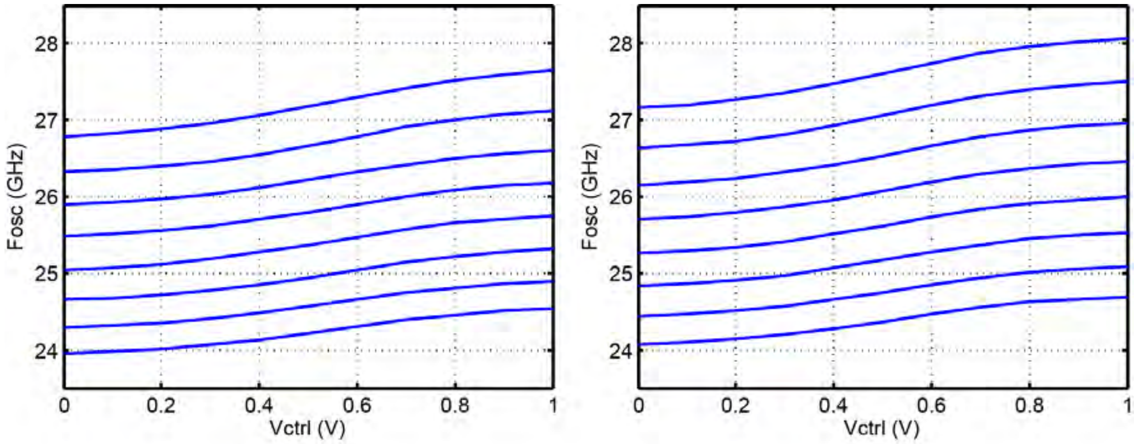

(a)

(b)

Figure 4.24: Frequency tuning curves for (a) QVCO-1 and (b) QVCO-2.

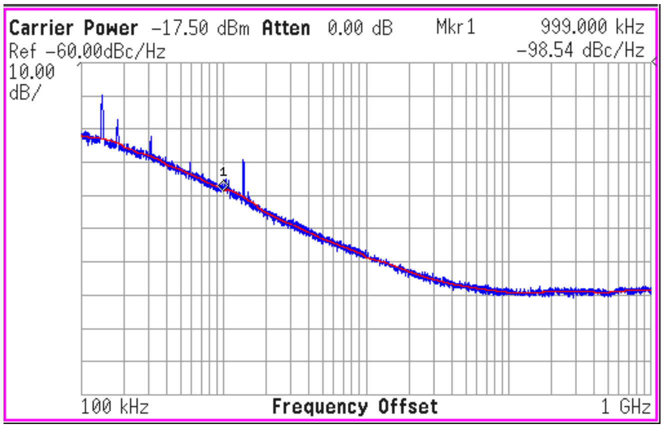

Figure 4.25: Measured QVCO-2 phase noise.

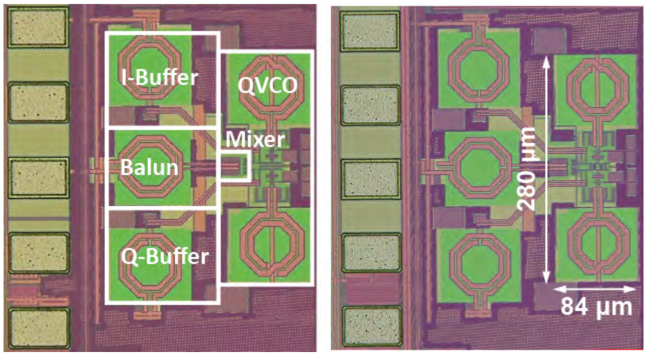

Figure 4.26: Die micrograph: (a) QVCO-1 and (b) QVCO-2.

Ref.	Freq (GHz)	Coupling Approach	DC Power (mW)	Phase Error (degree)	Phase Noise at 1MHz (dBc)	Tuning Range (%)	FOM (dB)	FOM$_A$** (dB)
[1]'13	5	Cascode Phase Shifter	4.2	0.6	-121	20.4	-189	-194.6
[2]'07	4.5	Linear Cap	3.2	~3*	-112	15.6	-181	-186.3
[3]'13	62.7	NMOS Diode	11.4	0.7	-94	16.8	-179.6	-193.7
[4]'13	6.6	MOS Varactors	16.8	0.3	-117	15.2	-180.8	-190.4
This Work	26	NMOS Diode	11.8	1.5	-100	14.4	-177.6	-193.9
	26	Bi-directional Diode	11.8	0.36	-98.5	15.4	-176.1	-192.4

*SSB rejection = 30 dB and assuming equal contribution from amplitude and phase errors. **FOM$_A$ = FOM-10log(Area(mm^2)) [4]

[1] Y.-C Lo and J. S.-Martinez, T-MTT'13. [2] C. T. Fu and H. C. Luong, ASSCC'07. [3] X. Yi, *et al*, ISSCC'13. [4] K. Bhardwaj, *et al*, VLSI'13.

Table 4.3: QVCO comparison table.

the physiological condition of cells can be neglected as the exposure of RF energy is less than 1 msec [22].

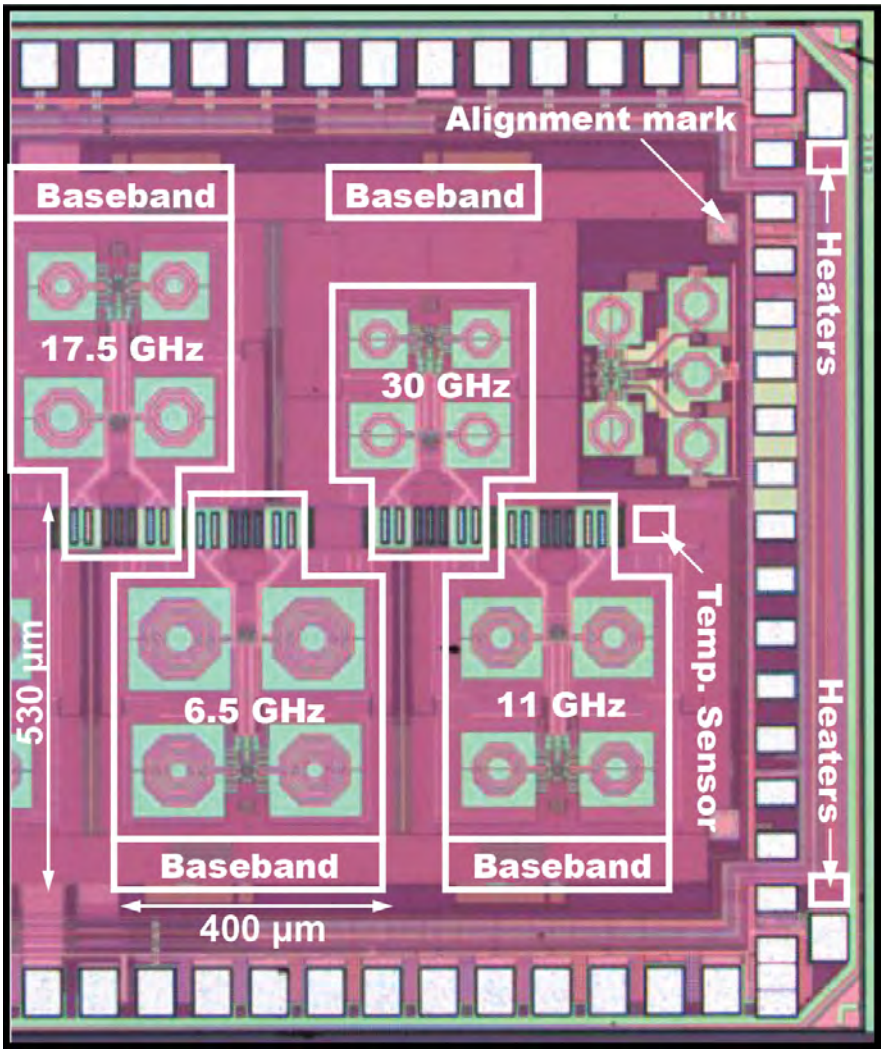

Figure 4.27: Chip micrograph.

4.4 Electrical Characterization

4.4.1 QVCO Measurements

The QVCOs are measured through on-wafer probing. I/Q outputs are buffered and converted through a balun-loaded amplifier. Phase error is measured with the aid of on-chip current-mode down-converting Gilbert mixer to a base- band frequency of 100 MHz and waveforms are captured using Agilent DSO6104A. To validate that QVCO-2 presents higher phase error immunity against tank mismatch, sensitivity measurement is carried out by offsetting the free-running frequencies of each oscillator with individually-accessible control voltages. With exactly the same measurement setup, the relative difference between the two architectures can be directly compared. Fig. 4.23 shows the phase error sensitivity and the oscillation frequency as a function of the differential control voltages at both the lowest and the highest frequency bands. All measured phase errors are normalized to that at $\Delta V = 0$. It is clearly seen that both QVCOs exhibit similar frequency dependency; on the other hand, QVCO-2 presents significantly lower phase error sensitivity. For example, the phase error sensitivity ($= \Delta\phi/\Delta V$) is reduced from 9.14°/V to 1.89°/V at highest frequency band, showing an improvement factor larger than 4. The measured absolute phase errors at $\Delta V = 0$ are 1.5° and 0.36° for QVCO-1 and QVCO-2, respectively, partially limited by routing and probe asymmetry. Fig. 4.24 shows the measured frequency tuning curves for both QVCOs. The PMOS devices shield the gate of the NMOS from the LC-tanks, and hence QVCO-2 exhibits higher oscillation frequency (28.07 vs. 27.65 GHz) and tuning range (4.0 vs. 3.7 GHz). Both QVCOs exhibit similar phase noise performance ranging from -98.5 to -100 dBc/Hz at 1-MHz offset (Fig. 4.25). Table 4.3 summarizes our study and compares it with recent works. Note that the measured phase noise is suboptimal due to lower tank Q-factor, limited by the available silicon area (Fig. 4.26); nonetheless, QVCO-1 achieves an $\mathrm{FOM_A}$ of -193.9 dB, comparable to state-of-the-art while QVCO-2 exhibits significantly improved phase accuracy.

4.4.2 Sensor Characterization

Fig. 4.27(a) shows the chip micrograph implemented in 65-nm CMOS. Each sensor occupies an area of $0.4\times0.46\ \mathrm{mm}^2$ consuming a total power of 65 mW under 1-V supply. While the temperature sensor is placed in proximity to the sensing electrodes underneath the microfluidic channel, two sets of heaters are located at the chip corners to provide more homogenous temperature distribution. Frequency scaling among each channel is achieved by scaling only the geometry of the spiral inductors in the oscillators. Fig. 4.28 shows the QVCO frequency tuning curves, exhibiting a tuning range of > 14.4 % for all channels. ILO locking range exceeds 2.5 % (in water) at nominal injection current setting ($K = 0.4$). By offsetting the ILO oscillation frequencies by 100 MHz, the phase noise of individual ILO is inferred by measuring the down-converted IF signal. The estimated ILO phase noise as the entire electrodes are immersed in water are -103.8 and -94 dBc/Hz at 1-MHz offset frequency for 6.5- and 30-GHz channels, respectively. It is approximately 1.5 ~ 3 dB better when loaded with air. The QVCO phase noise is -99 dBc/Hz at 1-MHz offset for the 30-GHz channel.

The sensor sensitivity is characterized by input-referring the sensor output to frequency shift through the use of $\mathrm{ILO_2}$ control voltage. First, the tuning range, the gain of $\mathrm{ILO_2}$ ($K_{\mathrm{ILO2}} = f_{\mathrm{osc,ILO2}}/V_{\mathrm{ctrl2}}$), and the sensor transducer gain A_{v} ($= V_{\mathrm{out}}/V_{\mathrm{ctrl2}}$) are measured separately. Next, the frequency sensitivity is derived by converting the measured output rms noise voltage through $K_{\mathrm{ILO}}/A_{\mathrm{v}}$:

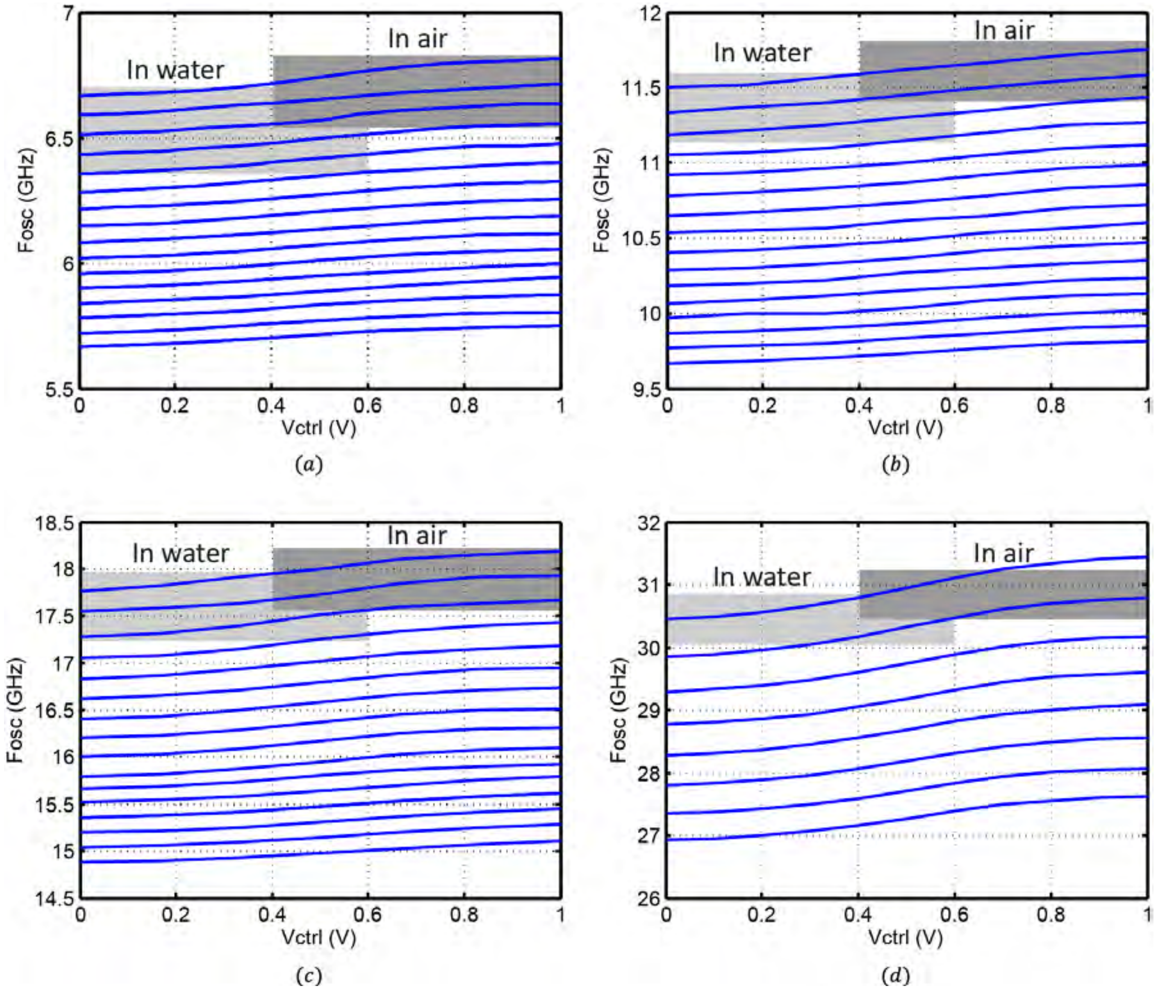

(a) (b) (c) (d)

Figure 4.28: QVCO tuning ranges for (a) 6.5-, (b) 11-, (c) 17.5-, and (d) 30-GHz channels.

$$\left(\frac{\Delta f}{f_0}\right)_{n,rms} = \frac{1}{f_0}\frac{v_{n,rms}}{A_v}K_{ILO2}, \tag{4.33}$$

where an example is shown in Fig. 4.29. The measured frequency resolution at 30-GHz channel is 5 ppm at 100-kHz filtering bandwidth at K = 0.4. The equivalent minimum detectable capacitance is therefore 10 ppm or 1.25 aF given the estimated ILO bulk capacitance of 125 fF when loaded fully with water. Such a number matches the SNR from modulating the on-chip switched-capacitors at 3 kHz measured with on-chip ΣΔ modulator (Fig. 4.30(a)). The PSD of such signal is also shown in Fig. 4.30(b), exhibiting a flicker noise corner of 10 kHz. Note that in the sensitivity measurement, the duration of data acquisition (or the observation window) is set to 4 msec, which effectively applies a high-pass filter with corner frequency of 125 Hz. In flow cytometry, such high-pass corner frequency depends on the flow rate of the cells when applying system-level

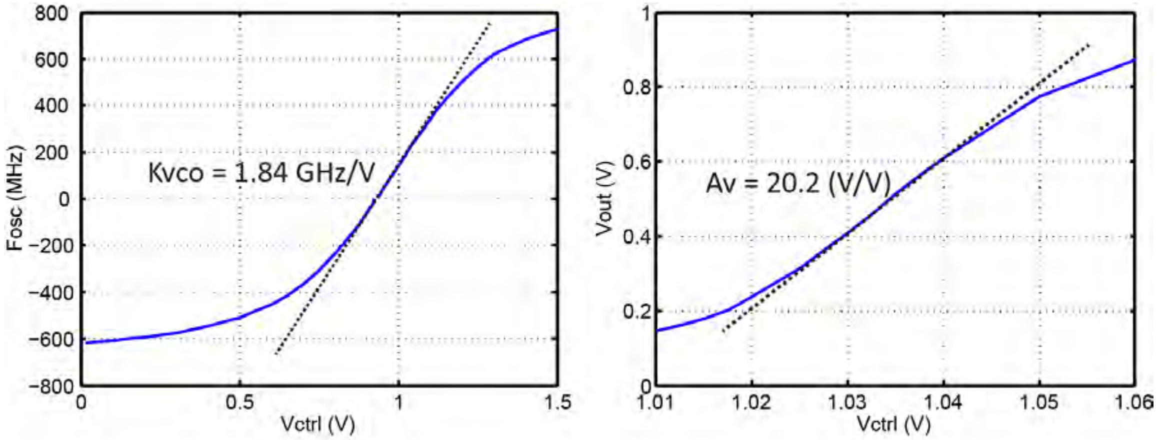

(*a*) (*b*)

Figure 4.29: Measured (a) ILO tuning range and (b) sensor transfer curve for 30-GHz channel.

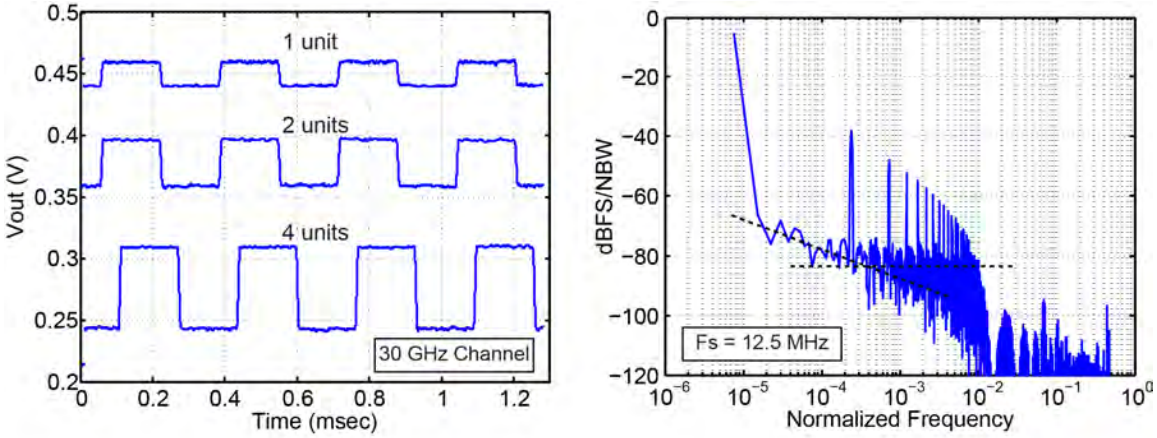

(*a*) (*b*)

Figure 4.30: Measured (a) timing waveforms of modulating on-chip switched-capacitors and (b) PSD after sinc2 filtering.

correlated double sampling (CDS) to the biploar waveform shown in Fig.4.2(a). Faster flow rate will results in better rejection against low-frequency noise. Finally, the signal is referred to the capacitance domain after ILO gain calibration using array of 20-aF switched capacitors.

Fig. 4.31(a) plots the sensor transfer curve from 30-GHz channel at different injection strength *K*, showing the expected transducer gain increment with weakened injection. The same figure also plots the transfer curve when the ILOs are configured as LC-buffers. Note that the gain compression is attributed to the output stage and such non-linearity can be compensated by simple curve-fitting curvature correction. At *K* = 0.4, a dynamic range of 52 dB (2000 ppm/5 ppm) is obtained. Fig. 4.31(b) plots the frequency resolution as a function of *K*, again from the 30-GHz channel. Contrary to the analysis in Section

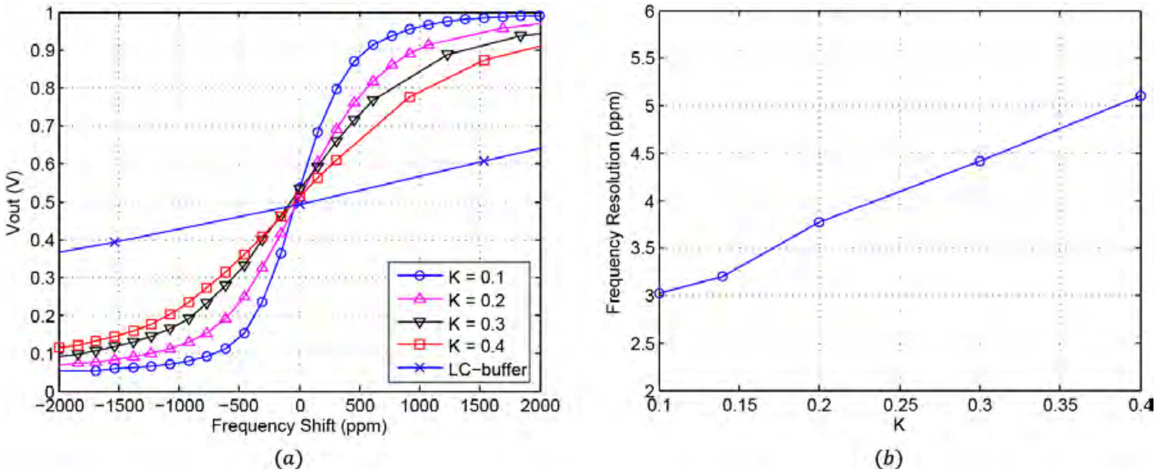

Figure 4.31: Measured (a) transfer curves and (b) frequency resolution at 30-GHz channel.

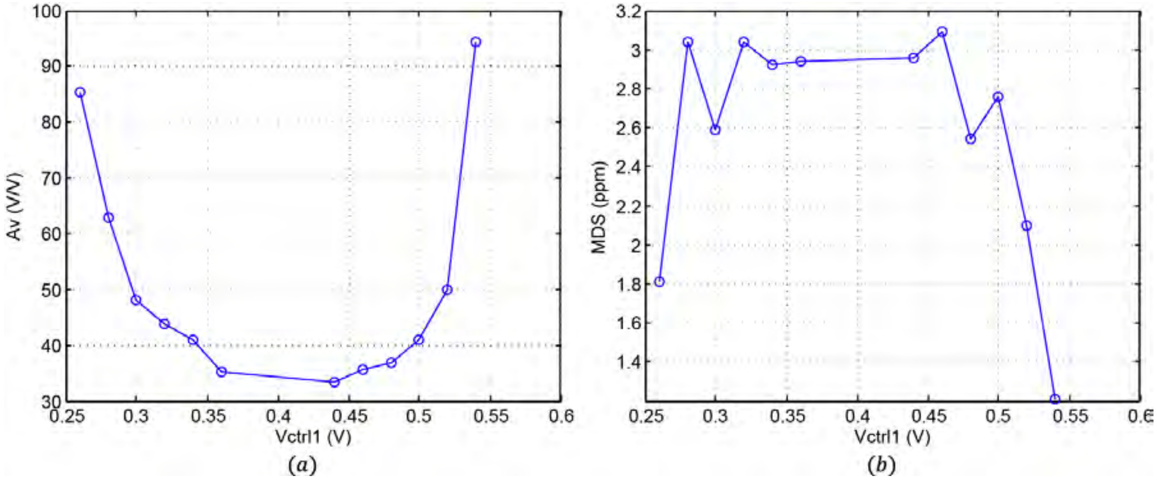

Figure 4.32: Measured (a) sensor sensitivity and (b) frequency resolution when adjusting V_{ctrl1}.

4.2.3, the input-referred frequency noise is improving with higher transducer gain. This is because system noise is dominated by PD and the baseband circuitries instead of the ILOs. Frequency resolution is improved to 3 ppm with $K = 0.1$.

Next, we study the sensor robustness against frequency mismatch between QVCO and ILOs. Fig. 4.32 plots the transducer gain A_{v} and the corresponding sensitivity limits as V_{ctrl} of QVCO is being adjusted. As expected, the gain increases when approaching the edge of locking range. Interestingly, the frequency noise improves with higher gain, as the noise is still dominated by the PD and the baseband circuits. The measured minimum detectable frequency shift is 1.25 ppm (also at 100-kHz bandwidth), equivalent to a minimum detectable capacitance change of 320 zF.

It is worth studying QVCO noise leakage due to path mismatch. Fig. 4.33 plots the frequency resolution as a function of the ratio between the two ILO injection currents.

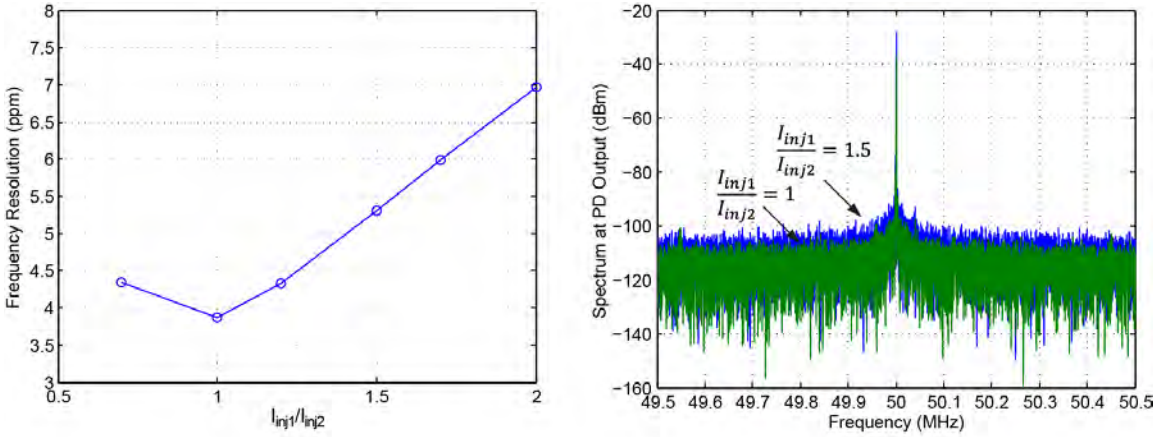

(a) (b)

Figure 4.33 Measured (a) frequency resolution and (b) PD noise floor with path mismatches.

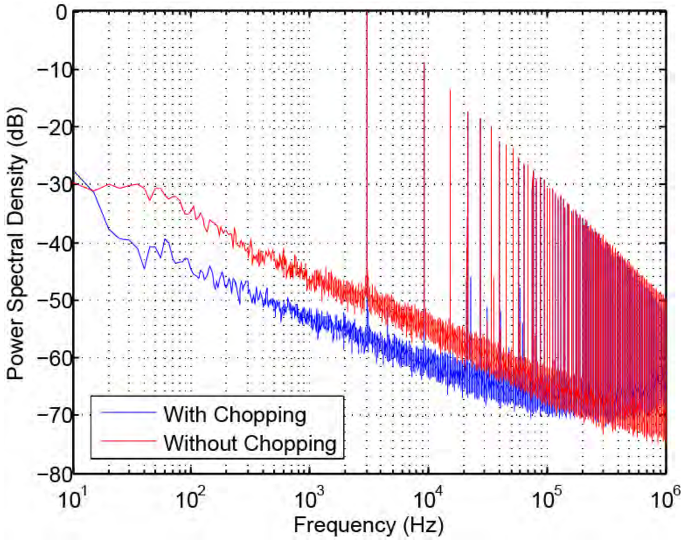

Figure 4.34: Measured output PSDs with and without chopping.

The rms noise increases by 2.5 % when the current ratio is 1.2, corresponding to a mismatch of 9.1 %. Such increase in the noise floor can also be observed from the measured spectrum at the PD output centered around the chopping frequency. The study emphasizes the importance of path matching.

The efficacy of chopping on flicker noise mitigation is shown in Fig. 4.34. Fig. 4.35 compares the chopping waveforms at the PD output. The nested chopping effect is clearly seen from the polarity of the ripples. Table 4.4 compares the input-referred chopping-induced offsets from different approaches. As there’s no precise on-chip phase reference, the offsets are calculated relative to that from the ping-pong nested chopping. The results show that such an input-referred offset can be as large as 761 ppm with BPSK chopping.

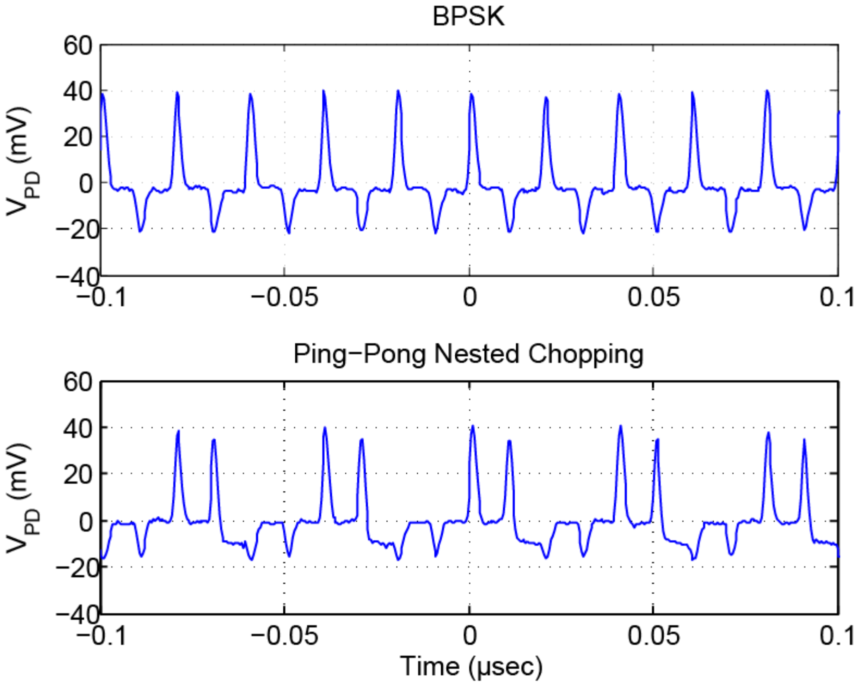

Figure 4.35: Measured chopping ripples at PD output.

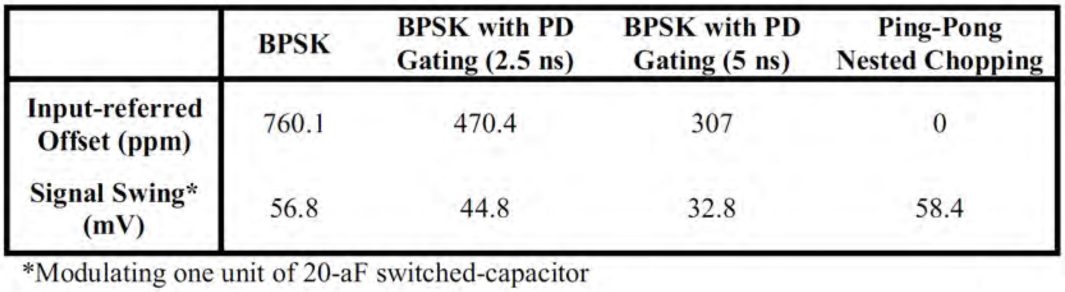

	BPSK	BPSK with PD Gating (2.5 ns)	BPSK with PD Gating (5 ns)	Ping-Pong Nested Chopping
Input-referred Offset (ppm)	760.1	470.4	307	0
Signal Swing* (mV)	56.8	44.8	32.8	58.4

*Modulating one unit of 20-aF switched-capacitor

Table 4.4: Comparison of input-referred frequency offsets between different approaches.

Ripple reduction through gating indeed reduces the offset at the cost of sacrificing the signal level.

4.5 Flow Cytometry Measurements

To ensure consistent elevation as cells flow across the sensing capacitors, microfluidics with 3D hydrodynamic focusing is necessary [91]. The focusing channel is patterned on top of the chip with 55 μm thick SU-8. After die mounting and wire bonding, a PDMS/glass microfluidic module is aligned and attached onto the chip under

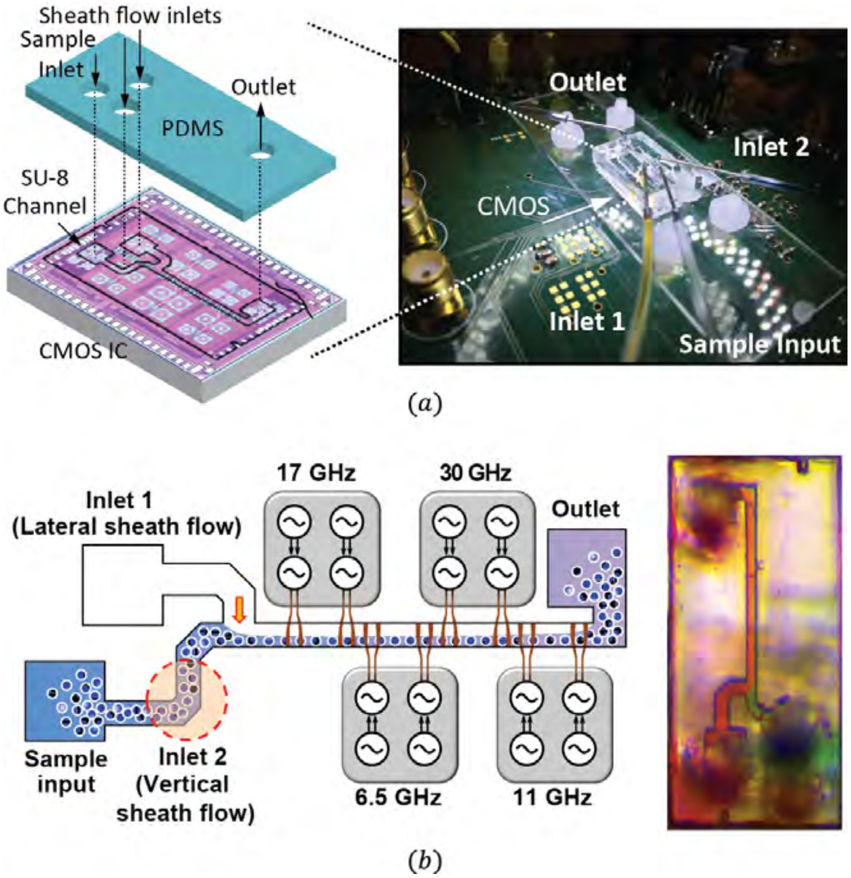

Figure 4.36: Microfluidic integration: (a) device photo and (b) 3-D hydrodynamic focusing.

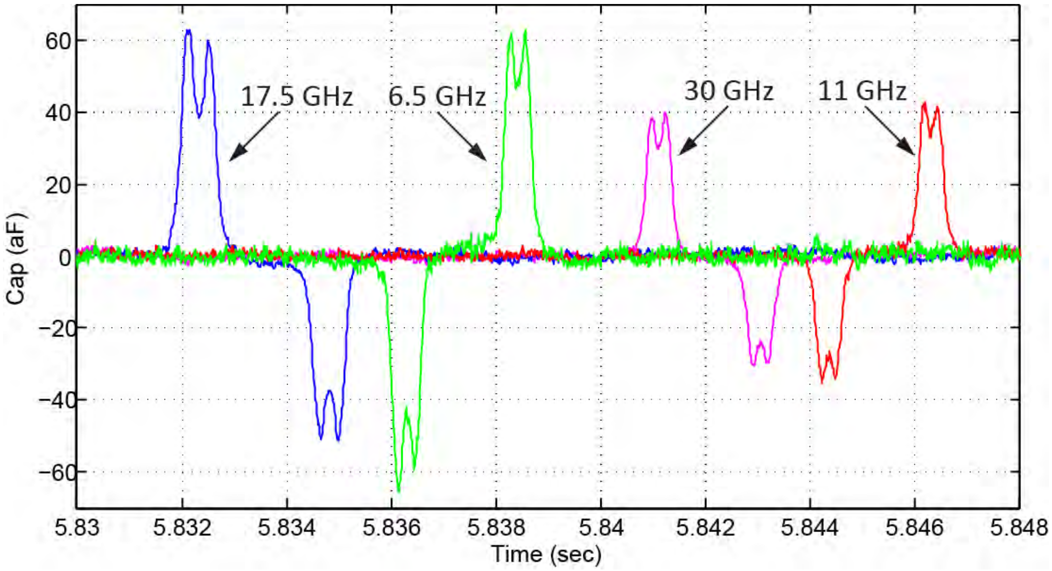

Figure 4.37: Measured single polystyrene bead flowing across four channels.

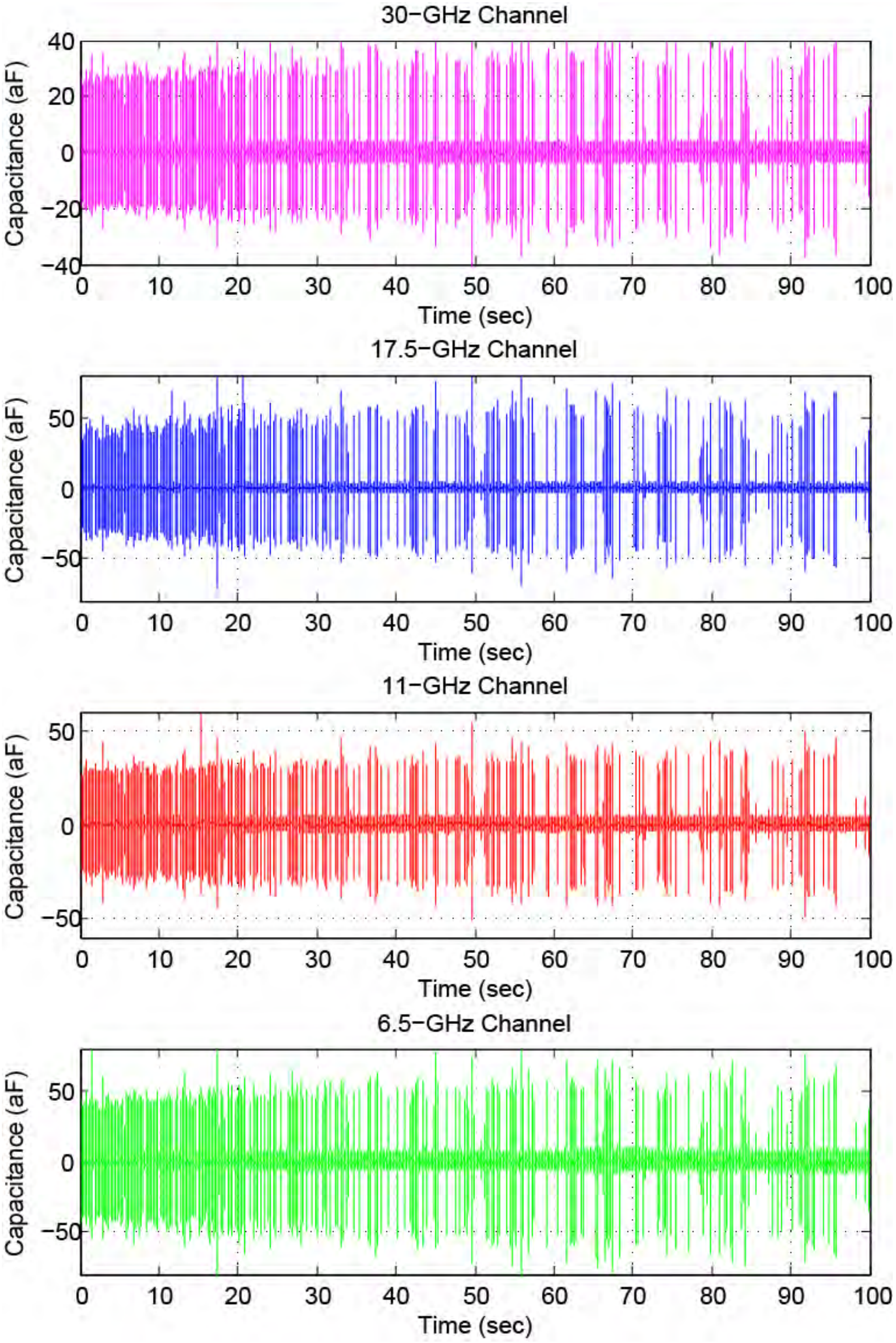

Figure 4.38: Measured bead signals.

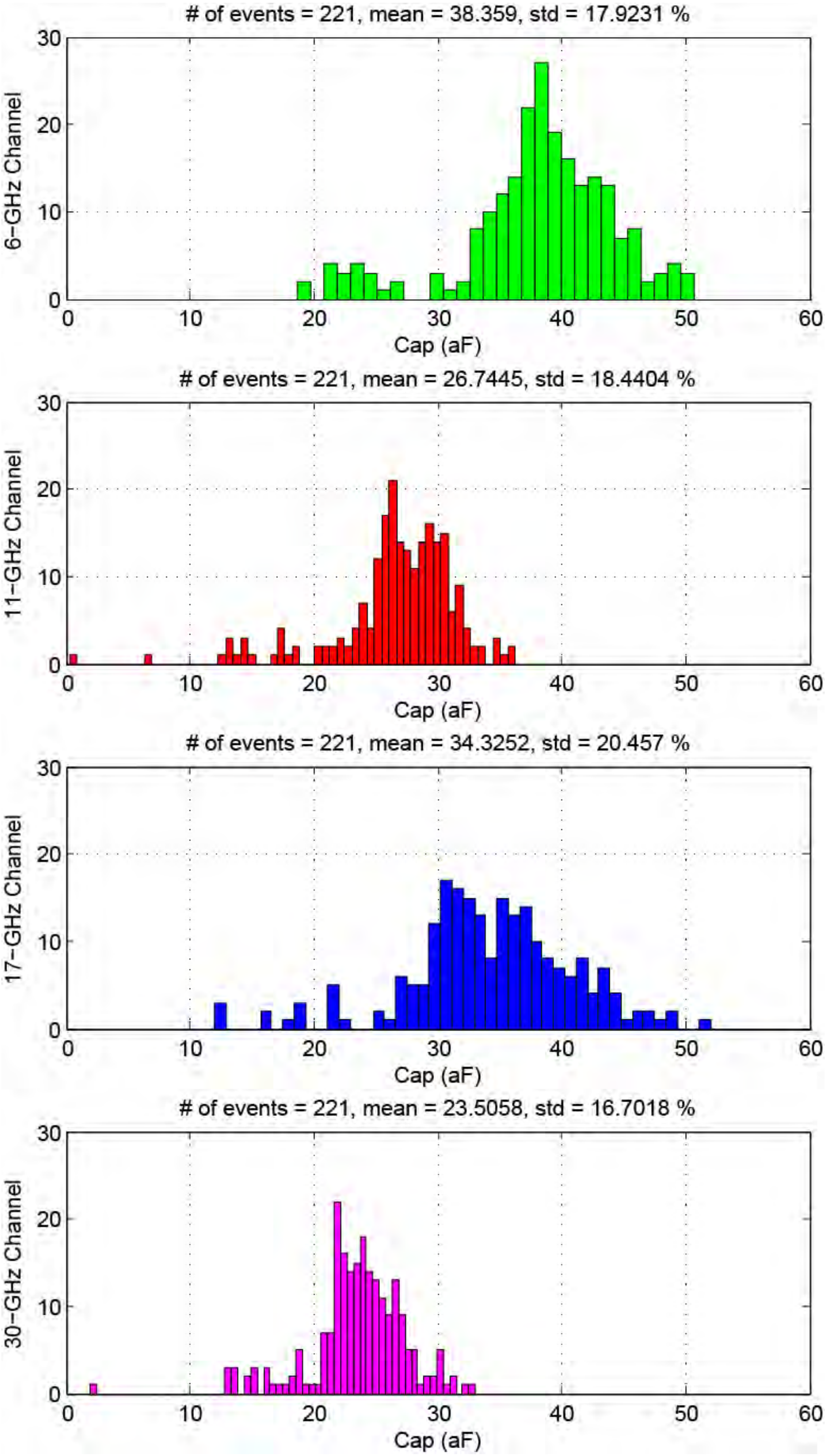

Figure 4.39: Histograms of the bead signals.

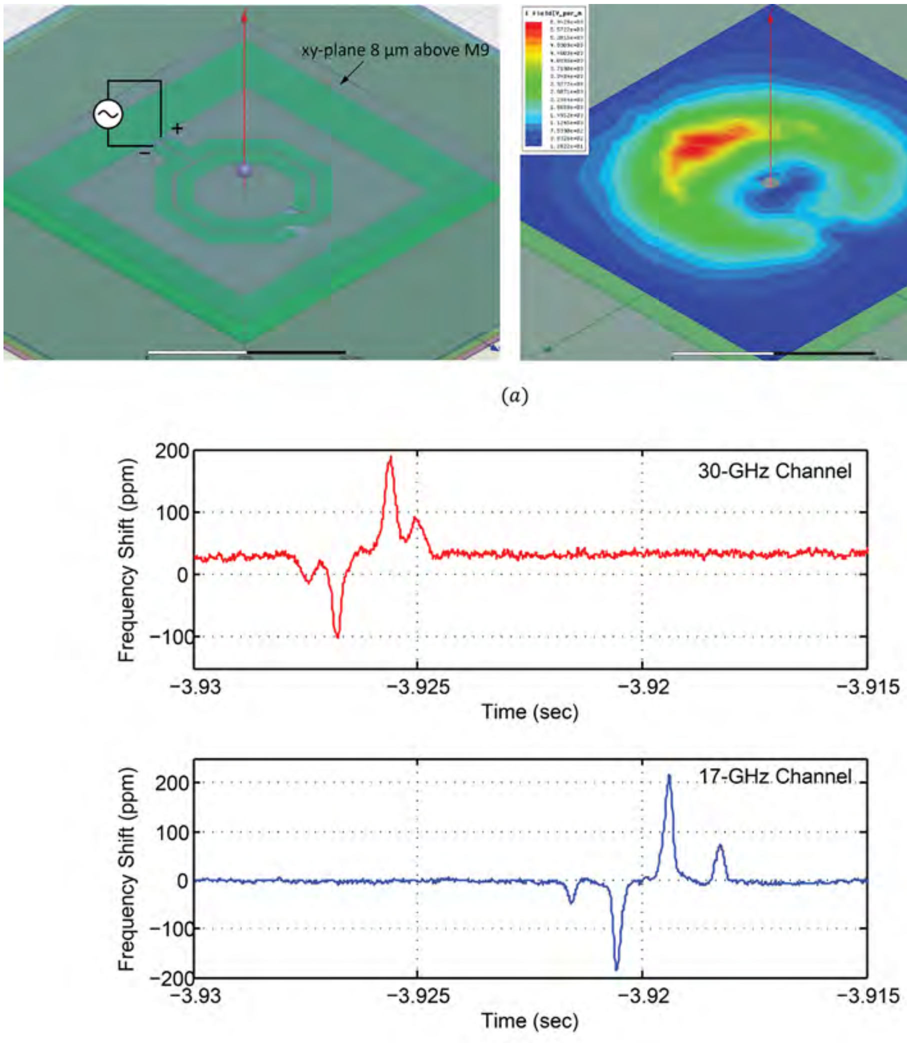

(*a*)

(*b*)

Figure 4.40: (a) Simulated E-fields on top of the 30-GHz spiral inductor. (b) Measured bead signals at 17.5- and 30-GHz channels.

microscope. Fig. 4.36 shows the entire measurement setup with focusing functionality demonstrated using different colors of ink.

Polystyrene beads (Polyscience Inc.) with a diameter of 5.8 μm (standard deviation of 0.447 μm) are distilled to 1.3 mg/ml using bovine serum albumin (BSA) for clogging prevention and injected using a syringe pump controlled at a rate of 160 mm/s. Fig. 4.37 shows the waveforms obtained from a 5.8 μm beads flowing across all four channels after ILO gain calibration. Fig. 4.38 shows the measured bead signals at high density over a duration of 100 s. The histogram shows that the coefficient of variation (CV) matches to that provided by the vendor (Fig. 4.39). Our flow cytometer can also differentiate between 5.8 and 10 μm beads in a mixture.

We have attempted to configure the system as a magnetic bead sensor similar to [40] and [93] by overlaying the fluidic channels on top of the spiral inductors of the two ILOs.

Interestingly, signals (Fig. 4.40) are observed at all frequencies with both magnetic (DyNA beads) and non-magnetic beads including polystyrene and gold particles. Field simulation shows that the differential center-tapped inductors can in fact be considered as two large co-planar electrodes. Fig. 4.40(a) shows the fringing fields above the inductor when driven differentially with 1-V amplitude, showing field intensity on the order of 0.6×10^4 V/m even at an distance 8 μm above M9 including CMOS passivation unremoved. Beads-induced capacitance change can therefore still be detected on top of the spiral inductors. Such a conclusion is different from [78]. Unfortunately, no magnetic response has been observed. This could be due to too high of an excitation frequency as the susceptibility of magnetic materials tends to vanish at frequencies above 6 GHz according to [92].

4.6 Discussions

4.6.1 Sensitivity Limits

This works presents an interferometry-based architecture employing injection-locked oscillator sensors for high-throughput flow cytometry using dielectric spectroscopy at microwave frequencies. Benefiting from the inherent phase amplification property of ILO sensors and simultaneous operation of both the sensing and the reference oscillators, the highest possible rejection against undesirable noise sources is obtained. A minimum detectable frequency shift of 1.25 ppm is measured with 100-kHz filtering bandwidth at 30 GHz, approaching the intrinsic noise floor of the sensing oscillator. In theory, the frequency resolution is 0.296 ppm if only the noise of the two ILOs is being considered assuming that each bears phase noise of -94 dBc/Hz at 1-MHz offset. Therefore the proposed sensor architecture measures noise that is 4.2 times the theoretical limit considering only the thermal noise of the oscillators. As a comparison, state-of-the-art oscillator-based reactance sensor with frequency counting measurements [93] achieves thermal-noise-limited frequency resolution of 0.125 ppm in 5 ms of counting period from a 1-GHz oscillator with phase noise performance of -135.3 dBc/Hz at 1-MHz offset, resulting in an estimate frequency resolution of 2.8 ppm ($= 0.125\ \text{ppm}\times\sqrt{(100\text{k}\times5\text{m})}$) after up-scaling the bandwidth. The case is worst once the uncertainty of counting window has been taken into account. This concludes the advantage of injection-locking for high-speed sensing applications. On the other hand, the relatively high flicker noise corner frequency, which originates from the ILO itself, limits the resolution at low filtering bandwidth. Approaches to reject low frequency noise require further research. Lastly, it is important to point out the ILOs in this work are not designed for low phase noise. In fact, minimum tank capacitance is pursued to minimize signal degradation in the capacitive sensing. The estimated water-loaded tank-Q is 3.5 from HFSS and the post-layout extraction at 30 GHz. Table 4.5 compares with previous work on oscillator-based sensors and impedance analyzers.

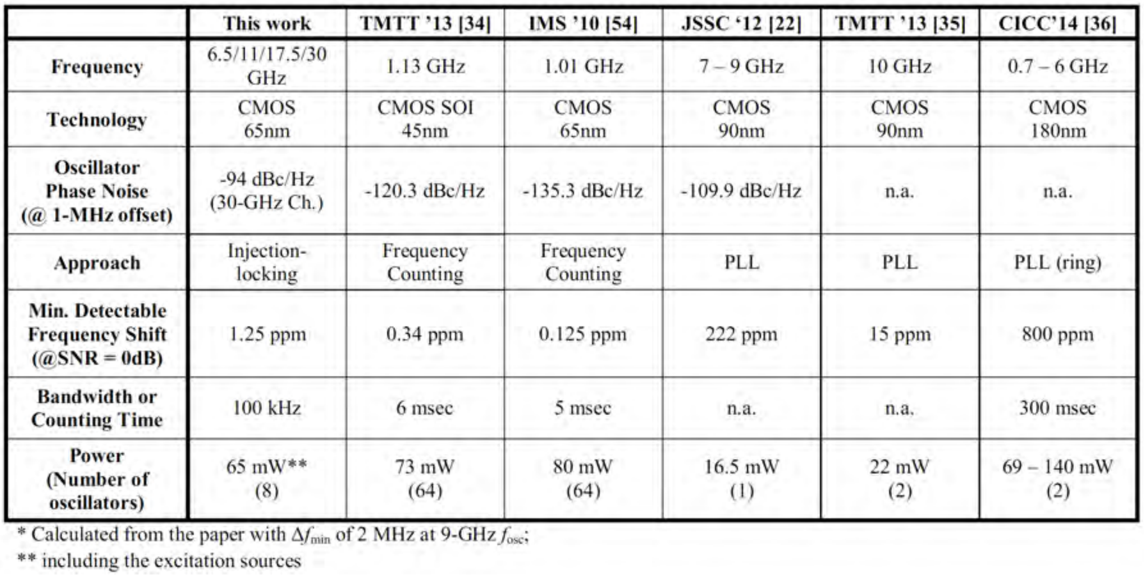

	This work	TMTT '13 [34]	IMS '10 [54]	JSSC '12 [22]	TMTT '13 [35]	CICC'14 [36]
Frequency	6.5/11/17.5/30 GHz	1.13 GHz	1.01 GHz	7 – 9 GHz	10 GHz	0.7 – 6 GHz
Technology	CMOS 65nm	CMOS SOI 45nm	CMOS 65nm	CMOS 90nm	CMOS 90nm	CMOS 180nm
Oscillator Phase Noise (@ 1-MHz offset)	-94 dBc/Hz (30-GHz Ch.)	-120.3 dBc/Hz	-135.3 dBc/Hz	-109.9 dBc/Hz	n.a.	n.a.
Approach	Injection-locking	Frequency Counting	Frequency Counting	PLL	PLL	PLL (ring)
Min. Detectable Frequency Shift (@SNR = 0dB)	1.25 ppm	0.34 ppm	0.125 ppm	222 ppm	15 ppm	800 ppm
Bandwidth or Counting Time	100 kHz	6 msec	5 msec	n.a.	n.a.	300 msec
Power (Number of oscillators)	65 mW** (8)	73 mW (64)	80 mW (64)	16.5 mW (1)	22 mW (2)	69 – 140 mW (2)

* Calculated from the paper with Δf_{min} of 2 MHz at 9-GHz f_{osc};

** including the excitation sources

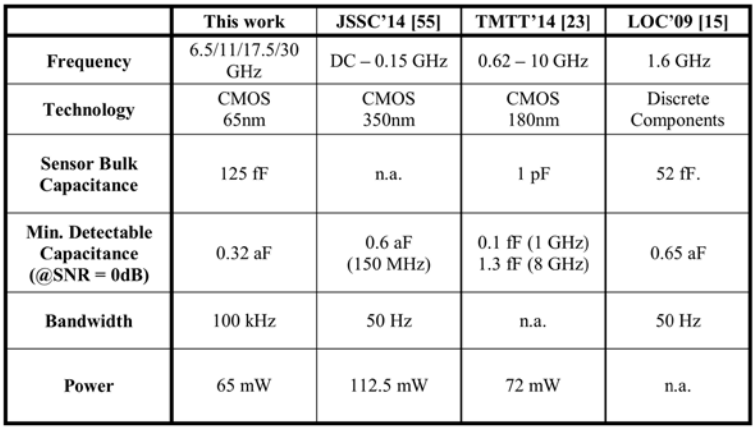

	This work	JSSC'14 [55]	TMTT'14 [23]	LOC'09 [15]
Frequency	6.5/11/17.5/30 GHz	DC – 0.15 GHz	0.62 – 10 GHz	1.6 GHz
Technology	CMOS 65nm	CMOS 350nm	CMOS 180nm	Discrete Components
Sensor Bulk Capacitance	125 fF	n.a.	1 pF	52 fF.
Min. Detectable Capacitance (@SNR = 0dB)	0.32 aF	0.6 aF (150 MHz)	0.1 fF (1 GHz) 1.3 fF (8 GHz)	0.65 aF
Bandwidth	100 kHz	50 Hz	n.a.	50 Hz
Power	65 mW	112.5 mW	72 mW	n.a.

Table 4.5: Comparison with oscillator-based reactance sensors and impedance analyzers.

4.6.2 Mutually-locked Coupled Oscillators

In this appendix, we will show that the frequency shift SNR of two mutually locked oscillators is no different from having two independent ILOs embedded in an interferometry. Fig. 4.41 shows the schematic of the coupled oscillators and its equivalent circuit model. To simplify the analysis, we consider only the in-phase coupling and therefore both V_{out1} and V_{out2} are perfectly synchronized with zero degree phase difference if $\omega_{\text{osc1}} = \omega_{\text{osc2}}$. The SNR is defined as the ratio between output phase shift due to frequency perturbation and its corresponding phase noise.

First, we will derive the output phase shift as ω_{osc1} is being perturbed by $\Delta\omega$. The Generalized Adler's Equations of the system are

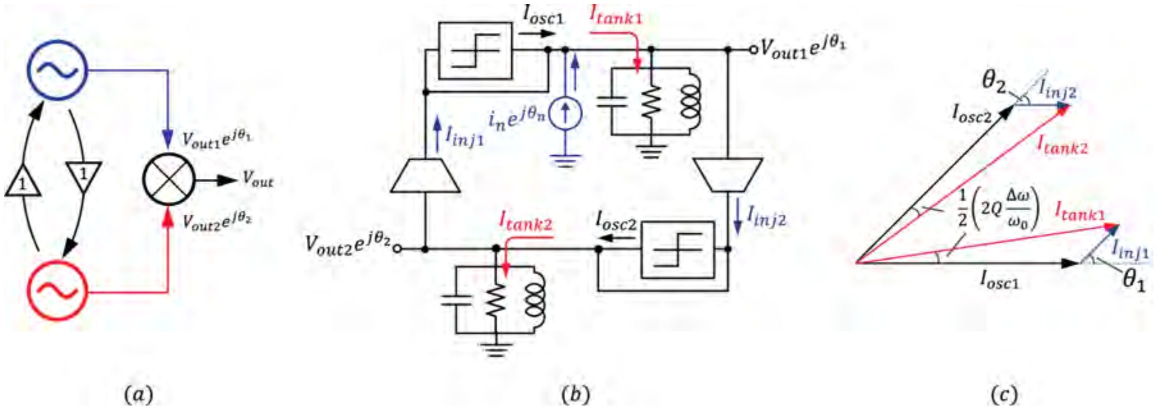

Figure 4.41: Mutually-locked oscillator sensor. (a) Circuit schematic. (b) Equivalent model. (c) Steady-state phasor diagram.

$$\frac{d\theta_1}{dt} = \omega_{osc1} + \frac{\omega_{osc1}}{2Q}\frac{I_{inj}\,sin(\theta_2 - \theta_1)}{I_{osc} + I_{inj}\,cos(\theta_2 - \theta_1)}, \tag{4.34}$$

$$\frac{d\theta_2}{dt} = \omega_{osc2} + \frac{\omega_{osc2}}{2Q}\frac{I_{inj}\,sin(\theta_1 - \theta_2)}{I_{osc} + I_{inj}\,cos(\theta_1 - \theta_2)}. \tag{4.35}$$

With $\omega_{osc1} = \omega_0 + \Delta\omega$, $\omega_{osc2} = \omega_0$, the system will settle to a new oscillation frequency ω_{osc}, and hence $\theta_1 = \omega_{osc}t + \theta_{ss}$, $\theta_2 = \omega_{osc}t$. Inserting in into (4.34) and (4.35), we arrive at the following expressions:

$$\frac{K\,sin\,\theta_{ss}}{1 + K\,cos\,\theta_{ss}} = \frac{1}{2}\frac{1}{1 + \frac{1}{2}\frac{\Delta\omega}{\omega_0}}2Q\frac{\Delta\omega}{\omega_0} \approx \frac{1}{2}\left(2Q\frac{\Delta\omega}{\omega_0}\right), \tag{4.36}$$

while ω_{osc} simply equals to the average of ω_{osc1} and ω_{osc2}:

$$\omega_{osc} = \omega_0 + \frac{\Delta\omega}{2}. \tag{4.37}$$

The effective frequency shift is therefore halved. Fig. 4.41(c) shows the corresponding phase diagram.

Next, we study the phase noise appears at the difference output ($\theta_1 - \theta_2$). By injecting a sinusoidal noise current into OSC$_1$ at the frequency of $\omega_0 + \omega_m$, the Generalized Adler Equations are [84]

$$\frac{d\theta_1}{dt} = \omega_0 + \frac{\omega_0}{2Q}\frac{I_{inj}\,sin(\theta_2 - \theta_1) + i_n\,sin(\theta_n - \theta_1)}{I_{osc} + I_{inj}\,cos(\theta_2 - \theta_1) + i_n\,cos(\theta_n - \theta_1)}, \tag{4.38}$$

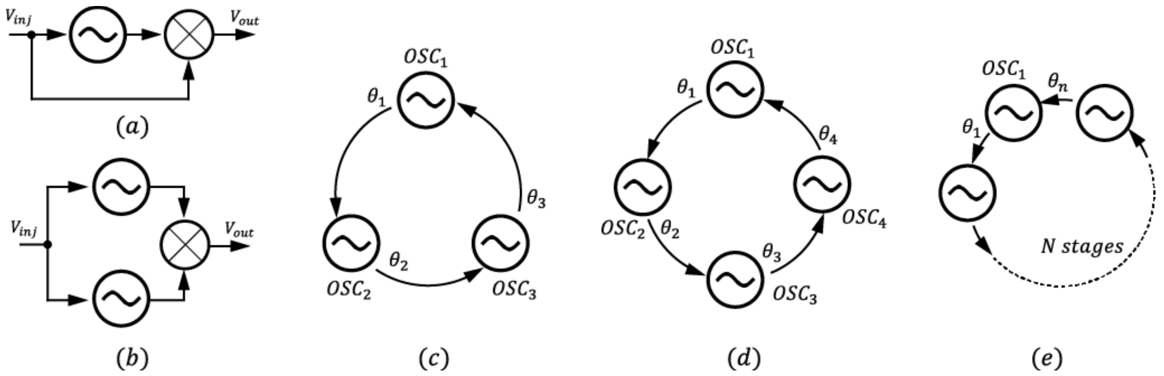

Figure 4.42: Injection-locked oscillator topologies. (a) Single ILO. (b) Interferometry. (c) 3-stage coupled oscillator. (d) 4-stage coupled oscillators. (e) N-stage coupled oscillator.

$$\frac{d\theta_2}{dt} = \omega_0 + \frac{\omega_0}{2Q}\frac{I_{inj}\,sin(\theta_1 - \theta_2)}{I_{osc} + I_{inj}\,cos(\theta_1 - \theta_2)}, \tag{4.39}$$

where i_n represents the noise amplitude. With $\theta_1 = \omega_0 t + \hat{\theta}_1$, $\theta_2 = \omega_0 t + \hat{\theta}_2$, $\theta_n = (\omega_0 + \omega_m)t$, and small number approximation ($|\hat{\theta}_1|$, $|\hat{\theta}_2|$, and i_n/I_{osc} << 1), (4.38) is expressed as

$$\frac{d\hat{\theta}_1}{dt} \approx \frac{\omega_0}{2Q}\frac{K\,sin(\hat{\theta}_2 - \hat{\theta}_1)}{1 + K\,cos(\hat{\theta}_2 - \hat{\theta}_1)}\left(1 + \frac{i_n}{I_{osc}}\frac{1}{K\,sin(\hat{\theta}_2 - \hat{\theta}_1)}sin(\omega_m t)\right)$$

$$\cdot\left(1 - \frac{i_n}{I_{osc}}\frac{1}{1 + K\,cos(\hat{\theta}_2 - \hat{\theta}_1)}cos(\omega_m t)\right). \tag{4.40}$$

After applying Taylor series expansion with respect to $\hat{\theta}_2 - \hat{\theta}_1$, we arrive at

$$\frac{d\hat{\theta}_1}{dt} \approx \frac{\omega_0}{2Q}\frac{K}{1 + K}(\hat{\theta}_2 - \hat{\theta}_1) + \frac{\omega_0}{2Q}\frac{i_n}{I_{osc}}\frac{1}{1 + K}sin\,\omega_m t. \tag{4.41}$$

In the same way, (4.39) is derived as

$$\frac{d\hat{\theta}_2}{dt} \approx \frac{\omega_0}{2Q}\frac{K}{1 + K}(\hat{\theta}_1 - \hat{\theta}_2) = \omega_p(\hat{\theta}_1 - \hat{\theta}_2). \tag{4.42}$$

Merging (4.41) and (4.42) results in the following differential equation:

$$\frac{d(\hat{\theta}_1 - \hat{\theta}_2),}{dt} \approx -2\omega_p(\hat{\theta}_1 - \hat{\theta}_2) + \frac{i_n}{I_{osc}}\frac{1}{K}\omega_p\,sin\,\omega_m t. \tag{4.43}$$

(4.43) is solved by assuming $\hat{\theta}_1 - \hat{\theta}_2$ has the form of $A\, sin\, \omega_m\, t + B\, cos\, \omega_m t$:

$$\hat{\theta}_1 - \hat{\theta}_2 = \frac{1}{2}\frac{1}{K}\frac{1}{1+\left(\frac{\omega_m}{2\omega_p}\right)^2}\frac{i_n}{I_{osc}}\left(sin\, \omega_m t - \frac{1}{2}\frac{\omega_m}{\omega_p} cos\, \omega_m t\right). \tag{4.44}$$

With $\omega_m << \omega_p$,

$$\hat{\theta}_1 - \hat{\theta}_2 \approx \frac{1}{2}\frac{1}{K}\frac{i_n}{I_{osc}} sin\, \omega_m t. \tag{4.45}$$

The above expression is free of ω_m due to the difference operation. The same approach is applied to a single ILO sensor (Fig. 4.42(a)), leading to

$$\hat{\theta} \approx \frac{1}{K}\frac{i_n}{I_{osc}} sin\, \omega_m t. \tag{4.46}$$

Comparing (4.45) and (4.46), it is seen that the amount of phase perturbation from the pulling of a noise current is reduced by half.

Defining the SNR of a single ILO (Fig. 4.42(a)) as

$$SNR_0 = \frac{\left(\frac{\Delta\omega}{\omega_0} S\right)^2}{\phi_n^2}, \tag{4.47}$$

with S and ϕ_n^2 representing the frequency-to-phase conversion and the integrated phase noise of the ILO, respectively, and assuming all the oscillators have identical noise floor, the SNR of two mutually locked oscillators is

$$SNR_2 = \frac{\left(\frac{1}{2}\frac{\Delta\omega}{\omega_0} S\right)^2}{2\left(\frac{\phi_n}{2}\right)^2} = \frac{1}{2} SNR_0. \tag{4.48}$$

The SNR of two independent ILOs in an interferometry (Fig. 4.42(b)) is

$$SNR_1 = \frac{\left(\frac{\Delta\omega}{\omega_0} S\right)^2}{2\phi_n^2} = \frac{1}{2} SNR_0. \tag{4.49}$$

Therefore, there’s no performance improvement with two coupled oscillators.

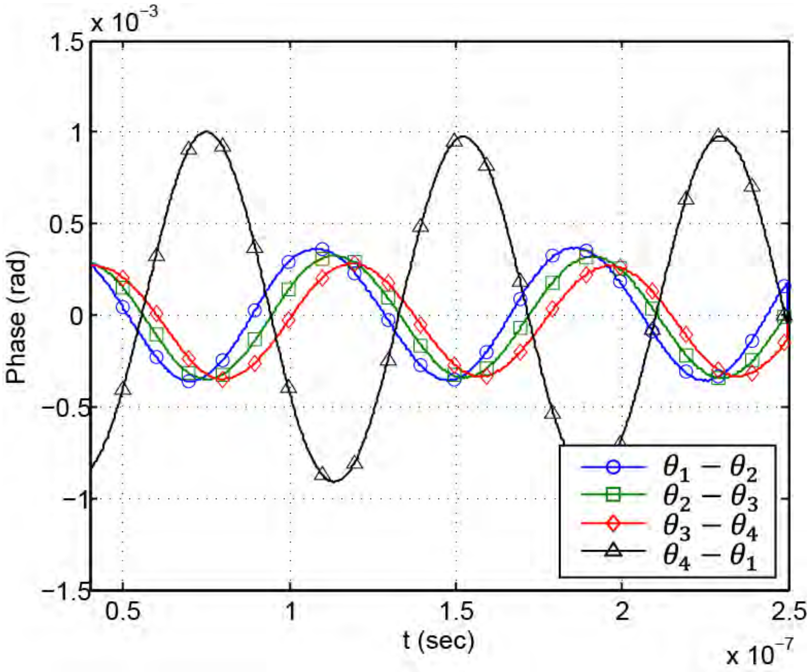

Figure 4.43: Simulated phase modulation for 4-stage coupled oscillator.

It is worth generalizing the analysis to N-stage coupled oscillators. For example, the effective frequency shift of a three-stage coupled oscillator shown in Fig. 4.42(c) is

$$\left(\frac{\Delta\omega}{\omega_0}\right)_{eff} = \frac{2}{3}\frac{\Delta\omega}{\omega_0}. \tag{4.50}$$

On the other hand, without detailed proof, the noise current generated from OSC$_1$ leads to phase perturbation on $\theta_3 - \theta_1$ that is 2/3 of ϕ_n but only 1/3 of ϕ_n on the other two outputs ($\theta_1 - \theta_2$ and $\theta_2 - \theta_3$). Therefore the SNR of such 3-stage coupled oscillator is

$$SNR_3 = \frac{\left(\frac{2}{3}\frac{\Delta\omega}{\omega_0}S\right)^2}{\left(\left(\frac{2}{3}\phi_n\right)^2 + 2\left(\frac{1}{3}\phi_n\right)^2\right)} = \frac{2}{3}SNR_0. \tag{4.51}$$

In the same way, the SNR of 4-stage coupled oscillator (Fig. 4.42(d)) is

$$SNR_4 = \frac{\left(\frac{3}{4}\frac{\Delta\omega}{\omega_0}S\right)^2}{\left(\left(\frac{3}{4}\phi_n\right)^2 + 3\left(\frac{1}{4}\phi_n\right)^2\right)} = \frac{3}{4}SNR_0. \tag{4.52}$$

For N-stage coupled oscillator (Fig. 4.42(e)),

$$SNR_N = \frac{N-1}{N} SNR_0. \tag{4.53}$$

Note that as N goes to infinity, the SNR converges to SNR_0. This can be explained intuitively. First, the frequency perturbation on the sensing oscillator (OSC_1) has negligible effect on the oscillation frequency of the whole system. From sensor perspective, this preserves the maximum frequency shift. Next, due to excessively long latency, there is no phase correlation between the input and the output of OSC_1, and hence there is no phase reduction effect as in two mutually-locked oscillators.

To validate the (4.52), Fig. 4.43 shows the simulated phase modulation at each phase differences of a 4-stage coupled oscillator (Fig. 4.42(d)) when injecting a noise current into OSC_1 at 10 MHz. Obviously, the effects of noise pulling on each individual oscillator are not identical; the one generating the noise will experience pulling sensitivity that is three times larger than all the other outputs.

4.6.3 Path Mismatch Derivation

As discussed in section IV-D, QVCO noise leaks to the output due to path mismatch, which can be quantified by mismatch in the injection-locking bandwidth $\Delta\omega_p$ ($= \omega_{p1} - \omega_{p2}$). To relate the amount of mismatch to parameters of interest, total derivative is applied to (4.12):

$$\Delta\omega_p = \frac{\partial\omega_p}{\partial\omega_0}\Delta\omega_0 + \frac{\partial\omega_p}{\partial Q}\Delta Q + \frac{\partial\omega_p}{\partial I_{inj}}\Delta I_{inj} + \frac{\partial\omega_p}{\partial I_{osc}}\Delta I_{osc}, \tag{4.54}$$

$$\frac{\partial\omega_p}{\partial\omega_0} = \frac{\omega_p}{\omega_0} + G \cdot \frac{\partial\theta_{ss}}{\partial\omega_0}, \tag{4.55}$$

$$\frac{\partial\omega_p}{\partial Q} = -\frac{\omega_p}{Q} + G \cdot \frac{\partial\theta_{ss}}{\partial Q}, \tag{4.56}$$

$$\frac{\partial\omega_p}{\partial I_{inj}} = H\frac{1}{I_{inj}} + G \cdot \frac{\partial\theta_{ss}}{\partial I_{inj}}, \tag{4.57}$$

$$\frac{\partial\omega_p}{\partial I_{osc}} = -H\frac{1}{I_{osc}} + G \cdot \frac{\partial\theta_{ss}}{\partial I_{osc}}, \tag{4.58}$$

$$G = \frac{\omega_0}{2Q}\frac{K \sin\theta_{ss}\,(2K^2 + K\cos\theta_{ss} - 1)}{(1 + K\cos\theta_{ss})^3}, \tag{4.59}$$

$$H = \frac{\omega_0}{2Q}\frac{K(2K + \cos\theta_{ss} - K\cos^2\theta_{ss})}{(1 + K\cos\theta_{ss})^3}, \tag{4.60}$$

where

$$\Delta\theta_{ss} = \frac{\partial\theta_{ss}}{\partial\omega_0}\Delta\omega_0 + \frac{\partial\theta_{ss}}{\partial Q}\Delta Q + \frac{\partial\theta_{ss}}{\partial I_{inj}}\Delta I_{inj} + \frac{\partial\theta_{ss}}{\partial I_{osc}}\Delta I_{osc}, \tag{4.61}$$

$$\frac{\partial\theta_{ss}}{\partial\omega_0} = 2Q\frac{(1 + K\cos\theta_{ss})^2}{K(K + \cos\theta_{ss})}\frac{1}{\omega_0}, \tag{4.62}$$

$$\frac{\partial\theta_{ss}}{\partial Q} = \sin\theta_{ss}\frac{(1 + K\cos\theta_{ss})}{K + \cos\theta_{ss}}\frac{1}{Q}, \tag{4.63}$$

$$\frac{\partial\theta_{ss}}{\partial I_{inj}} = \frac{-\sin\theta_{ss}}{K + \cos\theta_{ss}}\frac{1}{I_{inj}}, \tag{4.64}$$

$$\frac{\partial\theta_{ss}}{\partial I_{osc}} = \frac{\sin\theta_{ss}}{K + \cos\theta_{ss}}\frac{1}{I_{osc}}. \tag{4.65}$$

4.7 Chapter Summary

This chapter presents the design and the implementation of an oscillator-based reactance sensor using injection-locking. First, system specification for flow cytometry is discussed. Next, we review the conventional oscillator sensors and present the proposed interferometry architecture with ILO sensors. The system noise is analyzed in details including circuit non-idealities such as injection strength mismatches. Several circuit techniques are introduced to improve phase error and to reduce the chopping induced DC offsets. In the measurements, detailed study of sensor performance is presented and flow cytometry is demonstrated. Comparisons with the prior works are given. Finally, we discussed the sensor SNR for coupled oscillators.

Chapter 5

Injection-Locked Oscillator Sensors for Molecular Sensing

Molecular sensing finds wide applications in the field of medicine and biology. For instance, the enzyme-linked immunosorbent assay (ELISA), a technique based on the detection of antibody-antigen binding, is routinely used for diseases diagnosis. DNA sequencing is yet another good example which forms the whole theme of Precision Medicine. In this chapter, two different molecular targets are measured at microwave frequencies based on the sensor architecture presented in Chapter 4. First, glucose sensing is presented in Section 5.1. The experimental results show that sensitivity close to the physiological blood sugar level of human is achievable. Moreover, it only requires a sample volume as small as 180 pL. The sensor is reusable and can be used for continuous glucose monitoring applications. In Section 5.2, measurements on protein conformation change are demonstrated. In order to reduce sensor flicker noise, a novel chopping technique based on near-field modulation is presented. Dynamic range is enhanced through system architectural improvement. Measurements performed on thermal-cycled bovine serum albumin solutions (BSA) shows that the microwave sensing can also be used in drug discovery applications.

5.1 Glucose Sensing

As more than 8% of world population suffers from diabetes, the importance of continuous glucose monitoring (CGM) cannot be emphasized enough. Though tremendous effort has been put into CGM system [94], measurements using test strips with frequent finger pricks a day are still an inevitable action, resulting in high (~$0.7 per strip). To avoid chemical-based glucose measurements, which require reduction-oxidation reaction to take place, dielectric spectroscopy measurements on aqueous mediums at microwave frequencies have been pursued as an alternative [95, 96, 97]. Dielectric measurement can be potentially non-invasive and facilitates the re-use of the sensor. Study shows that 135 mg/dL of concentration difference in human blood induces a change of *one* in the real part of the permittivity at 10 GHz [95], demonstrating the potential of dielectric-based glucose sensing. Unfortunately, the study is conducted with a commercial coaxial probe kit with VNA while requiring 10 mL of blood sample and is therefore not yet ready for clinical application. Planar transmission-line (t-line) sensors can also be used to characterize the concentration of the aqueous solution by measuring the change in line propagation constant or shift in the resonance frequency [96] – [97]. For example, [97] introduces a double stub resonator loaded with inter-digitated capacitors (IDCs), enabling simultaneous characterization of two different samples. However, the measured glucose concentration, ranging from 1500 ~ 8000 mg/dL, is not close to the actual blood sugar level (80 ~ 200 mg/dL).

To enable point-of-care (PoC), device miniaturization is a must to bring portability for CGM. This motivates the application of CMOS technology for bio-sensing purpose. Several CMOS impedance analyzers have been demonstrated with significantly reduced sensing volume [62, 64]. However, none to date demonstrate glucose measurements with sensitivity level close to the actual blood sugar level.

In this section, a reconfigurable sensor architecture is provided for glucose concentration measurements covering a wide concentration range. Sensing is performed directly *on* CMOS with microfluidics using coplanar electrodes. A sensitivity limit of 20 mg/dL is achieved at 0.18 nL (50-μm × 60-μm × 60-μm) of sensing volume. To the authors' knowledge, this work presents the highest sensitivity level with the smallest sample volume. Thanks to the scalability offered by CMOS, four independent sensors, each performing measurements at 6-, 11-, 17-, and 30-GHz, are integrated on a single chip.

5.1.1 System Architecture

Fig. 5.1 shows the conceptual view of the sensors in this work. Two pairs of parallel electrodes forms two differential capacitors with one serving as the reference while the other performing detection on the injected sample medium. Each capacitor is covered by isolated fluidic channel with the reference capacitor immersed in de-ionized water at all time. Dielectric characterization of the glucose solution is performed by measuring the induced capacitance change as the sample on top of the sensing capacitor is being altered.

Fig. 5.2 depicts the system architecture. To accommodate large concentration difference without sacrificing the sensitivity, configurability is introduced. Such a concept is similar to the coarse and fine detection in most electronic design such as a zoom-in ADC. When detecting high concentration, the system is configured into free-running frequency measurements, as shown in Fig. 5.2(a). In this setup, the two capacitance sensors are embedded as part of the oscillator's LC-tank. Shift in the oscillation frequency of the sensing oscillator (OSC_2) is measured through the beat frequency (F_{beat}) after mixing with oscillation signal from OSC_1. The mapping between the capacitance and the normalized frequency shift can be characterized by

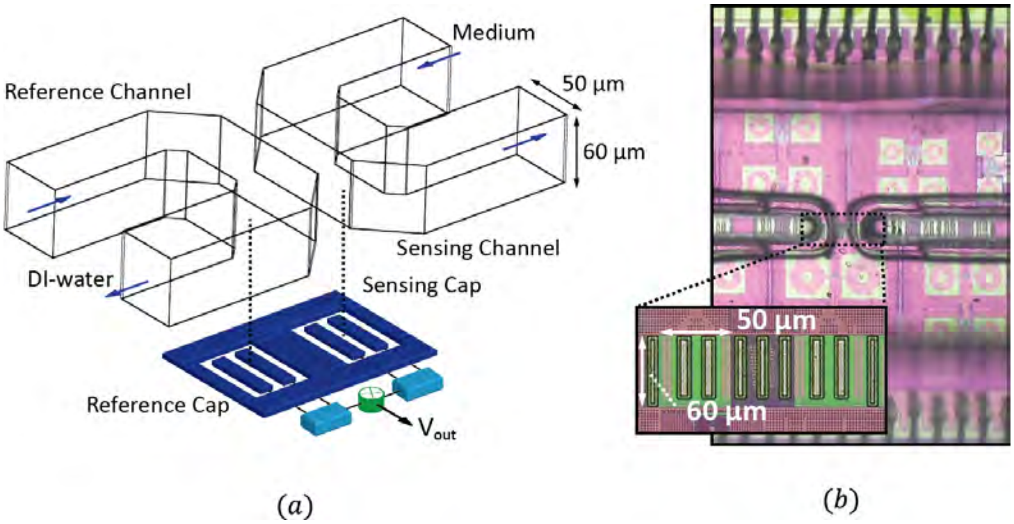

Figure 5.1: (a) Capacitor sensors with microfluidic channels. (b) Chip micrograph and electrode dimensions.

$$\frac{\Delta\omega}{\omega_0} = \frac{1}{\sqrt{1 + \Delta C / C_0}} - 1. \tag{5.1}$$

where C_0 represents the total bulk capacitance of the LC-tank. Here no linear approximation is made as the sample permittivity can span wide range, e.g. air vs. water. To extract the permittivity from the measured frequency shift, either reference liquid calibration with polynomial fitting or EM simulation is necessary. Such measurements provide unlimited dynamic range at the cost of elevated noise level due to degraded tank-Q as capacitors are loaded with the lossy medium.

When measuring moderate glucose concentration (500 – 2000 mg/dL), the system is configured into an interferometer-based architecture (Fig. 5.2(b)) where the same LC-tank is driven by a gm-stage [58]. The induced capacitance change perturbs the LC-tank resonance frequency, which is captured by measuring the phase shift using an active mixer. The excitation signals are generated using the on-chip QVCO. The benefit of the interferometer architecture is that phase noise from the source is cancelled after self-mixing.

Finally, as glucose concentration is lowered to a level close to that of human blood, the LC-tanks are made to oscillate again but remain injection-locked to the source for enhanced sensitivity [67]. This enables the use of phase amplification property offered by the injection-locked-oscillator (ILO). The phase shift due to the capacitance change can be derived as

$$\theta \approx 2Q \cdot \frac{I_{osc}}{I_{inj}} \cdot \frac{\Delta\omega}{\omega_0} \approx Q \cdot \frac{I_{osc}}{I_{inj}} \cdot \frac{\Delta C}{C_0}, \tag{5.2}$$

where the amplification factor is proportional to the ratio of I_{osc} and I_{inj}. In all three modes, the same mixer is re-used, saving the hardware complexity considerably.

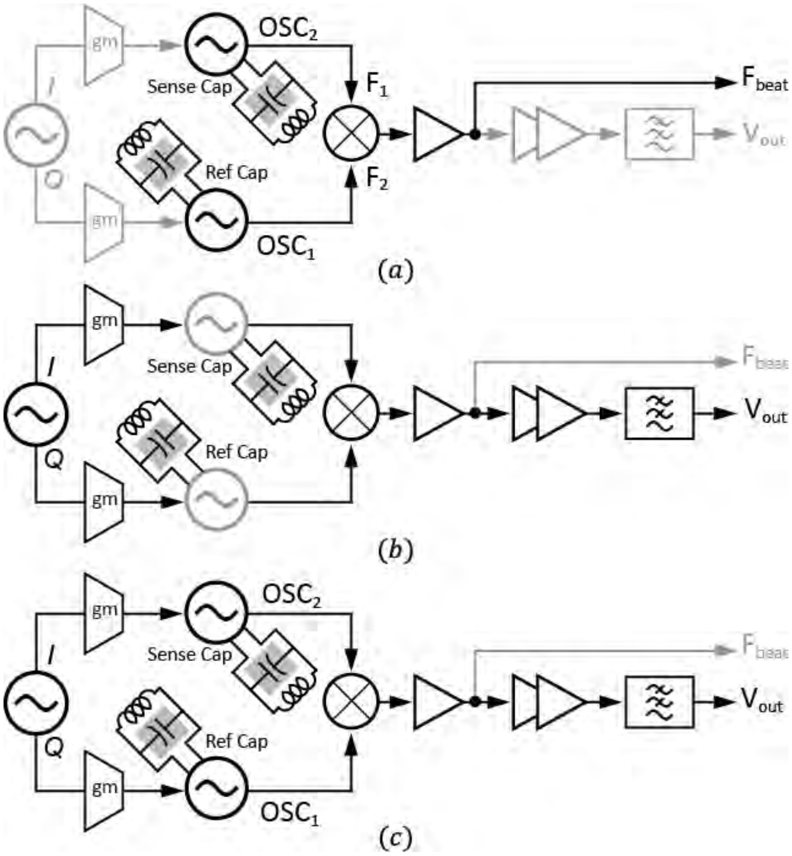

Figure 5.2: Reconfigurable sensor architecture: (a) Mode-I, (b) Mode-II, and (c) Mode-III.

As dielectric relaxation of aqueous medium is a strong function of molecular thermal energy, temperature regulation is included (section 4.3.8).

5.1.2 Glucose Measurements

Fig. 5.3 shows the microfluidic structure and the setup. Fluidic channels, made by replica-molding using PDMS, consist of multiple inlets to facilitate the infusion of different samples. Interestingly, we found that the signal is sensitive to both the flow rate of the medium as well as the time constant of the fluidic network. To remedy these effects, data is collected when the medium is static. On the other hand, sensor drift is reduced by employing correlated double sampling (CDS) where the glucose medium is alternating with DI-water every ten seconds using tube clamps operated manually.

Fig. 5.4 shows the measured time-domain waveforms in different configurations, demonstrating that measurement repeatability is achievable. In Fig. 5.4(c), the measured V_{out} are referred to induced capacitance change with the aid of on-chip capacitance reference after gain calibration. Signals are quantified by averaging over at least 16 CDS

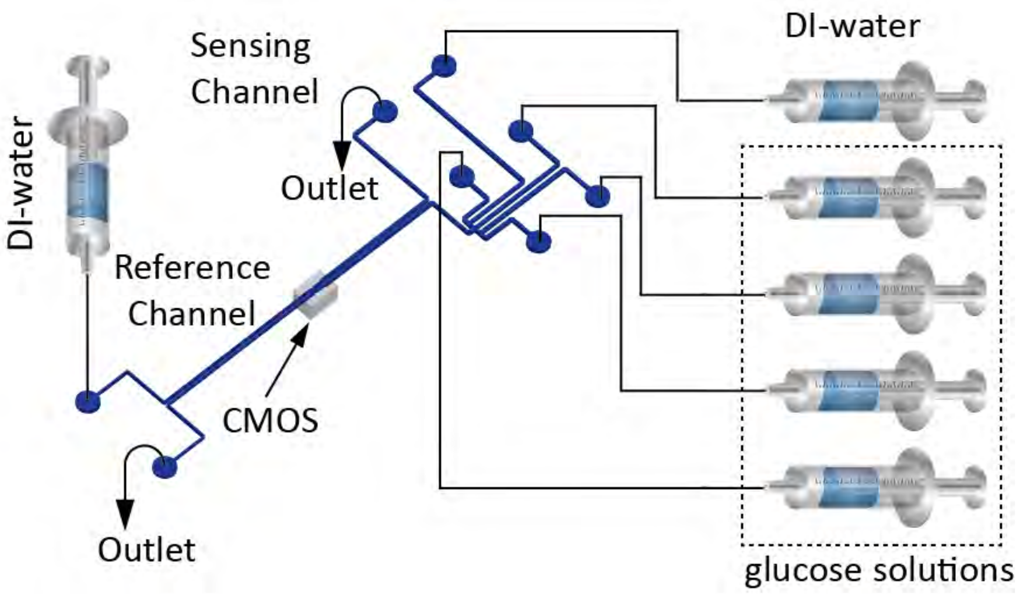

Figure 5.3: Microfluidic structure and the measurement setup.

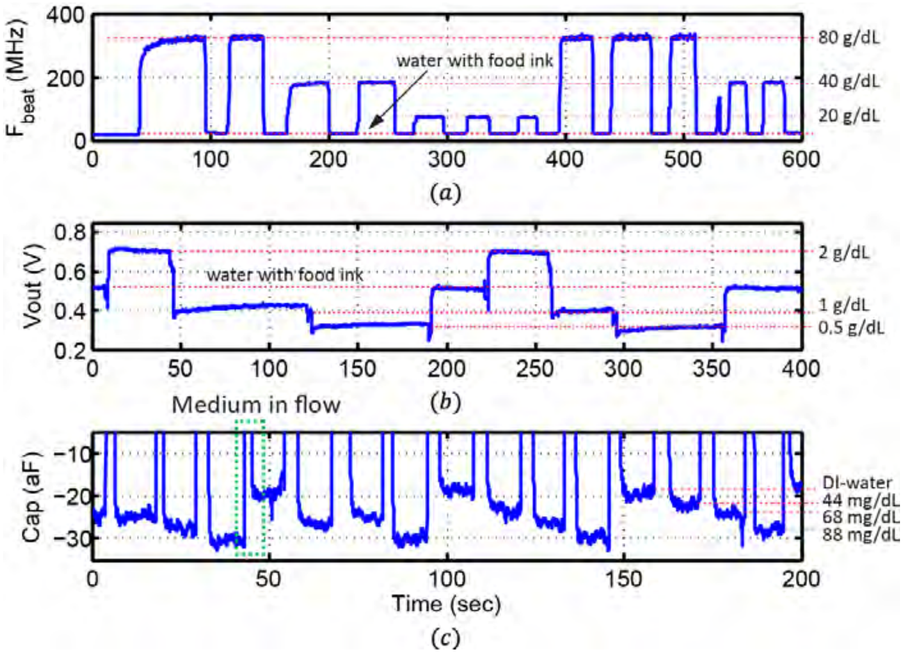

Figure 5.4: Measure time-domain waveforms of glucose medium in different configurations: (a) Mode-I, (b) Mode-II, and (c) Mode-III.

cycles. Fig. 5.5 shows the quantified results at different glucose concentration, which is also characterized using a commercial glucose meter. The error bar stands for one standard deviation of the collected signal sequence from CDS. The minimum resolvable

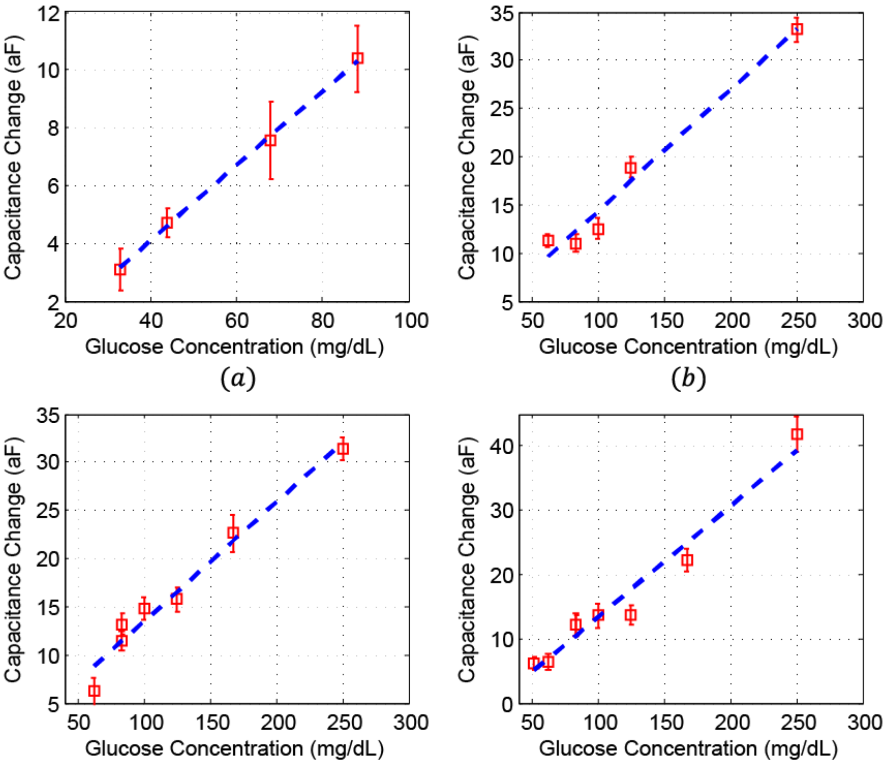

(*a*) (*b*)

(*c*) (*d*)

Figure 5.5: Measured induced capacitance change (reference to DI-water) at different concentration and sensing channels: (a) 6-GHz, (b) 11.-GHz, (c) 17-GHz, and (d) 30-GHz.

	MTT'13 [1]	IMS'13 [2]	IMS'14 [3]	IMS'13 [4]	This work
Frequency	5 – 15 GHz	DC – 12 GHz	DC – 50 GHz	1 – 50 GHz	6/11/17/30-GHz
Sensor	Coax; microstrip	Microstrip	Cap in resonator	CPW line	Cap in resonator
Electronics	VNA	Discrete	VNA	CMOS (Rx-only)	CMOS
Sample	Human Blood	Glucose Medium	Glucose Medium	Chemicals, Saline	Glucose Medium
Volume	10 mL	10 mL*	$200\times100\ \mu\text{m}^2$** (height n.a.)	0.09 nL	0.18 nL
Measured Concentration Range	0 – 4 g/dL	0 – 5 g/dL	15 – 80 g/dL	n.a.	0 – 80 g/dL
Sensitivity Limit	n.a.	n.a.	n.a.	n.a.	20 mg/dL

*Similar device as in [1].

** Estimate from the figure in the paper.

[1] Hofmann, T-MTT'13. [2] Guarin, IMS'13. [3] Chretiennot, IMS'14. [4] Chien, IMS'13.

Table 5.1: Comparisons with prior works.

concentration difference is dictated by the circuit flicker noise. The sensitivity limit, defined as SNR = 0 dB, is 20 mg/dL at worst-case. Each channel consumes 18.5 mW from 1-V supply excluding the power in the heater. Table 5.1 compares with prior works.

5.2 Protein Conformation Detection

Study of the protein-protein interactions is essential for drug discovery and validation for tomorrow's therapeutics. Conventional approaches utilizing UV/VIS spectrometry and fluorescence require dedicated optical instrumentation as well as sophisticated sample preparation. On the other hand, spectroscopy at microwaves using near-field coupling shows great potential for label-free bio-sensing. In particular, probing macromolecules such as proteins and DNA exhibits significant responses through dispersive polarization. For instance, [33] studies the effect of temperature and pH modulation on the unfolding and refolding of RNase A using a slot antenna while [98] demonstrates the detection of DNA at few pM of sensitivity.

Recently, miniaturized sensor-on-CMOS has been pursued due to not only its versatility for a multi-parameter sensing but also significant improvement in sensitivity offered by the direct integration. At microwave frequencies, interferometry with injection-locked oscillators (ILO) as sensor is utilized for high-throughput single-cell detection [67]. However, substantial flicker noise limits the achievable sensitivity at low filtering bandwidth for detecting minute differences. In this work, we investigate the origins of the flicker noise in [67] and propose a near-field modulation chopping technique, which lowers the corner frequency by a factor of 40 with bio-sensing results.

5.2.1 Conventional Chopping

Fig. 5.6 shows the simplified block diagram of a highly sensitive capacitive sensor based on interferometry [67]. The capacitance change induced by different sample permittivity is detected through frequency-to-phase transduction of an LC-oscillator being injection-locked to an excitation source. To avoid signal corruption caused by the mixer 1/f noise, chopping is mandatory. This is achieved by applying BPSK modulation to one of the injection paths while utilizing the gain inversion property of the phase detector (PD) in the vicinity of ±90°. However, such an approach inevitably suffers from the undesirable up-conversion of the 1/f noise presented in both the injection current ($I_{\mathrm{inj}1,2}$) and the ILO phase noise ($L_{\mathrm{ILO}1,2}$). To facilitate the understanding of their origins, Fig. 5.6(b) shows the ILO model for phasor analysis [84]. First, the amplitude noise of $I_{\mathrm{inj}1,2}$ manifest as phase noise at the input of the mixer (Fig. 5.6(c)). On the other hand, finite ILO 1/f phase noise leaks inevitably since injection-locking shapes the ILO in-band phase noise merely with 1st-order high-pass filtering. In either case, such phase perturbation is indistinguishable from the chopped signal. To make things worse, the 1/f noise in L_{ILO} experience the same phase amplification as the desired signal due to its

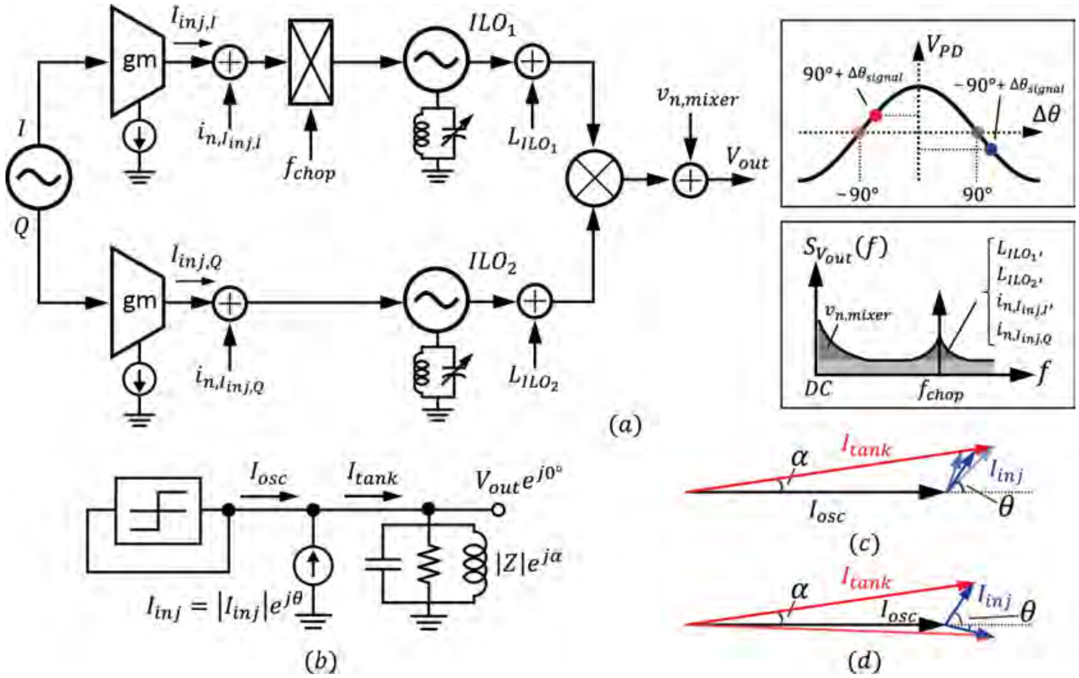

Figure 5.6: (a) Interferometry sensor architecture with BPSK modulation. (b) ILO circuit model. (c) and (d) Phasor analysis for I_{inj} and L_{ILO} noise.

equivalence to low-frequency FM on the ILO oscillation, compromising the high sensitivity offered by injection locking. Such phenomenon is modeled by a noise-modulated LC-tank phase shift (α) in Fig. 5.6(d). Note that such up-conversion of 1/f noise cannot be alleviated through OOK modulation, an approach widely used in optical interferometry using chopper wheels [58]. This is due to loss of 1/f noise information during one half of the modulation cycle.

5.2.2 Near-Field Modulation

In this work, we propose a field modulation technique to significantly reduce sensor 1/f noise. The main idea is to periodically prohibit the sensing operation by shielding the E-fields, emitted out of the sensor electrodes, from penetrating into the sample. Such shielding can be achieved by adding a pair of shielding electrodes ($P_{1\text{-}2}$) on top of the sensing ones ($P_{3\text{-}4}$) with a switch bridging the two (Fig. 5.7). As switch is closed, a low-impedance path for the displacement current is created to reduce the sensing sensitivity. On the contrary, $P_{1\text{-}2}$ is floated with an opened switch and the sensing is restored through field coupling. By alternating between the two modes, signal chopping is achieved while keeping the operation in the vicinity of +90° on the PD transfer curve (Fig. 5.7(c)). As the 1/f noise experiences neither phase nor amplitude modulation, the up-conversion is therefore mitigated. Note that such dynamic operation results in different capacitance loading and modulates the ILO oscillation frequency. To ensure proper locking, FSK needs to be applied to the excitation coherently to track such frequency deviation.

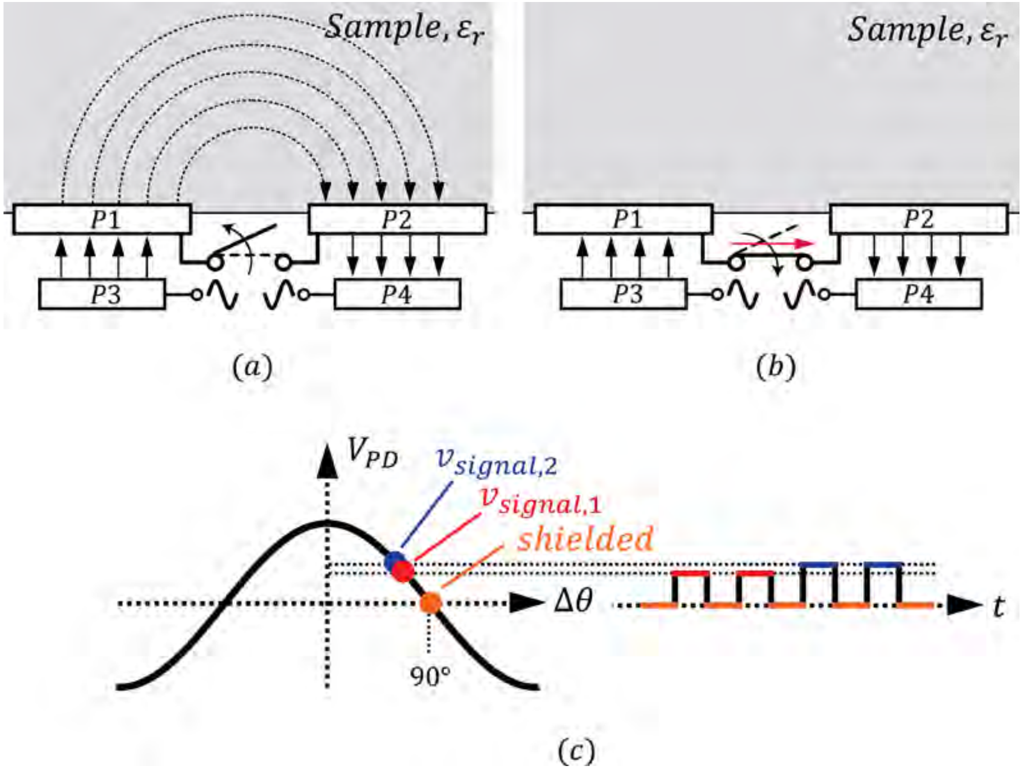

Figure 5.7. (a) Sensing mode. (b) Shielding mode. (c) Chopping illustration.

5.2.3 Sensor Design with Maximum Dynamic Range

As ILOs exhibit finite locking range, sensor dynamic range is severely limited [67]. To maximize the range of operation, this work employs feedback-around-the-sensor architecture. As shown in Fig. 5.8, the output of the sensor front-end (V_{out1}) is locked against a constant V_{ref} through feedback, which adjusts V_{ctrl2} of the varactor in ILO_2 and compensates for the sampled-induced capacitance change. Such feedback system bears similarity as a delay-locked loop (DLL) where ILO_2 serves as high-gain phase shifter. Measurement exhibits 50-dB loop gain at 100-Hz closed-loop bandwidth. Temperature is regulated using on-chip BJT diodes and NMOS heaters in linear region.

Fig. 5.9 presents the 3D illustration of the proposed field-modulated capacitor and the circuit schematic of the signal path. Each sensing electrode, implemented in M8 with a dimension of 45 μm × 6.4 μm, is enclosed by both M7 and M9-AP layers in a stripline configuration. The latter serves as the shielding layer with 1.8 μm extension relative to the sensing electrode to minimize field leakage. The gate of the shielding switch (SW_1) is modulated at 50-MHz chopping frequency while the switch presents 82-Ω R_{on} and 2.5-fF C_{off}. In addition, two units of switched-capacitor (SW_2), implemented with M6 underneath shielding M7, serve as on-chip reference. Each unit presents a measured frequency shift of 857 ppm. The QVCO switched-capacitor bank consists of 15 units with

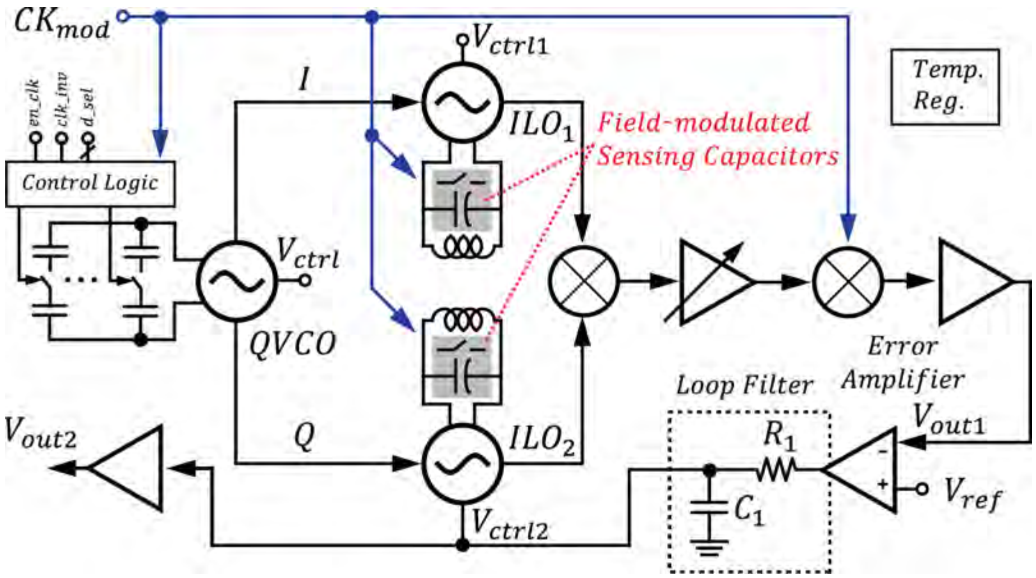

Figure 5.8. System block diagram.

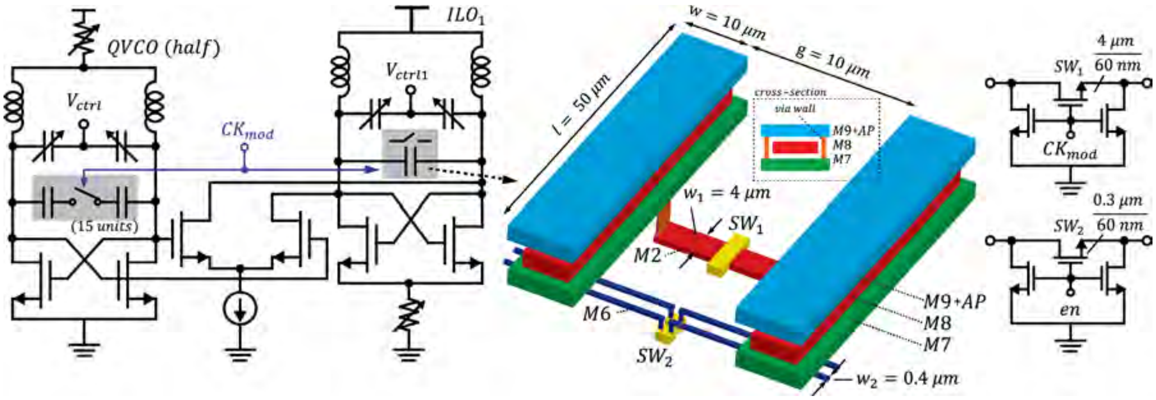

Figure 5.9. Circuit schematic and 3D illustration of the sensing capacitor.

19.7-% tuning range. Each unit can be clocked individually with phase inversion capability.

5.2.4 Experimental Results

The shielding effect on the ILO oscillation frequency is first evaluated (Fig. 5.10(a)). Such *calibration* determines the number of switched-capacitors in QVCO to be clocked. Next, the shielding capability is tested by configuring SW_1 in static state while modulating SW_2. From Fig. 5.10(b), sensitivity is reduced by 40x as shielding is enabled. This factor matches the equivalent circuit model of the electrodes extracted from both the field and circuit simulations.

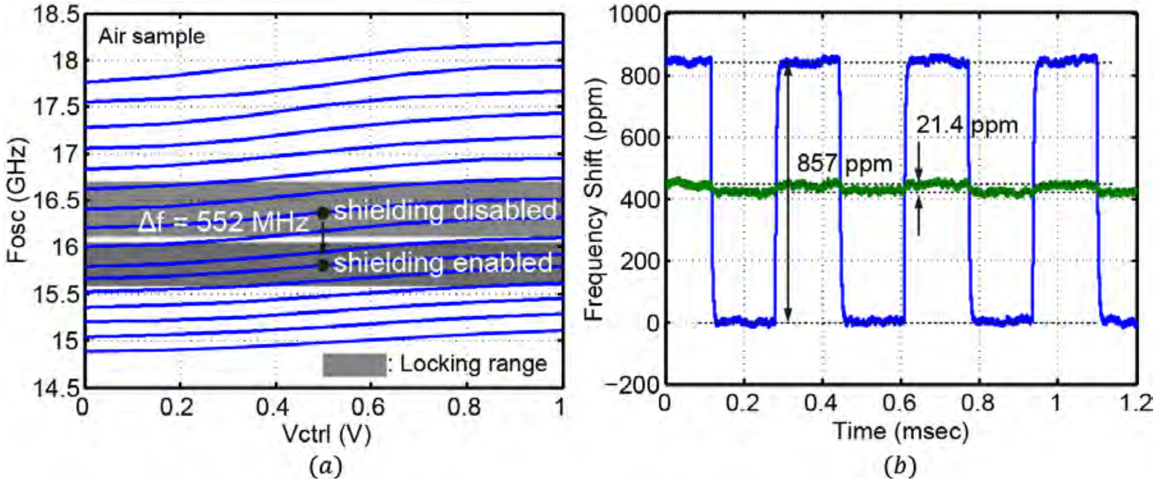

Figure 5.10. (a) QVCO tuning and ILO locking ranges. (b) Shielding efficacy.

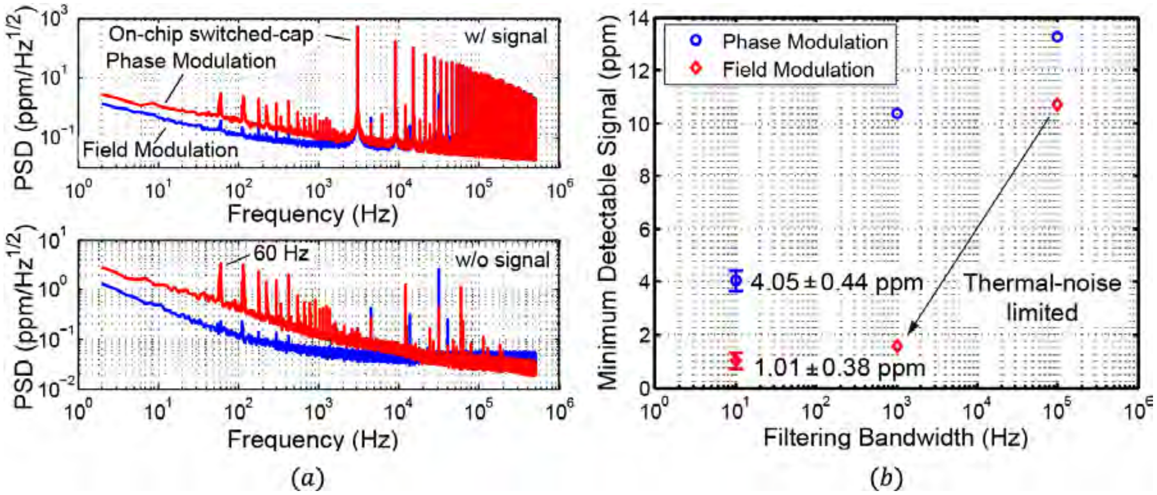

Figure 5.11. (a) Output PSD. (b) Sensitivity limit at different filtering bandwidth with off-chip RC filters.

Fig. 5.11(a) compares the open-loop output PSD from V_{out1}. Flicker noise corner is reduced from 10 kHz to 250 Hz with the proposed near-field modulation while the in-band is reduced by 11 dB. Such reduction matches to the level of spur rejection as we modulate V_{ctrl2} with 50-mV$_{\text{pp}}$ sinewave at 100 Hz. The residual flicker noise is due to finite locking transient during mode transition. Sensitivity limit at different off-chip filtering is shown in Fig. 5.11(b).

Fig. 5.12 shows the die micrograph and the setup for protein solution measurements. Two independent fluidic channels are employed with the reference channel filled with DI-water. Benefiting from the feedback operation, the ILO remains locked when measuring both air and water. As each material represents the extremes of the permittivity distribution for biological samples, this work achieves the maximum

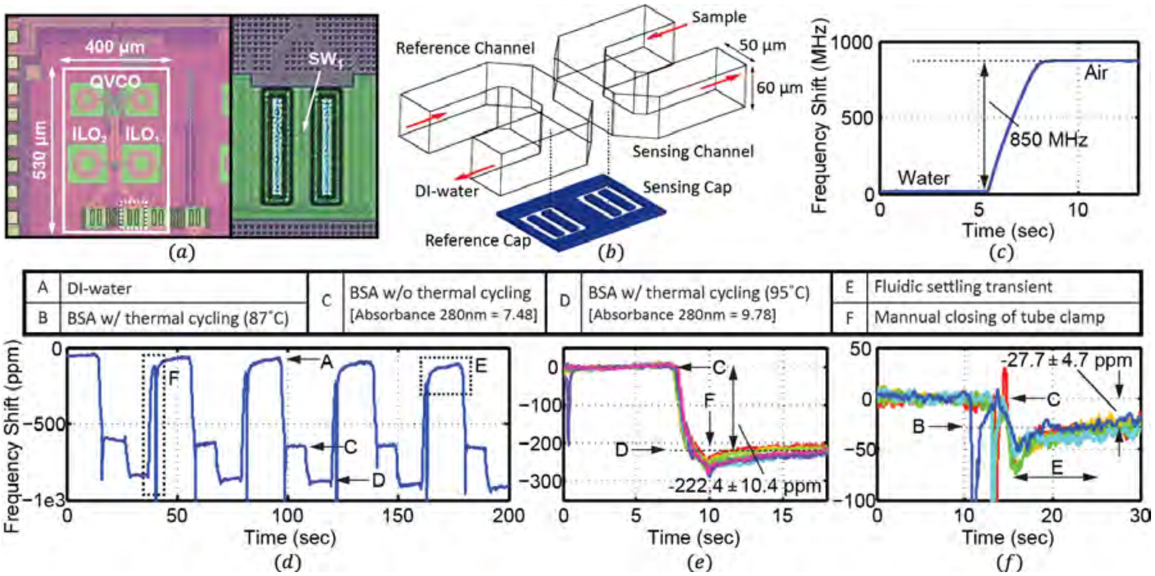

Figure 5.12. (a) Chip micrograph. (b) Microfluidic integration. (c) Dynamic range measurements. (d) Repeated BSA measurements. (e) and (f) CDS between two different BSA solutions.

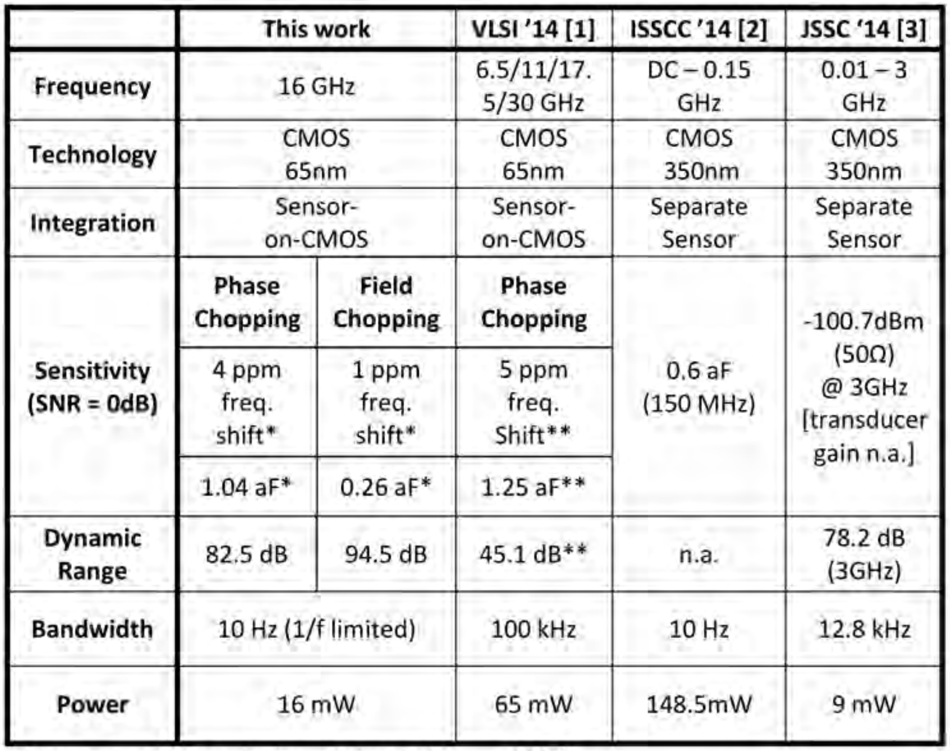

	This work		VLSI '14 [1]	ISSCC '14 [2]	JSSC '14 [3]
Frequency	16 GHz		6.5/11/17.5/30 GHz	DC – 0.15 GHz	0.01 – 3 GHz
Technology	CMOS 65nm		CMOS 65nm	CMOS 350nm	CMOS 350nm
Integration	Sensor-on-CMOS		Sensor-on-CMOS	Separate Sensor	Separate Sensor
Sensitivity (SNR = 0dB)	**Phase Chopping**	**Field Chopping**	**Phase Chopping**	0.6 aF (150 MHz)	-100.7dBm (50Ω) @ 3GHz [transducer gain n.a.]
	4 ppm freq. shift*	1 ppm freq. shift*	5 ppm freq. Shift**		
	1.04 aF*	0.26 aF*	1.25 aF**		
Dynamic Range	82.5 dB	94.5 dB	45.1 dB**	n.a.	78.2 dB (3GHz)
Bandwidth	10 Hz (1/f limited)		100 kHz	10 Hz	12.8 kHz
Power	16 mW		65 mW	148.5mW	9 mW

*1-sec acquisition window, estimated C_{bulk} = 130 fF

** 30-GHz channel, 4-msec acquisition window, estimated C_{bulk} = 125 fF

[1] Chien, et al. [2] G. Ferrari, et al. [3] M. Bakhshiani, et al.

Table 5.2: Comparison with prior works.

dynamic range of 94.5 dB. To study protein conformation changes, BSA (66.5 kDa) solutions at 10% weight concentration are prepared. Thermal cycling is applied to the same BSA solution by heating up to 87 or 95°C for more than 15 minutes. Measurements are performed after cooling to the room temperature (22°C). Fig. 5.12(d)-(f) shows the measured time-domain waveforms, demonstrating the detection of protein structural change, which has been verified with UV-VIS Nanodrop spectrophotometry, at 180 pL of sensing volume. Correlated-double sampling has been applied to combat drifts. Table 5.2 compares our sensor with prior works.

5.3 Chapter Summary

Molecular sensing is studied in this chapter. Experiments on glucose and bovine serum albumin (BSA) solutions show that dielectric sensing at microwave frequencies for molecular detection is achievable with our highly sensitive ILO sensors. From electronic perspective, two circuit techniques are presented to remedy the limitation in the sensor architecture presented in Chapter 4. These include near-field modulation for 1/f noise reduction and feedback-around-sensor architecture to maximize the dynamic range.

Chapter 6

Conclusion and Future Research Direction

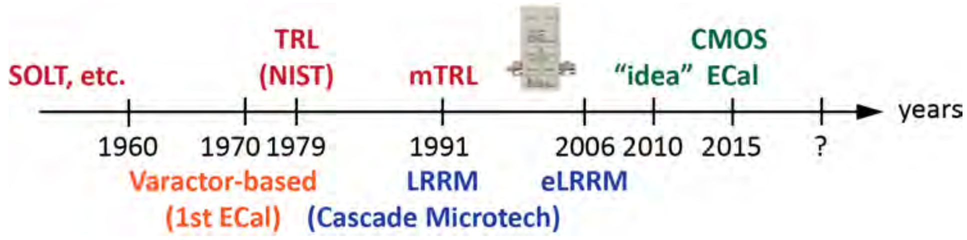

Figure 6.1. History of VNA calibration.

Fig. 6.1 shows a brief history of VNA calibration algorithms. As mentioned in Section 2.1, one-port E-Cal was first proposed in 1970. However, it required prior knowledge on the actual varactor capacitance at different biasing voltages. Later on, two major VNA calibrations, the TRL and LRRM, were invented and have been the golden standards for the past forty years. This research proposes a single-element electronic calibration exploiting the impedance modulation of CMOS transistors without any prior knowledge of the on-chip impedance, reducing the cost while minimizing the probing errors. The experimental results are demonstrated in the problem of de-embedding.

Efforts have been attempted to extend the concept toward full VNA calibration. Two additional algorithms are presented: dual-element and single-element approaches. These new algorithms are mathematically accurate but verifications with actual measurements are still mandatory. Moreover, the effect of probing errors requires careful study at G-band (140 – 220 GHz) where the error is much more pronounced. Noise reduction using measurement redundancy must be investigated. The aim is to reduce the noise sensitivity to TRL-equivalent level.

On the other hand, two-times probing is nevertheless inevitable in the proposed single-element E-Cal: one on the calibration structure and the other on the device-under-

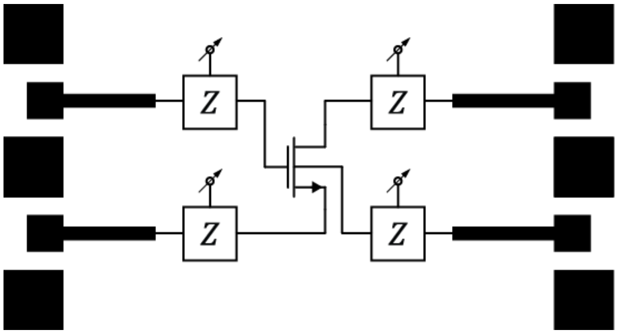

Figure 6.2. Embedded impedance modulators with DUT for single-element E-Cal.

test (DUT). Future work should innovate on embedding the impedance modulators into the DUT for *true* single-element electronic calibration (Fig. 6.2). It is also worth studying the application of the E-Cal concept to multi-port calibration. Such a technique will be beneficial for the characterization of differential circuits.

Finally, it is interesting to explore the possibility of adapting the concept to the other RF/microwave measurements including noise figure and linearity. Photonics is yet another research area.

In the second part, we presented a dielectric spectroscopy flow cytometer at microwave frequencies for high-throughput cell identification applications. The system sensitivity is enhanced through the use of injection-locking on oscillator-based capacitive sensors. Chopping techniques including phase and field modulations are presented to alleviate the flicker noise from the phase detector, to reduce chopping-induced DC offsets, and to prevent the up-conversion of the oscillator flicker noise. Flow cytometry and molecular measurements are demonstrated with microfluidic integration. Future work includes the characterization of mammalian cells. In particular, comparisons between different cancer cells are necessary in order to justify whether dielectric spectroscopy is applicable for label-free cell sorting.

Numerous research directions can be pursued based on this work. From electronic perspectives, approaches to reduce flicker noise corner frequency below 10 Hz are needed. This will enable zF sensitivity, which is beneficial for molecular sensing at reduced concentration. Next, broadband spectrometer architecture with more sampling frequencies is critical for measuring the spectroscopic response of the specimen. Pushing the frequencies toward sub-THz, e.g. 500 GHz, is yet another direction which will enable label-free detection of DNA resonance. A spectrometer example is illustrated in Fig. 6.3. On the other hand, it is of interest to apply injection-locking in a MEMS-oscillator for sensing purpose. Significant sensitivity improvement is expected due to excessive high-Q resonator. With the combination of BioMEMS, new tool for scientific study can be developed. The adoption of microwave dielectric spectroscopy for non-invasive glucose sensing is also worthwhile studying. Finally, circuit techniques to enable near-field imaging at sub-cellular resolution will open another new direction for cellular studies.

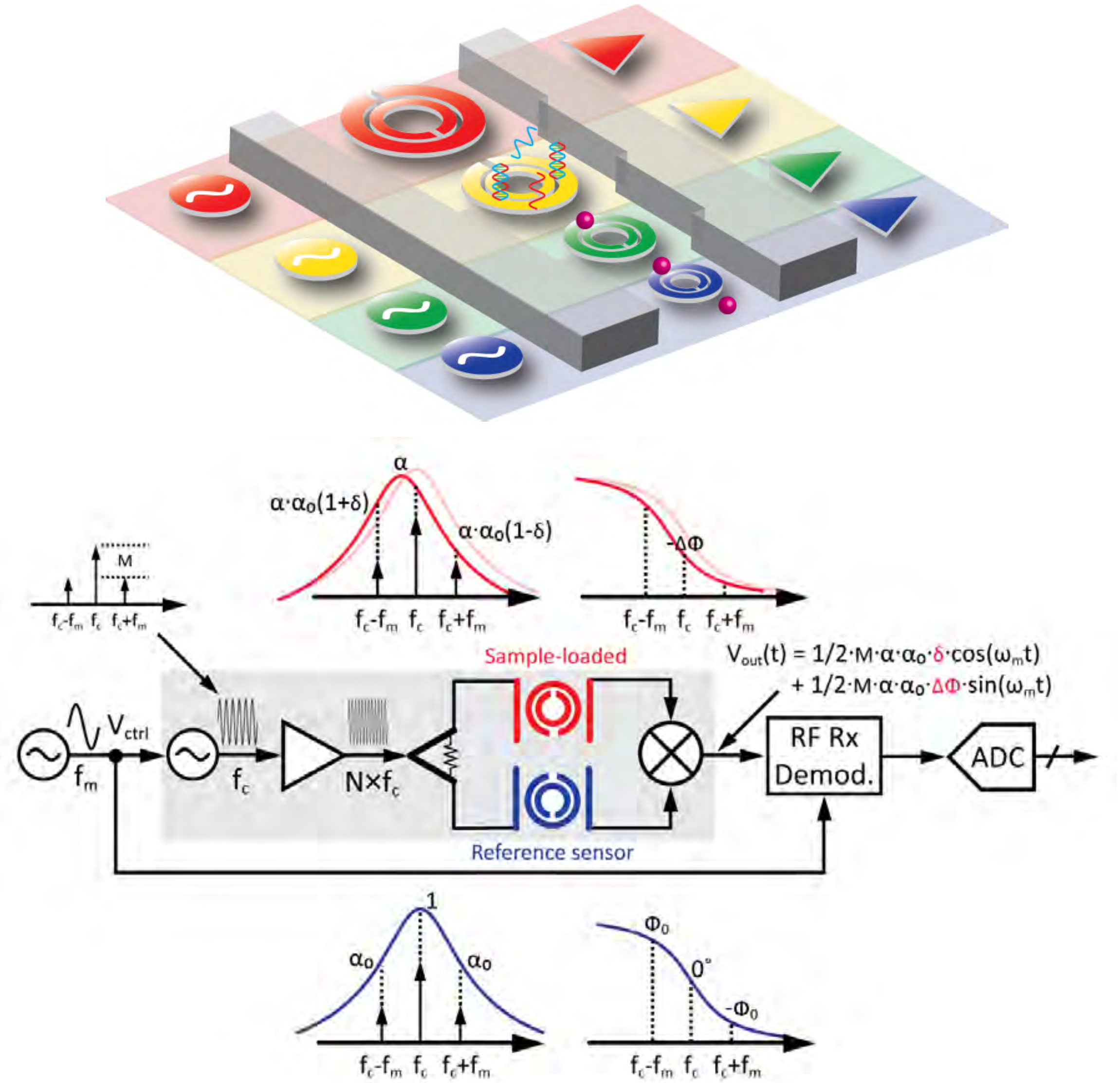

Figure 6.3. Conceptual view of a sub-THz spectrometer architecture.

Bibliography

1. S. V. Thyagarajan, S. Kang, and A. M. Niknejad, "A 240GHz wideband QPSK receiver in 65nm CMOS," in *Proc. IEEE Radio Frequency Integrated Circuits Symposium (RFIC)*, May 2014, pp. 357 – 360.
2. S. Kang, S. V. Thyagarajan, and A. M. Niknejad, "A 240GHz wideband QPSK transmitter in 65nm CMOS," in *Proc. IEEE Radio Frequency Integrated Circuits Symposium (RFIC)*, May 2014, pp. 353 – 356.
3. C. Wang, J.-C. Chien, H. Fang, K. Takei, J. Nah, E. Plis, S. Krishna, A. M. Niknejad, and A. Javey. "Self-aligned, extremely high frequency III–V metal-oxide-semiconductor field-effect transistors on rigid and flexible substrates", *Nano Letters*, 12 (8), pp. 4140 – 4145, 2012.
4. A. M. Niknejad, *Electromagnetics for High-Speed Analog and Digital Communication Circuits*, Cambridge University Press, 2007.
5. R. B. Marks, "A multiline method of network analyzer calibration," *IEEE Trans. Microw. Theory Tech.*, vol. 39, no. 7, pp. 1205 – 1215, Jul. 1991.
6. D. F. William, et. al., "Calibration-kit design for millimeter-wave silicon integrated circuits," *IEEE Trans. Microw. Theory Tech.*, vol. 61, no. 7, pp. 2685 – 2694, Jul. 2013.
7. H. Ito, et. al., "A simple through-only de-embedding method for on-wafer S-parameter measurements up to 110 GHz," in *IEEE MTT-S Int. Microw. Symp.*, Jun. 2008, pp. 383 – 386.
8. F. Kremer and A. Schönhals, *Broadband Dielectric Spectroscopy*, Springer, 2002.
9. K. C. Cheung, M. Di Berardino, G. Schade-Kampmann, M. Hebeisen, A. Pierzchalski, J. Bocsi, A. Mittag, A. Tárnok, "Microfluidic impedance-based flow cytometry," *Cytometry A*, 77(7) Jul. 2010, pp. 648 – 666.
10. D. Kajfez, "Numerical data processing of reflection coefficient circles," *IEEE Trans. Microw. Theory Tech.*, vol. 18, no. 2, pp. 96 – 100, Feb. 1970.
11. L. Hayden, "An enhanced line-reflect-reflect-match calibration," *67th ARFTG Conf. Dig.*, Jun., 2006, pp. 143 – 149.
12. A. A. Kidwai, et. al., "A fully integrated ultra-low insertion loss T/R switch for 802.11b/g/n application in 90 nm CMOS process," *IEEE J. of Solid-State Circuits*, vol. 44, no.5, pp. 1352 – 1360, May 2009.

13. D. F. Williams, “Accurate characteristic impedance measure-ment on silicon,” in *IEEE MTT-S Int. Microw. Symp.*, Jun. 1998, pp. 1917 – 1920.

14. D. F. Williams, U. Arz, and H. Grabinski, "Characteristic-impedance measurement error on lossy substrates," *IEEE Microwave Wireless Compon. Lett.*, vol. 11, no. 7, pp. 299 – 301, Jul. 2001.

15. http://www.sds.l-3com.com/advancedimaging/provision-at.htm

16. E. C. Fear, X. Li, S. C. Hagness, and M. A. Stuckly, "Confocal microwave imaging for breast cancer detection: localization of tumors in three dimnesions," *IEEE Trans. Biomed. Eng.*, vol. 49, no. 8, pp. 812 – 822, Aug. 2002.

17. E. J. Bond, X. Li, S. C. Hagness, and B. D. Van Veen, "Micorwave imaging via space-time beamforming for early detection of breast cancer," *IEEE Trans. Antennas Progpagat.*, vol. 51, no. 8, pp. 1690 – 1705, Aug. 2003.

18. J. T. Nevill, *Impedance Spectroscopy-Based Biosensors*, Dissertation, UC Berkeley, 2008.

19. E. H. Grant, R. J. Sheppard, and G. P. South, *Dielectric Behaviour of Biological Molecules in Solution*, Clarendon Press, Oxford, 1978.

20. H. Morgan, T. Sun, D. Holmes, S. Gawad, and N. G. Green, "Single cell dielectric spectroscopy," *J. of Physics D: Applied Physics*, 40, pp. 61 – 70, 2007.

21. A. Kotnala, S. Wheaton, and R. Gordon, "Playing the notes of DNA with light: extremely high frequency nanomechanical oscillations," *Nanoscale*, 2015, 7, pp. 2295 – 2300.

22. K. Grenier, D. Dubuc, T. Chen, F. Artis, T. Chretiennot, M. Poupot, and J.-J. Fournié, "Recent advances in microwave-based dielectric spectroscopy at the cellular level for cancer investigations," *IEEE Trans. Microw. Theory Tech.*, vol. 61, no. 5, pp. 2023 – 2030, May 2013.

23. C. Warwick, *Understanding the Kramers-Kronig relation using a pictorial proof*, Agilent 5990-5255EN.

24. D. Popovic, L. McCartney, C. Beasley, M. Lazebnik, M. Okoniewski, S. Hagness, and J. Booske, ”Precision open-ended coaxial probes for in vivo and ex vivo dielectric spectroscopy of biological tissues at microwave frequencies,” *IEEE Trans. Microw. Theory Tech.*, vol. 53, no. 5, pp. 1713 – 1722, May 2005.

25. M. Lazebnik, L. McCartney, D. Popovic, C. B. Watkins, M. J. Lindstrom, J. Harter, S. Sewall, A. Magliocco, J. Booske, M. Okoniewski, and S. Hagness, “A large-scale study of the ultrawideband microwave dielectric properties of normal breast tissue obtained from reduction surgeries,” *Phys. Med. Biol.*, vol. 52, pp. 2637 – 2656, Apr. 2007.

26. M. Lazebnik, D. Popovic, L. McCartney, C. B. Watkins, M. J. Lindstrom, J. Harter, S. Sewall, T. Ogilvie, A. Magliocco, T. M. Breslin, W. Temple, D. Mew, J. H.

Booske, M. Okoniewski, and S. Hagness, “A large-scale study of the ultrawideband microwave dielectric properties of normal, benign and malignant breast tissues obtained from cancer surgeries,” *Phys. Med. Biol.*, vol. 52, pp. 6093 – 6115, Oct. 2007.

27. K. Kim, N. Kim, S.-H. Hwang, Y.-K. Kim, and Y. Kwon, "A miniaturized broadband multi-state reflectometer integrated on a silicon MEMS probe for complex permittivity measurement of biological material," *IEEE Trans. Microw. Theory Tech.*, vol. 61, no. 5, pp. 2205 – 2214, May 2013.
28. J.-M. Kim, D. Oh, J. Yoon, S. Cho, N. Kim, J. Cho, Y. Kwon, C. Cheon, and Y.-K. Kim, "In vitro and in vivo measurement for biological applications using micromachined probe", *IEEE Trans. Microw. Theory Tech.,* vol. 53, no. 11, pp. 3415 – 3421, Nov. 2005.
29. J. C. Booth, N. D. Orloff, J. Mateu, M. Janezic, M. Rinehardt, and J. A. Beall, “Quantitative permittivity measurements of nanoliter liquid volumes in microfluidic channels to 40 GHz,” *IEEE Trans. Instrum. Meas.*, vol. 59, no. 12, pp. 3279 - 3288, Dec. 2010.
30. K. Grenier, D. Dubuc, P.-E. Poleni, M. Kumemura, H. Toshiyoshi, T. Fujii, and H. Fujita, “Integrated broadband microwave and microfluidic sensor dedicated to bioengineering,” *IEEE Trans. Microw. Theory Tech.*, vol. 57, no. 12, pp. 3246 - 3253, Dec. 2009.
31. T. Chen, D. Dubuc, M. Poupot, J.-J. Fournié, and K. Grenier, "Accurate nanoliter liquid characterization up to 40 GHz for biomedical applications: toward noninvasive living cells monitoring," *IEEE Trans. Microw. Theory Tech.,* vol. 60, no. 12, pp. 4171 – 4177, Dec. 2012.
32. B. Randall Jean, E. C. Green, and M. J. McClung, "A microwave frequency sensor for non-invasive blood-glucose measurement," in *IEEE Sensors Applications Symposium*, Feb. 2008, pp. 4 – 7.
33. K. M. Taylor and D. W. van der Weide, "Ultra-sensitive detection of protein thermal unfolding and refolding using near-zone microwaves," *IEEE Trans. Microw. Theory Tech.*, vol. 53, no. 5, pp. 1576 – 1586, May 2005.
34. http://dunemedical.com/
35. T. Karni, I. Pappo, J. Sandbank, O. Lavon, V. Kent, R. Spector, S. Morgenstern, and S. Lelcuk, "A device for real-time, intraoperative margin assessment in breast-conservation surgery," *The American Journal of Surgery*, 194, pp. 467 – 473, 2007.
36. J. T. Kindt and C. A. Schmuttenmaer, "Far-infrared dielectric properties of polar liquids probed by femtosecond terahertz pulse spectroscopy," *J. Phys. Chem.*, 1996, 100 (24), pp 10373 – 10379.

37. G. Guarin, M. Hofmann, R. Weigel, G. Fischer, D. Kissinger, "Determination of sugar concentration in aqueous solutions using ultra-wideband microwave impedance spectroscopy," in *IEEE MTT-S Int. Microw. Symp.*, Jun. 2013, pp. 1 – 4.
38. A. Manickam, A. Chevalier, M. McDermott, A. Ellington, and A. Hassibi, "A CMOS electrochemical impedance spectroscopy biosensor array for label-free biomolecular detection," in *ISSCC Dig. Tech. Paper*, pp. 130 – 131, Feb. 2010.
39. K.-H. Lee, J. Nam, S. Choi, H. Lim, S. Shin, G-H. Cho, "A CMOS impedance cytometer for 3D flowing single-cell real-time analysis with DS error correction," in *ISSCC Dig. Tech. Paper*, Feb. 2012, pp. 304 – 305.
40. P. Murali, I. Izyumin, D. Cohen, J.-C. Chien, A. M. Niknejad, and B. Boser, "A CMOS micro-flow cytometer for magnetic label detection and classification," in *ISSCC Dig. Tech. Papers*, Feb. 2014, pp. 422 – 423.
41. D. Bianchi, G. Ferrari, A. Rottigni, and M. Sampietro, "CMOS impedance analyzer for nanosamples investigation operation up to 150 MHz with sub-aF resolution," *IEEE J. Solid-State Circuits,* vo. 49, no. 12, pp. 2748 – 2757, Dec. 2014.
42. M. M. Bajestan, A. A. Helmy, H. Hedayati, and K. Entesari, " A 0.62 – 10 GHz complex dielectric spectroscopy system in 0.18-μm CMOS, ", *IEEE Trans. Microw. Theory Tech.*, vol. 62, no. 12, pp. 3522 – 3537, Dec. 2014.
43. K. Entesari, A. Reza Tavakoli, and A. Helmy, "CMOS distributed amplifiers with extended flat bandwidth and improved input matching using gate line with coupled inductors," *IEEE Trans. Microw. Theory Tech.*, vol. 57, no. 12, pp. 2862 – 2871, Dec. 2009.
44. S. C. Blaakmeer, E. A. M. Klumperink, D. M. W. Leenaerts, and B. Nauta, "Wideband balun-LNA with simultaneous output balancing, noise-canceling and distortion-canceling," *IEEE J. Solid-State Circuits*, vol. 43, no. 6, pp. 1341 – 1350, Jun. 2008.
45. F. Buckley and A. A. Maryott, "Tables of dielectric dispersion data for pure liquids and dilute solutions," Nat. Inst. Standards Technol., NBS circular 589, 1958.
46. D. S. Boyle, K. R. Hawkins, M. S. Steele, M. Singhal, and X. Cheng, "Emerging technologies for point-of-care CD4 T-lymphocyte counting," *Trends Biotechnol.*, vol. 30, no. 1, pp. 45 – 54, Jan. 2012.
47. C. Alix-Panabières and K. Pantel, "Challenges in circulating tumor cell research," *Nature Reviews Cancer*, vol. 14, no. 9, pp. 623 - 631, Sep. 2014.
48. F. B. Myers, O. J. Abilez, C. K. Zarins, and L. P. Lee, "Label-free electrophysiological cytometry for stem cell-derived cardiomyocyte clusters," *Lab Chip*. vol. 13, no. 2, pp. 220 – 228, Jan. 2013.
49. T. Sun and H. Morgan, "Single-cell microfluidic impedance cytometry: a review," *Microfluidics and Nanofluidics*, vol. 8, no. 4, pp. 423 – 443, Apr. 2010.

50. Y. Zheng, J. Nguyen, Y. Wei, and Y. Sun, "Recent advances in microfluidic techniques for single-cell biophysical characterization," *Lab Chip*. vol. 13, no. 13, pp. 2464 – 2483, Jul. 2013.

51. C. van Berkel, J. D. Gwyer, S. Deane, N. Green, J. Holloway, V. Hollis, and H. Morgan, "Integrated systems for rapid point of care (PoC) blood cell analysis," *Lab Chip*, vol. 11, no. 7, pp. 1249 – 1255, Jul. 2011.

52. S. Gawad, K. Cheung, U. Seger, A. Bertsch, and P. Renaud, "Dielectric spectroscopy in a micromacihned flow cytometer: theoretical and practical considerations," *Lab Chip.*, vol. 4, no. 3, pp. 241 - 251, Feb. 2004.

53. D. Holmes, D. Pettigrew, C. H. Reccius, J. D. Gwyer, C. van Berkel, J. Holloway, D. E. Davies, and H. Morgan, "Leukocyte analysis and differentiation using high speed microfluidic single cell impedance cytometry," *Lab Chip*, vol. 9, no. 20, pp. 2881 – 2889, Aug. 2009.

54. D. Holmes and H. Morgan, "Single cell impedance cytometry for identification and counting of CD4 T-cells in human blood using impedance labels," *Anal. Chem.*, vol. 82, no. 4, pp. 1455 – 1461, Jan. 2010.

55. L. Y. Zhang, C. Bounaix Morand du Puch, C. Dalmay, A. Lacroix, A. Landoulsi, J. Leroy, C. Melin, F. Lalloué, S. Battu, C. Lautrette, S. Giraud, A. Bessaudou, P. Blondy, M. O. Jauberteau, A. Pothier, "Discrimination of colorectal cancer cell lines using microwave biosensors," *Sens. Actuators A: Phys.*, vol. 216, pp. 405 – 416, Sep. 2014.

56. N. Haandbæk, Sebastian C. Bürgel, F. Heer, and A. Hierlemann, "Characterization of subcellular morphology of single yeast cells using high frequency microfluidic impedance cytometer," *Lab Chip*, vol. 14, no. 2, pp. 369 – 377, Jan. 2014.

57. Y. Yang, H. Zhang, J. Zhu, G. Wang, T.-R. Tzeng, X. Xuan, K. Huang, and P. Wang, "Distinguishing the viability of a single yeast cell with an ultra-sensitive radio frequency sensor", *Lab Chip*, vol. 10, no. 5, pp. 553 – 555, Mar. 2010.

58. G. A. Ferrier, S. F. Romanuik, D. J. Thomson, G. E. Bridges, and M. R. Freeman, "A microwave interferometric system for simultaneous actuation and detection of single biological cells," *Lab Chip*, vol. 9, no. 23, pp. 3406 – 3412, Oct. 2009.

59. H. Wang, A. Mahdavi, D. A. Tirrell, and A. Hajimiri, "A magnetic cell-based sensor," *Lab Chip*, vol. 12, no. 21, pp. 4465 – 4471, Nov. 2012.

60. J. S. Park, T. Chi, J. Butts, T. Hookway, T. McDevitt, H. Wang, "A multimodality CMOS sensor array for cell-based assay and drug screening," in *ISSCC Dig. Tech. Papers*, Feb. 2015, pp. 208 – 209.

61. M. Ballini, J. Müller, P. Livi, Y. Chen, U. Frey, A. Stettler, A. Shadmani, V. Viswam, I. Lloyd Jones, D. Jäckel, M. Radivojevic, M. K. Lewandowska, W. Gong, M. Fiscella, D. J. Bakkum, F. Heer, and A. Hierlemann, "A 1024-channel CMOS microeletrode array with 26,400 electrodes for recording and stimulation of

electrogenic cells in vitro," *IEEE J. Solid-State Circuits,* vo. 49, no. 11, pp. 2705 – 2719, Nov. 2014.

62. J.-C. Chien, M. Anwar, E.-C. Yeh, L. P. Lee, and A. M. Niknejad, "A 1-50 GHz dielectric spectroscopy biosensor with integrated receiver front-end in 65nm CMOS," in *IEEE MTT-S Int. Microw. Symp.,* Jun. 2013, pp. 1 - 4.

63. M. Bakhshiani, M. A. Suster, P. Mohseni, "A microfluidic-CMOS platform with 3D capacitive sensor and fully integrated transceiver IC for palmtop dielectric spectroscopy," in *ISSCC Dig. Tech. Papers*, Feb. 2015, pp. 386 – 387.

64. A. A. Helmy, H.-J. Jeon, Y.-C. Lo, A. J. Larsson, R. Kulkarni, J. Kim, J. Silva-Martinez, and K. Entesari, "A self-sustained CMOS microwave chemical sensor using a frequency synthesizer" *IEEE J. Solid-State Circuits*, vol. 47, no. 10, pp. 2467 – 2483, Oct. 2012.

65. B. Laemmle, K. Schmalz, J. Christoph Scheytt, R. Weigel, and D. Kissinger, "A 125-GHz permittivity sensor with read-out circuit in a 250-nm SiGe BiCMOS technology," *IEEE Trans. Microw. Theory Tech.*, vol. 61, no. 5, pp. 2185 – 2194, May. 2013.

66. I. Nasr, J. Nehring, K. Aufinger, G. Fischer, R. Weigel, and D. Kissinger, "Single- and dual-port 50-100-GHz integrated vector network analyzers with on-chip dielectric sensors," *IEEE Trans. Microw. Theory Tech.*, vol. 62, no. 9, pp. 2168 – 2179, Sep. 2014.

67. J.-C. Chien, M. Anwar, E.-C. Yeh, L. P. Lee, and A. M. Niknejad, "A 6.5/11/17.5/30-GHz high throughput interferometer-based reactance sensors using injection-locked oscillators and ping-pong nested chopping," *in Proc. Symp. VLSI Circuits Dig. Tech. Papers*, Jun. 2014, pp. 107 – 108.

68. S. Shekhar, M. Mansuri, F. O’Mahony, G. Balamurugan, J. E. Jaussi, J. Kennedy, D. J. Allstot, R. Mooney, and B. Casper, "Strong injection locking in low-Q LC oscilaltors: modeling and application in a forwarded-clock I/O receiver," *IEEE Trans. Circuits Syst. I, Reg. Papers,* vol. 56, no. 8, pp. 1818 – 1829, Aug. 2009.

69. J. F. Buckwalter, A. Babakhani, A. Komijani, and A. Hajimiri, "An integrated subharmonic coupled-oscillator scheme for a 60-GHz phased-array transmitter," *IEEE Trans. Microw. Theory Tech.*, vol. 54, no. 12, pp. 4271 – 4280, Dec. 2006.

70. Y. M. Tousi, O. Momeni, and E. Afshari, "A novel CMOS high-power terahertz VCO based on coupled oscillators: theory and implementation," *IEEE J. Solid-State Circuits*, vol. 47, no. 12, pp. 3032 – 3042, Dec. 2012.

71. F.-K. Wang, C.-J. Li, C.-H. Hsiao, T.-S. Horng, J. Lin, K.-C. Peng, J.-K. Jau, J.-Y. Li, and C.-C. Chen, "A novel vital-sign sensor based on a self-injection-locked oscillator," *IEEE Trans. Microw. Theory Tech.*, vol. 58, no. 12, pp. 4112 – 4120, Dec. 2010.

72. J. A. Smith, U. W. Rathe, and C. P. Burger, "Lasers with optical feedback as displacement sensors," *Optical Engineering*, vol. 34, no. 9, pp. 2802 – 2810, Sep. 1995.

73. W. H. Coulter, "High speed automatic blood cell counter and cell size analyzer," in *Proc. Natl. Electron Conf.*, 1956, pp. 1034 - 1042.

74. Y.-T. Liao, W. Biederman, and B. P. Otis, "A CMOS accelerometer using bondwire inertial sensing," in *Proc. Symp. VLSI Circuits*, Jun. 2009, pp. 64 – 65.

75. Y.-T. Liao, H. Yao, A. Lingley, B. Parviz, and B. P. Otis, "A 3-uW CMOS glucose sensor for wireless contact-lens tear glucose monitoring," *IEEE J. Solid-State Circuits*, vol. 47, no. 1, pp. 335 – 344, Jan. 2012.

76. Y. Hu, L. Huang, W. Rieutort-Louis, J. Sanz-Robinson, S. Wagner, J. C. Sturm, and N. Verma, "3D gesture-sensing system for interactive displays based on extended-range capacitive sensing," in *ISSCC Dig. Tech. Papers*, Feb. 2014, pp. 212 – 213.

77. L. Du, Y. Zhang, F. Hsiao, A. Tang, Y. Zhao, Y. Li, Z.-Z. Chen, L. Huang, M.-C. F. Chang, "A 2.3mW 11cm-range bootstrapped and correlated-double-sampling (BCDS) 3D touch sensor for mobile devices," in *ISSCC Dig. Tech. Papers*, Feb. 2015, pp. 122 – 123.

78. H. Wang, Y. Chen, A. Hassibi, A. Scherer, A. Hajimiri, "A frequency-shift CMOS magnetic biosensor array with single-bead sensitivity and no external magnet," in *ISSCC Dig. Tech. Papers*, Feb. 2009, pp. 438 – 439.

79. A. Hajimiri, S. Limotyrakis, and T. H. Lee, "Jitter and phase noise in ring oscillators," *IEEE J. Solid-State Circuits*, vol. 34, no. 6, pp. 790 – 804, Jun. 1999.

80. H. Wang, C.-C. Weng, and A. Hajimiri, "Phase noise and fundamental sensitivity of oscillator-based reactance sensors," *IEEE Trans. Microw. Theory Tech.*, vol. 61, no. 5, pp. 2215 – 2229, May 2013.

81. O. Elhadidy, M. Elkholy, A. A. Helmy, S. Palermo, and K. Entesari, "A CMOS fractional-N PLL-based microwave chemical sensor with 1.5% permittivity accuracy," *IEEE Trans. Microw. Theory Tech.*, vol. 61, no. 9, pp. 3402 – 3416, Sep. 2013.

82. O. Elhadidy, S. Shakib, K. Krenek, S. Palermo, and K. Entesari, "A 0.18-um CMOS fully integrated 0.7 - 6 GHz PLL-based complex dielectric spectroscopy system," in *Proc. IEEE Custom Integrated Circuits Conf.*, Sep. 2014, pp. 1–4.

83. B. Razavi, "A study of injection locking and pulling in oscillators," *IEEE J. Solid-State Circuits*, vol. 39, no. 9, pp. 1415 – 1424, Sep. 2004.

84. A. Mirzaei, M. E. Heidari, R. Bagheri, S. Chehrazi, and A. A. Abidi, "The quadrature LC oscillator: a complete portrait based on injection locking," *IEEE J. Solid-State Circuits*, vol. 42, no. 9, pp. 1916 – 1932, Sep. 2007.

85. A. Hajimiri and T. H. Lee, "A general theory of phase noise in electrical oscillators," *IEEE J. Solid-State Circuits*, vol. 33, no. 2, pp. 179 – 194, Feb. 1998.

86. J.-C. Chien, P. Upadhyaya, H. Jung, S. Chen, W. Fang, A. M. Niknejad, J. Savoj, and K. Chang, "A pulse-position modulation phase noise reduction technique for a 2-16 GHz injection-locked ring oscillator in 20nm CMOS, " in *ISSCC Dig. Tech. Papers*, Feb. 2014, pp. 52 – 53.

87. M. Hossain and A. C. Carusone, "CMOS oscillators for clock distribution and injection-locked deskew," *IEEE J. Solid-State Circuits*, vol. 44, no. 8, pp. 2138 – 2153, Aug. 2009.

88. L.-M. Lee and C.-K. K. Yang, "An LC-based clock buffer with tunable injection locking," *IEEE J. Solid-State Circuits*, vol. 44, no. 3, pp. 797 – 807, Mar. 2009.

89. X. Yi, C. C. Boon, H. Liu, J. F. Lin, and W. M. Li, "A 57.9-to-68.3 GHz 24.6 mW frequency synthesizer with in-phase injection-coupled QVCO in 65 nm CMOS technology," *IEEE J. Solid-State Circuits*, vo. 49, no. 2, pp. 347 – 359, Feb. 2014.

90. J.-C. Chien, N.-C. Kuo, and A. M. Niknejad, "A 26-GHz low-phase-error in-phase-coupled QVCO using modified bi-directional diodes," in *Proc. IEEE Radio Frequency Integrated Circuits Symposium (RFIC)*, May 2014, pp.253 – 256.

91. N. Watkins, B. M. Venkatesan, M. Toner, W. Rodriquez, and R. Bashir, "A robust electrical microcytometer with 3-dimensional hydrofocusing", *Lab Chip*, vol. 9, no. 22, pp. 3177 – 3184, Nov. 2009.

92. C. Sideris and A. Hajimiri, "Design and implementation of an integrated magnetic spectrometer for multiplexed biosensing," *IEEE Trans. Biomed. Circuits Syst.*, vol. 7, no. 6, pp. 773 - 784, Dec. 2013.

93. H. Wang, S. Kosai, C. Sideris, and A. Hajimiri, "An ultrasensitive CMOS magnetic biosensor array with correlated double counting noise suppression," in *IEEE MTT-S Int. Microw. Symp.*, Jun. 2010, pp. 616 – 619.

94. Y. M. Luijf, et. al., "Accuracy and Reliability of Continuous Glucose Monitoring Systems: A Head-to-Head Comparison", *Diabetes Technol. Ther.*, vol. 15, no. 8, Aug. 2013, pp. 721 – 726.

95. M. Hofmann, et. al., "Microwave-based noninvasive concentration measurements for biomedical applications," *IEEE Trans. Microw. Theory Tech.*, vol. 61, no. 5, pp. 2195 – 2204, May 2013.

96. G. Guarin, et. al., "Determination of sugar concentration in aqueous solutions using ultra-wideband microwave impedance spectroscopy," *in IEEE MTT-S Int. Microw. Symp.*, Jun. 2013, pp. 1 – 4.

97. T. Chretiennot, et. al., "Double stub resonant biosensor for glucose concentrations quantification of multiple aqueous solutions," in *IEEE MTT-S Int. Microw. Symp.*, Jun. 2014, pp. 1 – 4.

98. Y. Cui, J. Li, W. Cao, and P. Wang, "Highly sensitive RF detection and analysis of DNA solutions," in *IEEE MTT-S Int. Microw. Symp.*, Jun. 2014, pp. 1 – 4.